LUND UNIVERSITY

Control of Laser Focusing using a Deformable Mirror and a Genetic Algorithm

Lundh, Olle

2003

Link to publication

Citation for published version (APA):
Lundh, O. (2003). *Control of Laser Focusing using a Deformable Mirror and a Genetic Algorithm*. (Lund Reports on Atomic Physics). [Publisher information missing].

Total number of authors:
1

General rights
Unless other specific re-use rights are stated the following general rights apply:
Copyright and moral rights for the publications made accessible in the public portal are retained by the authors and/or other copyright owners and it is a condition of accessing publications that users recognise and abide by the legal requirements associated with these rights.
• Users may download and print one copy of any publication from the public portal for the purpose of private study or research.
• You may not further distribute the material or use it for any profit-making activity or commercial gain
• You may freely distribute the URL identifying the publication in the public portal

Read more about Creative commons licenses: https://creativecommons.org/licenses/

Take down policy
If you believe that this document breaches copyright please contact us providing details, and we will remove access to the work immediately and investigate your claim.

LUND UNIVERSITY

PO Box 117
221 00 Lund
+46 46-222 00 00

Download date: 11. Sep. 2024

Control of Laser Focusing using a Deformable Mirror and a Genetic Algorithm

Master's thesis
by
Olle Lundh

Lund Reports on Atomic Physics, LRAP-315
Lund, November 2003

Abstract

In this thesis an *adaptive optics* system has been developed, implemented and evaluated at the Lund High Power Laser facility, Atomic Physics Division, Lund Institute of Technology. The laser system delivers ultrashort pulses with peak powers exceeding 40 TW at a repetition rate of 10 Hz. The pulses are focused to achieve extreme irradiance exceeding 10^{19} W/cm^2. In order to increase the peak intensity at the focal spot it is possible to either increase the pulse energy, to reduce the pulse length or to make the focal spot smaller. Cost and the laser bandwidth put limits to the two first alternatives. This thesis explores the third option.

The aim for this project was to investigate the abilities of an *adaptive optics* system to precompensate for alignment or intrinsic optical errors that would degrade the focusing power of the laser system. A test system, using a smaller deformable mirror than required for the main laser system was developed and implemented by the author and comprise a deformable mirror, a detection system and an optimization algorithm. The deformable mirror was a Micromachined Membrane Deformable Mirror (MMDM), it had 37 electrostatic actuators and was coated with gold. The detection system measured the focal spot peak intensity and the mirror shape was optimized by a Genetic Algorithm (GA). Heavily astigmatic foci were routinely corrected and the MMDM was used to precompensate for the astigmatic errors introduced by off-axis focusing with a spherical mirror. At an off-axis angle of 17^o, the focal spot size was improved from 6.5 to 1.3 times the diffraction limit. When the laser was focused with a well aligned parabolic mirror, the algorithm and the deformable mirror were still able to increase the focal spot peak intensity by 85%. The deformable mirror was also used to *manipulate* the focal spot intensity profile. Multiple focal spots of equal intensity were successfully generated from a single beam and a scheme that would allow tailored focal spots was tested.

Contents

Chapter 1

Introduction

Ever since the introduction in the 1960:s, laser technology has been under continuous development and laser radiance is today available in a broad spectral range, from far infrared to x-ray radiation. Of particular interest has been the development of high-power lasers and the peak power generated from an intense pulse of laser radiation has increased by 12 orders of magnitude (10^{12}) during the last forty years. The *modelocking* technique [21] made possible the generation of ultrashort (or ultrafast) laser pulses in the femtosecond domain. Very short pulses may produce very intense radiation, even at low energies. A 100 fs pulse, carrying an energy of 1 mJ produce a peak power of 10 GW. At some point the high intensities of the laser pulses may damage the optics and the crystals that are used for the pulse generation, making further amplification impossible. One obvious solution to this problem is to expand the laser beam but this requires large optics and large crystals and thus tends to result in very expensive facilities. A better solution came with the innovative design of the *chirped pulse amplification* (CPA) technique. The CPA technique has made possible the generation of ultrafast *and* energetic laser pulses, using very compact laser systems.

The work that is presented in this thesis has been performed at the Lund High Power Laser Facility, Atomic Physics Department, Lund Institute of Technology. Its high-power CPA laser system delivers ultrashort pulses of 35 fs duration with peak powers exceeding 40 TW at a repetition rate of 10 Hz. These pulses are focused to achieve extreme irradiance, exceeding 10^{19} W/cm^2. Such high intensities make new areas of research accessible. The high-power laser system in Lund is continuously developed in order to increase the peak power reached when the laser pulses are focused. A look at the theoretical definition of intensity reveals the important parameters,

$$I = \zeta \cdot \frac{E}{\pi r^2 \tau} \tag{1.1}$$

where E is the pulse energy, τ is the pulse duration and r is the focal spot radius at $1/e^2$ of the peak intensity. ζ depends on the temporal shape of the pulse and for a Gaussian pulse, it is 2. It is clear that, in order to increase the intensity at the focal spot there are three possibilities. The pulse energy may be increased, the pulse duration may be shortened or the focal spot radius may be reduced. Cost is often the limit when it comes to increase the pulse energy. The radiation

from a Ti:sapphire laser is centered around 800nm so the period of the electric field is

$$T = \frac{1}{f} = \frac{\lambda}{c} \approx 3fs \tag{1.2}$$

Since the pulse must contain at least a few periods the laser wavelength puts a lower limit to the length of the laser pulse. This limit is almost reached since the Terawatt laser in Lund may produce 35fs pulses. The focused intensity has however a quadratic dependence on the radius of the focal spot so an efficient way to increase the peak power of the laser system would be to reduce the size of the focal spot. When a laser beam is focused, the ideal diameter of the focal spot is

$$d = \frac{4\lambda f}{\pi D} \tag{1.3}$$

where λ is the wavelength of the laser, D is the beam diameter and f is the focal length of the focusing optics. This is the ideal diameter or, the *diffraction limit* of the focal spot. In CPA laser systems however, alignment errors, surface quality of optical components, thermal and nonlinear effects and doping inhomogeneities in the amplifying crystals influence the laser beam quality and degrade the focusing power of the system. Even in an ideal situation where the focusability is limited only by the f-number of the focusing optics, f/D, alignment difficulties may limit the size of the focal spot. At the end of CPA laser chains, such as the high-power system in Lund, the ultrafast pulses are focused by a parabolic mirror. At present a f/3 focusing mirror is used so replacing this mirror with a f/1 focusing mirror would reduce the diameter of the focal spot to one third of the present size and thus increase the peak intensity by almost a factor of 10. A f/1 parabola is however extremely difficult to manufacture accurately and very difficult to align [2] [1] so, in effect, the peak intensity would not increase that much.

The aim for this thesis was to investigate the abilities of an *adaptive optics* system to precompensate for alignment or intrinsic optical errors that degrade the focusing power of the laser system. Adaptive optics was originally developed by astronomers in order to compensate for imaging aberrations originating from turbulence in the atmosphere. Adaptive optics has however also found vast applications in laser development and have been used for temporal [3] [7] [27] as well as spatial [2] [17] [9] control of high-power lasers. A conventional adaptive optics system is a feed-back loop comprising a wavefront sensor, a control computer and a phase correcting element. The wavefront sensor measures the phase distortions that are to be corrected, the control computer analyzes the measurement and the phase correcting element (most often a deformable mirror) performs the correction. A detailed description of the deformable mirror that has been used for wavefront correction in this work is given in Chapter 2 and 4. This thesis investigates the possibilities to, instead of using a wavefront sensor, use a search algorithm in order to find the desired shape of the deformable mirror. Mainly two search methods have been used for this kind of optimization, *Genetic Algorithms* [2] [1] [3] [6] [15] [27] and *Stochastic Parallel Gradient Descent* [18] [25]. The genetic algorithm was chosen for this work and is explained in Chapter 3 and 4.

Chapter 2

Adaptive optics

Most optical systems suffer from construction defects or environmental aberrations that degrade the performance of the system. An imaging system may be troubled by the turbulence in the medium of propagation or badly manufactured lenses. Adaptive optics are designed to correct for such aberrations. This chapter describes the main components of a conventional adaptive optics system, that is a deformable mirror and a wavefront sensor. The last section treats a simulation of the deformable mirror that was used in Chapter 5 for wavefront correction. But first, a short review of the wave nature of light.

2.1 Propagation of light

In a mathematical formalism a monochromatic wave may be written as [16]

$$u(P,t) = U(P)cos(\omega t + \phi(P)) \tag{2.1}$$

where $U(P)$ and $\phi(P)$ are the amplitude and phase of the wave at position P, while ω is the optical frequency. It is convenient to use a complex notation such that

$$u(P,t) = Re\left[\mathbf{U}(P)e^{-i\omega t}\right] \tag{2.2}$$

where the *phasor*, $\mathbf{U}(P)$, is

$$\mathbf{U}(P) = U(P)e^{-i\phi(P)}. \tag{2.3}$$

In a plane (x, y), perpendicular to the direction of propagation, the field is

$$\mathbf{U}(x,y) = U(x,y)e^{-i\phi(x,y)}. \tag{2.4}$$

The function $\phi(x, y)$ will often be referred to as the *wavefront*. Most detectors, including the human eye, cannot detect the electric field directly. Instead the measured quantity is *intensity*, defined as

$$\mathbf{I} = \mathbf{U}\mathbf{U}^{\dagger} \tag{2.5}$$

where $\mathbf{U}^{\dagger}$ is the conjugate of the complex electric field $\mathbf{U}$. Now consider diffraction of monochromatic light from a finite aperture to an infinite screen. The

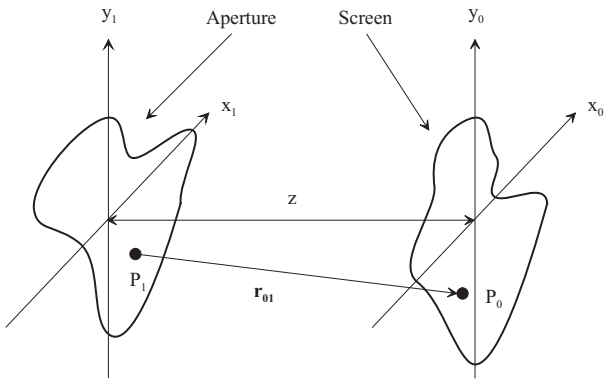

Figure 2.1: Diffraction geometry.

aperture and the screen are assumed to be plane and parallel, at a normal distance z. A rectangular coordinate system (x_0, y_0) is attached to the plane of observation, with the coordinate axes parallel to (x_1, y_1) in the aperture plane. A general expression for the electric field at the screen is, under *paraxial* conditions, given by [10]

$$\mathbf{U}(x_0, y_0) = \iint \mathbf{h}(x_0, y_0; x_1, y_1)\mathbf{U}(x_1, y_1)dx_1 dy_1 \tag{2.6}$$

where

$$\mathbf{h}(x_0, y_0; x_1, y_1) = \frac{1}{i\lambda}\frac{e^{ikr_{01}}}{r_{01}}. \tag{2.7}$$

In this expression r_{01} is the distance between the points (x_0, y_0) and (x_1, y_1) and $k = 2\pi/\lambda$ is the *wave number*.

2.1.1 Aberrations

Diffraction, as stated in equation 2.6, is a natural property of the wave nature of light and puts fundamental limitations to any optical system. Whenever an optical system is free from aberrations it will be referred to as diffraction limited. Unfortunately, aberrations may distort the propagating wave along the optical path and thus degrade the system performance. The sources of aberrations depend on the specific system but can generally be divided into *monochromatic* and *chromatic* aberrations. Chromatic aberrations may occur since the refractive index is a function of frequency, $n = n(\omega)$. Important monochromatic aberrations that often occur in optical systems are spherical aberration, coma and astigmatism.

Spherical aberration

For an aberration free lens all geometrical rays pass through the focal point. The effect of spherical aberration is that rays entering farther away from the optical axis focus nearer the lens. Spherical aberration is dependent on the lens shape and, theoretically, the simplest way to eliminate or reduce spherical aberration is to make a lens surface with a varying radius of curvature. Aspheric lenses

$\rho \cos\theta$	tilt
$\rho^2 \cos^2\theta$	astigmatism
$\rho^3 \cos\theta$	coma
ρ^4	spherical aberration

Table 2.1: Seidel terms and their meaning.

are available but most lenses with high surface quality are manufactured by techniques that naturally produce spherical surfaces. In general, positive lenses have undercorrected spherical aberration and negative lenses have overcorrected spherical aberration. By combining a positive lens and a negative lens it is possible suppress spherical aberrations.

Coma

When an object is imaged by a spherical lens that suffers from coma, rays that pass through the periphery of the lens will form a larger image than the rays that pass close to the center of the lens. This blurs in the image plane and an off-axis object point does not form a sharp image point, but appears as a characteristic comet-like object.

Astigmatism

When an off-axis object is focused by a spherical lens, the natural asymmetry leads to astigmatism. The system appears to have two different focal lengths. The images of an object point are separated along the optical axis and are not points. Instead the first image is a line, stretched in same direction as the off-axis displacement off the object point. The second image is also a line, rotated 90° with respect to the first focal line. Between these lines the image is a circular blur, called the circle of least confusion.

2.1.2 Representing the wavefront

The *wavefront* is indeed a fundamental quantity and a number of mathematical tools have been developed in order to describe the phase of a beam. In adaptive optics it is often the phase that is altered in order to change the propagation of the beam. In fact all the primary aberrations, that is tilt, astigmatism, coma and spherical aberration can be considered as phase distortions to a plane wave. The *wavefront*, $\phi(x, y)$, was defined in equation 2.4. It is a two-dimensional map of the phase at a plane, normal to the line between the beam origin and the observer. The wavefront is positive in the direction of propagation. For simplicity the rectangular aperture coordinate system (x, y) is frequently replaced by a polar coordinate system (ρ, θ), through

$$x = \rho \cos\theta, \;\; y = \rho \sin\theta.$$

$\rho\cos\theta$	Tilt in x direction
$\rho\sin\theta$	Tilt in y direction
$\rho^2\cos 2\theta$	Astigmatism ($\pm 45^o$)
$2\rho^2 - 1$	Defocusing
$\rho^2\sin 2\theta$	Astigmatism (0^o and 90^o)
$(\rho^3 - 2\rho)\cos\theta$	Coma

Table 2.2: Zernike polynomials and their meaning.

Seidel terms

A power series representation of the wavefront would be

$$\phi(\rho,\theta) = \sum_{m,n} a_{mn}\,\rho^n \cos^m\theta + b_{mn}\,\rho^n \sin^m\theta. \tag{2.8}$$

It can be shown [5] that some of the first terms in this series describe the primary (or Seidel) aberrations. Some terms and their meaning are listed in Table 2.1. A fourth aberration, *tilt* is added to the previously described aberrations. Tilt is a very common aberration, also known as beam pointing, even though it is not always treated as an aberration as such. Tilt simply alters the direction of the beam, which means that the wavefront is *tilted*.

Zernike polynomials

The polynomials in Table 2.1 are not linearly independent. An orthogonal basis on the unit circle that is commonly used in adaptive optics is the Zernike basis. Zernike polynomials are linear combinations of the terms in equation 2.8. The first few Zernike polynomials are given in Table 2.2 [30].

2.1.3 Far-field diffraction and the Fourier transforming properties of lenses

The propagation of a beam is described by equation 2.6. As the electromagnetic wave propagates, the intensity pattern, $\mathbf{I}(x,y)$, varies. We will investigate what the intensity pattern looks like with a long distance between the aperture and the observer, that is in the far-field. In this context, a long distance z means that z must fulfill the *Fraunhofer* assumption;

$$z \gg \frac{k(x_1^2 + y_1^2)_{max}}{2} \tag{2.9}$$

where $k = 2\pi/\lambda$ is the *wave number*. Under this assumption the field distribution at the screen is to a good approximation given by *Fraunhofer* diffraction [10]

$$\mathbf{U}(x_0,y_0) = \frac{e^{ikz}e^{\frac{ik}{2z}\left(x_0^2+y_0^2\right)}}{i\lambda z}\iint \mathbf{U}(x_1,y_1)e^{-\frac{2\pi i}{\lambda z}(x_0x_1+y_0y_1)}dx_1dy_1 \tag{2.10}$$

The two-dimensional *Fourier*-transform of a function $\mathbf{U}(x,y)$ is defined as

$$\mathcal{F}\{\mathbf{U}\}(f_x,f_y) = \iint \mathbf{U}(x,y)e^{-2\pi i(xf_x+yf_y)}dxdy \tag{2.11}$$

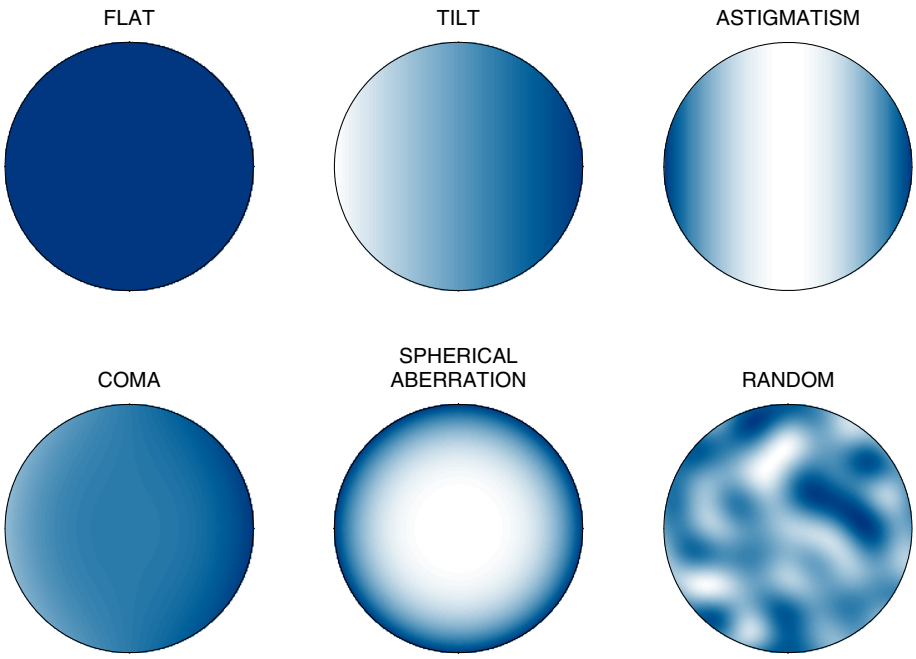

Figure 2.2: Resulting wavefronts when a plane wave is subject to the aberrations in Table 2.1. The unperturbed wavefront and a random wavefront are also shown.

Looking again at equation 2.10 we realize that, aside from the factors in front of the integral, the field distribution at the screen of observation is nothing else than the two dimensional *Fourier* transform of the aperture field, evaluated for spatial frequencies

$$f_x = x_0/\lambda z\,, \quad f_y = y_0/\lambda z \tag{2.12}$$

The aperture-screen distance required for the validity of the Fraunhofer integral may indeed be long. For an optical wavelength of 600nm (red light) and an aperture diameter 1cm, the aperture-screen distance must satisfy

$$z \gg \frac{\pi}{600 \cdot 10^{-9}} \cdot (0,005^2 + 0,005^2) \approx 250 \text{ meters}$$

Even if this distance may appear to be long, Fraunhofer diffraction patterns can be observed at distances more suitable for laboratory work. In fact it can be shown [10] that if a lens is placed at the aperture, the Fraunhofer diffraction formula 2.10 is valid in the focal-plane. Substituting the distance z with the focal length f of the lens gives the intensity distribution at the focal-plane

$$\mathbf{I}(x_0, y_0) = \frac{1}{\lambda^2 f^2} \left| \iint \mathbf{U}(x_1, y_1) e^{-\frac{2\pi i}{\lambda f}(x_0 x_1 + y_0 y_1)} dx_1 dy_1 \right|^2 \tag{2.13}$$

So, when focusing monochromatic light the shape of the focal spot is essentially the squared absolute value of the Fourier transform of the field at the lens. In order to study the effects of the primary aberrations in Table 2.1 we consider a circular aperture and a field of constant amplitude, A, and initially flat phase. Figure 2.3 shows the unaberrated focal spot and the focal spot when the beam

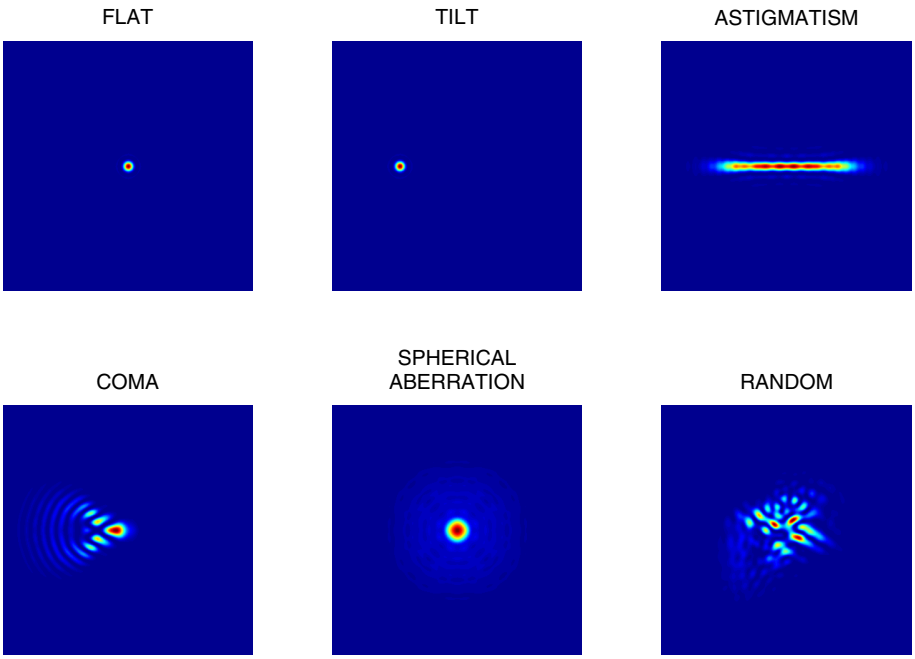

Figure 2.3: Resulting focal spots when the phases of the electric fields are the wavefronts in Figure 2.2. The amplitude is constant over the aperture so the electric field at the aperture is $U(x_1, y_1) = Ae^{-i\phi(x_1,y_1)}$.

is subject to the primary aberrations in Table 2.1. The corresponding aperture phases are shown in Figure 2.2.

2.2 Wavefront sensing

A wavefront sensor is an instrument used to obtain the phase, ϕ, of a wave as defined in equation 2.4. The sensor often consists of an optical head, detectors, electronics, computer controlled data acquisition and a sophisticated software program that reconstructs the wavefront from measured data. Wavefront sensors are of great importance in adaptive optics and many types of sensors have been developed. This section describes briefly two of the most popular wavefront sensing techniques.

2.2.1 Lateral shearing interferometer

A lateral shearing interferometer exploits the principle of self-reference for the measurement of the wavefront. The beam is in some way split in two and the two beams are displaced by some lateral distance δ. The two beams interfere and the intensity pattern of the normalized interferogram is

$$I(x,y) = \left| e^{i\phi(x,y)} + e^{i\phi(x+\delta,y)} \right|^2 = 2 + 2\cos[\phi(x,y) - \phi(x+\delta,y)]. \qquad (2.14)$$

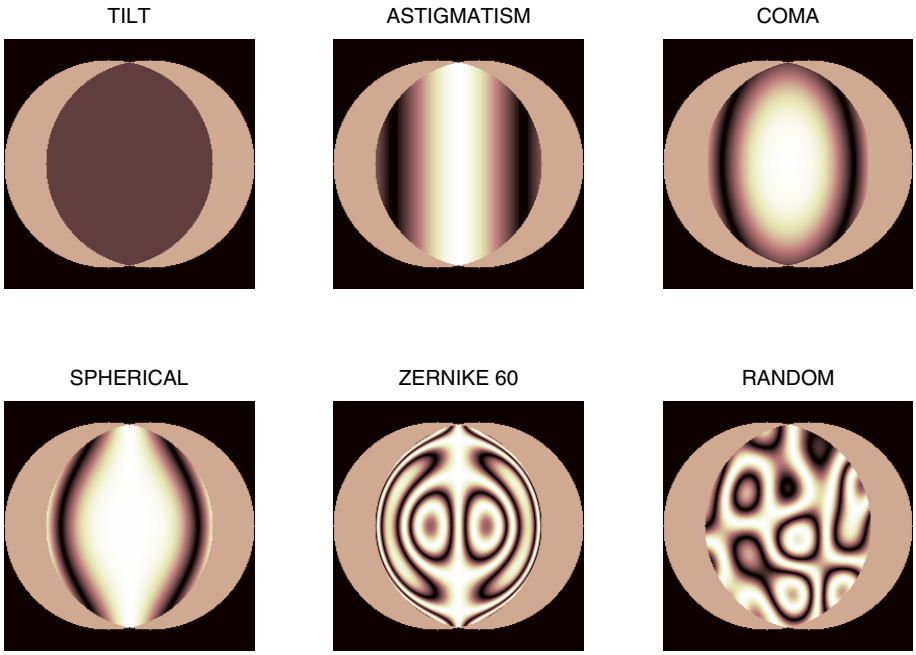

Figure 2.4: Lateral shearing interferograms. The diameters of the interfering beams are R. The center-to-center distance between the beams is 0.4R. The interferograms were obtained by using equation 2.14. The wavefronts are tilt, astigmatism, coma and astigmatism, as given in Table 2.1. The aperture amplitudes of the electric fields were constant, $U(\rho, theta) = Ae^{-i\phi(\rho,\theta)}$. The interferograms that would be the results from a circular symmetric Zernike wavefront, $\phi(\rho,\theta) = Z^{60}(\rho,\theta) = -1+12\rho^2-30\rho^4+20\rho^6$, and from a random wavefront is also shown.

Lateral shearing interferograms that would be the result from the wavefronts in Table 2.1 are shown in Figure 2.4. In order to fully reconstruct the wavefront, it is necessary to record several shearing interferograms. Harbers *et al.* [11] describe a modal reconstruction technique, using two orthogonal shearograms. Modal reconstruction means here that the reconstructed wavefront is a linear combination of Zernike polynomials (see Table 2.2). Lateral shearing interferometers, using three waves instead of two, have been used for wavefront reconstruction of high-power laser pulses [9] [19] [26].

2.2.2 Shack-Hartmann wavefront sensor

The most commonly used wavefront sensor seems to be the Shack-Hartmann wavefront sensor [4] [17] [18] [28] [29] [30]. The sensor consists of an array of very small lenses, mounted in front of a CCD detector. The CCD is positioned in the focal plane of the lenslets. The principle of the measurement is illustrated in Figure 2.5. Each of the lenslets samples the incident wave and focuses it to a small spot on the CCD. If the incident wave is plane, the spots will be positioned in front of the sub apertures, resulting in a regular pattern. If, however, the incident wave is locally tilted over a sub aperture, that spot will be shifted. The shift will be proportional to the local tilt of the incident wave. What is

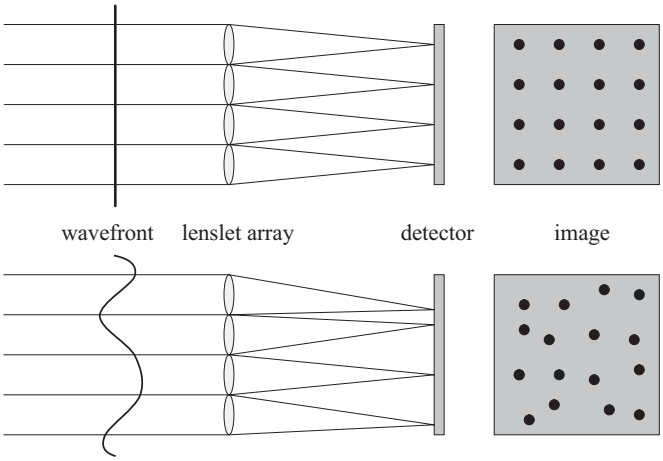

Figure 2.5: Shack-Hartmann wavefront sensing technique

measured is thus the local tilt over each of the sub apertures, that is the sampled wavefront gradient. The wavefront is then obtained through integration.

2.3 Wavefront correction

A distorted wavefront may be corrected by many of the same mechanisms that are responsible for the distortion. If an optical device introduces a phase distortion, another optical device may be designed in order to introduce the reversed, that is conjugated, distortion. Altering the phase means changing the length of the optical path which depends both on refractive index and the geometrical path length. A correcting device could hence adjust either the refractive index or the geometrical path length. Reflective devices (mirrors) are used to alter the geometrical path length and transmissive devices (liquid crystals) are used to alter the refractive index. Wavefront correctors are generally reflective as a consequence of their wavelength insensitivity. In general, the dispersion of transmissive systems is a problem for use over broad spectral ranges.

A wavefront corrector should be designed in order to match the specific aberrations that one wants to correct. The resolution, or the number of corrective zones, is important as is the maximum possible adjustment to the optical path length. The response time of the corrective device should also be considered.

2.3.1 Tilt correction

The simplest form of wavefront correction is probably variation of the beam direction, or the tilt of the wavefront. The tilt corrector is generally a steerable plane mirror.

2.3.2 Segmented mirrors

The first multichannel wavefront correctors were the segmented mirrors. A segmented mirror is constructed by a number of small mirrors that may be

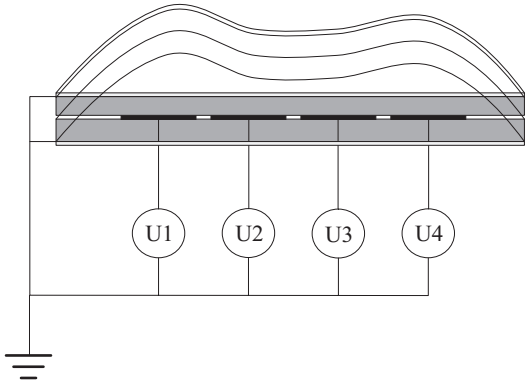

Figure 2.6: The bimorph mirror principle.

manipulated independently. The adjustment of each segment may involve both tilt and translation. The main advantage of this kind of mirror is the aperture scalability (just add more segments) and the fact that damaged mirror segments are replaceable. The primary drawback of the segmented mirror is that the gaps between the segments scatter the light, resulting in unwanted diffraction.

2.3.3 Deformable mirrors

The drawbacks of the segmented mirror may be circumvented if one uses a continuous faceplate with an array of actuators. The faceplate is a thin mirror that may be deformed. The actuators behind it push or pull on the surface, producing local deformations of the mirror surface. The total shape of the mirror may be controlled through the actuators. Deformable mirrors can be constructed in many ways. Two common techniques used in laser applications are those of the bimorph and membrane deformable mirrors.

Bimorph deformable mirrors

A bimorph deformable mirror is composed of two plates of piezoelectric ceramics which are poled in the same direction, see Figure 2.6. An array of actuator electrodes are positioned between the plates before bonding them together. Conducting electrodes are then added to the top and bottom of the piece. The top electrode may either be polished and used as the mirror phase plate right away or a separately manufactured phase plate is glued to the top electrode. When the front and bottom electrodes are grounded and voltage is applied to an actuator electrode, the ceramic changes shape as a consequence of the piezoelectric properties and the poling of the material. One of the plates responds to the applied voltage by shrinking while the other plate expands. This causes bending of the entire plate. The size of the deformation, or the local radius of curvature of the bimorph mirror, depends then on the applied voltage. The density of actuators is limited since the dimensions of the electrodes must be large compared to the thickness of the piezoelectric plates in order to have sufficient effect. This makes the bimorph mirror suitable in applications requiring only low order corrections [4][17]. The simple design and fabrication of the bimorph mirror allows the production to be rather inexpensive.

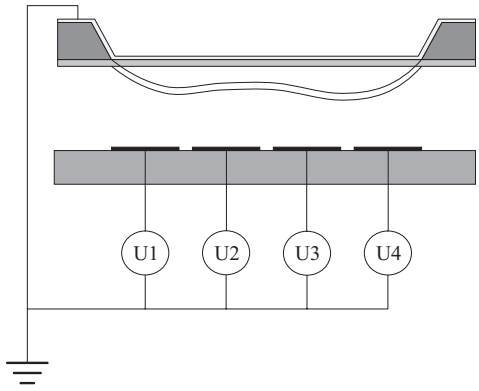

Figure 2.7: The membrane mirror principle.

Membrane deformable mirrors

The membrane deformable mirror is another type of continuous surface deformable mirror. The mirror is in this case a reflective membrane that is somehow made conductive. The membrane is then suspended over an array of actuator electrodes, see Figure 2.7. When the membrane is grounded and a voltage is applied to one of the actuator electrodes the resulting electrostatic force between the membrane and the electrode produce a local deformation of the membrane. The total mirror shape is the summed effect of all actuator voltages. The actuator electrodes must be separated far enough so that they can withstand the voltages applied. This distance is however the main limitation to the achievable actuator density, which often permits quite many actuators on a small aperture. The temporal bandwidth of the membrane mirrors often exceeds 1kHz, which allow high-speed corrections.

One type of membrane mirrors that have received attention for some years now are the so called micromachined membrane deformable mirrors (MMDM) [1][3][6][9][18][22][23][24][25][27][29][30]. The membrane of these devices is in this case made from a substrate of silicon. The production of a MMDM is thus compatible with the silicon industrial manufacturing methods and may allow mass production of low-cost deformable mirrors. The deformable mirror used in this work belongs to this class of mirrors. It has 37 hexagonal electrostatic actuators and is coated with gold. The membrane diameter is 15mm and the membrane material is silicon nitride, Si_3Ni_4. A detailed description of the mirror in Figure 2.8 will follow in Section 4.2.

2.4 Modelling the Membrane Deformable Mirror

It has been experimentally shown that a membrane model is suitable for a static description of a MMDM. The deflection u(x,y) of the membrane under an external load p(x,y) is given by the Poisson equation [20];

$$\Delta u = -\frac{p}{T} \tag{2.15}$$

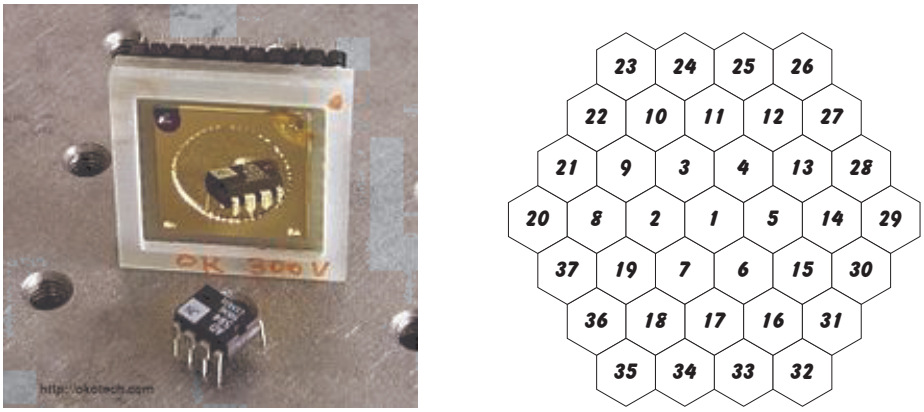

Figure 2.8: The Micromachined Membrane Deformable Mirror that was used for wavefront correction. The left picture shows the mirror and is from *okotech.com*. The right figure shows the actuator structure. The mirror has 37 hexagonal actuators.

where T is the membrane tension and is given by [22]

$$T = \frac{Eh\delta}{2(1-\upsilon)}. \tag{2.16}$$

E is Young's modulus of the membrane material (silicon nitride), h is the thickness of the membrane, υ is the Poisson ratio of the membrane material and δ is the in-plane elongation due to stretching. The change of the membrane tension, T, as the membrane is deflected is considered negligible.

In order to determine the electrostatic load imposed on the membrane by the actuator structure we consider the load on a small element of area dA of the membrane-actuator structure. The element is equivalent to a plate capacitor so the electric field is

$$E = \frac{V(x,y)}{d(x,y)}. \tag{2.17}$$

The membrane is grounded and V(x,y) is the voltage applied to the actuator structure at (x,y). d(x,y) is the distance between the membrane and the actuator structure at (x,y). The attractive force between the plates is $F = QE = QV(x,y)/d(x,y)$ where Q is the charge trapped in the capacitor and is given by $Q = CV(x,y)$. C is the capacitance of the element, given by $C = \epsilon\epsilon_0 dA/d(x,y)$. Finally, the force on the membrane element is

$$F = -\epsilon\epsilon_0 \frac{V(x,y)^2}{d(x,y)^2} dA. \tag{2.18}$$

The sign is negative since the membrane will be attracted towards the actuators. The pressure or load per unit area is then

$$p(x,y) = -\epsilon\epsilon_0 \frac{V(x,y)^2}{d(x,y)^2}. \tag{2.19}$$

The silicon nitride membrane is fabricated on the surface of a silicon wafer (see Section 4.2.1). When the silicon substrate is etched away, the membrane will

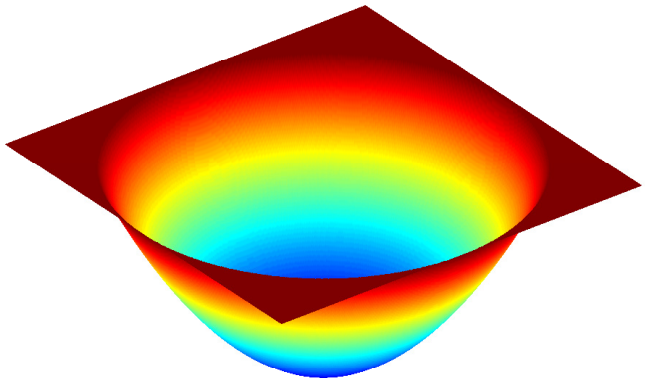

Figure 2.9: When all actuators have the same voltages, the membrane takes on a parabolic shape.

still be clamped at the edges. Thus the boundary condition u=0 has to be added to the Poisson equation. The static deflection of the MMDM is now given as the solution to

$$\begin{cases} \Delta u = \epsilon\epsilon_0 \frac{V^2}{Td^2} & (x,y) \in \Omega \\ u(x,y) = 0 & (x,y) \in \partial\Omega \end{cases} \tag{2.20}$$

where $\partial\Omega$ is the membrane boundary and Ω is the membrane.

2.4.1 Membrane response to identical actuator voltages

We first consider the simple case where the same voltage V_0 is applied to all the actuators. The membrane is circular with radius R. In polar coordinates we get

$$\frac{1}{r}\frac{\partial}{\partial r}\left(r\frac{\partial u}{\partial r}\right) + \frac{1}{r^2}\frac{\partial^2 u}{\partial \theta^2} = \zeta V_0^2 \tag{2.21}$$

where $\zeta = \epsilon\epsilon_0/Td^2$ is assumed to be constant over the membrane. This is true if we assume that the deflection of the membrane is small compared to the distance between the actuator structure and the membrane. Circular symmetry eliminates the angular term, leaving

$$\frac{1}{r}\frac{\partial}{\partial r}\left(r\frac{\partial u}{\partial r}\right) = \zeta V_0^2 \Rightarrow \frac{\partial u}{\partial r} = \zeta V_0^2 \frac{r}{2} + A\frac{1}{r}. \tag{2.22}$$

But, since $\partial u/\partial r < \infty$, the constant A is zero. The boundary condition, $u = 0$, gives that

$$u(r) = \frac{\zeta V_0^2}{4}\left(r^2 - R^2\right). \tag{2.23}$$

So, the MMDM takes on a parabolic shape when identical voltages is applied to all actuators, see Figure 2.9. Note that the deflection of the membrane is proportional to the *square* of the applied voltage.

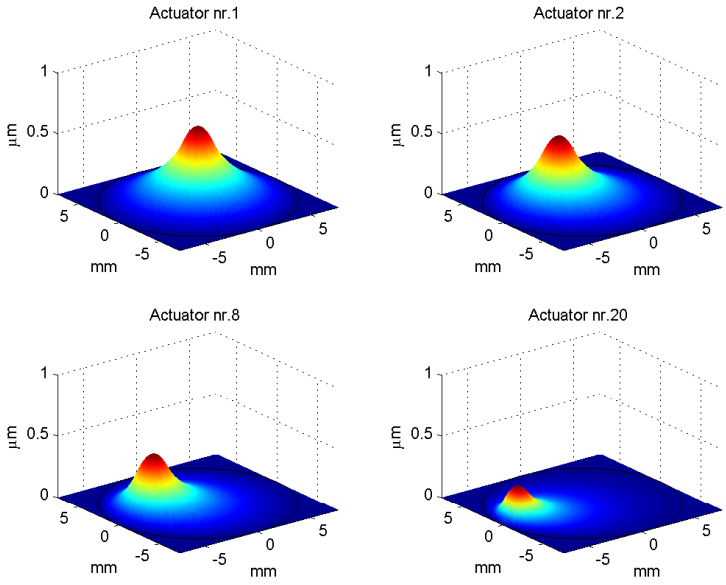

Figure 2.10: Influence functions for actuators 1, 2, 8 and 20. This is the membrane response when maximum pressure is applied from a single actuator.

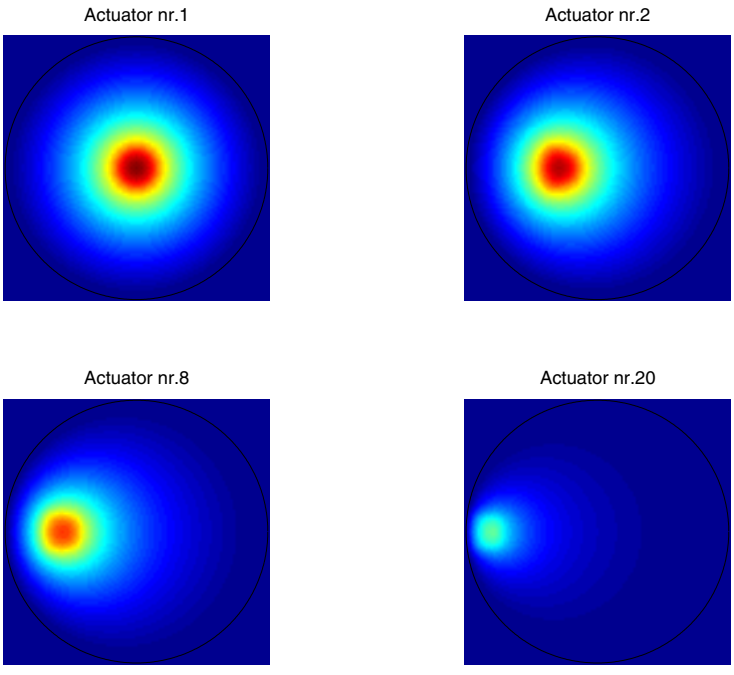

Figure 2.11: Same as Figure 2.10 but the view is from above.

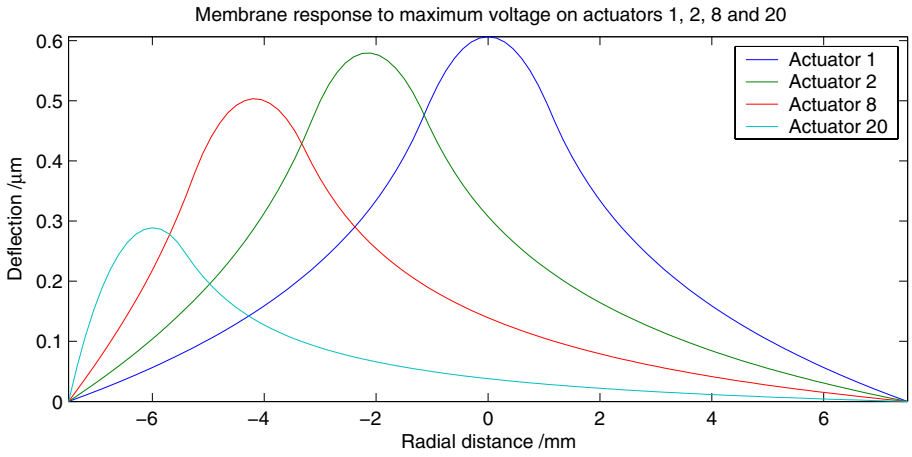

Figure 2.12: Line-out of the influence functions in Figure 2.10. The matrix **A** in equation 2.25 was normalized so the deflection was $5.4\mu m$ when maximum voltage was applied to all actuators. This deflection was measured experimentally, see Figure 4.7.

2.4.2 Membrane response to arbitrary actuator voltages

In order to determine the MMDM response to arbitrary actuator voltages a more rigorous analysis has to be made. A common approach is to assume that the membrane mirror is *linear*, meaning that the total shape of the mirror may be calculated as the *sum* of the mirror responses to the individual actuators. This is not strictly true but under certain conditions it is an adequate estimate. The mirror response to a unit exerted pressure from actuator j is $\mathcal{A}_j$. The function $\mathcal{A}_j$ is the *influence function* of actuator j. A 37 actuator mirror has 37 influence functions. The *linearity* of the mirror then implies

$$u = \sum_{j=1}^{37} p_j \mathcal{A}_j \tag{2.24}$$

where u is the membrane shape and p_j is the pressure exerted on the membrane by actuator j. Recall that the pressure is proportional to the *square* of the actuator voltages. There are several ways to find the influence functions. A Finite Element analysis could of course be employed but in this thesis another approach has been chosen. The method makes an approximation of the actuator structure and then calculates the influence functions *analytically*. The scheme involves a few steps and is treated in Appendix A. The actuator approximation is illustrated in Figure A.1. An important result is that the membrane deflection is simply calculated in a matrix operation,

$$\mathbf{u} = \mathbf{AP}. \tag{2.25}$$

The elements of **P** are the pressures that are exerted by the actuators and the columns of **A** are the influence functions. If the membrane surface is defined by M surface points and the mirror has 37 actuators, the influence matrix **A** is a Mx37 matrix and membrane deflection vector, **u**, is a Mx1 column vector. The

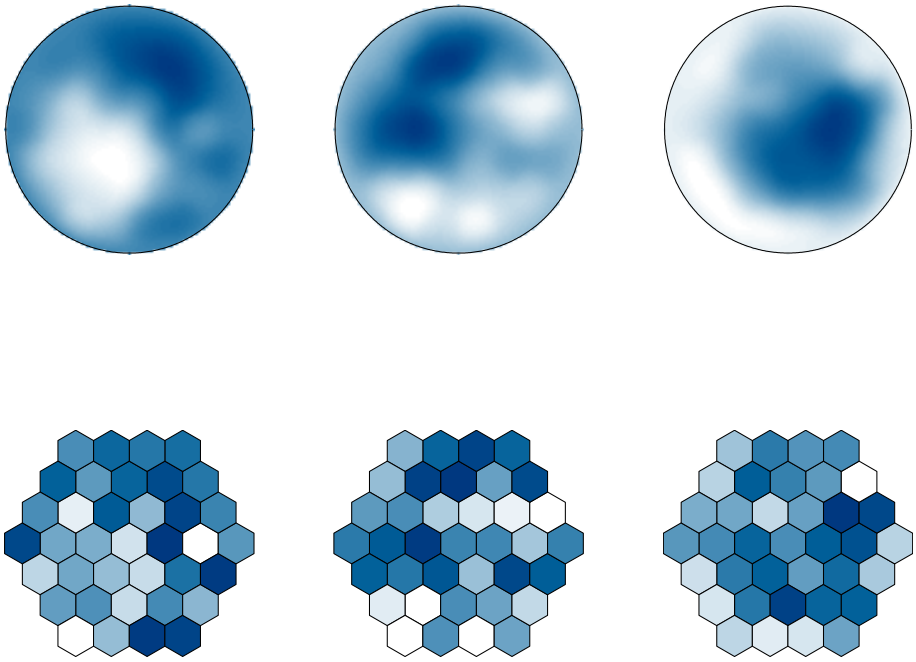

Figure 2.13: Mirror membrane response to random actuator pressures. The normalized pressures are in the range ±1 and the hexagonal patterns shows some random actuator combinations. Normalized pressure −1 corresponds to blue color and a normalized pressure +1 is white. The corresponding membrane deflections are also shown and a large negative deflection is blue and a large positive deflection is white.

pressure vector, $\mathbf{P}$, is a 37x1 column vector. If a bias voltage, V_b, is applied to the mirror electrode, the pressure from actuator j is

$$p_j = \epsilon\epsilon_0 \left(\frac{V_b^2}{\delta^2} - \frac{V_j^2}{d^2} \right) \tag{2.26}$$

where δ is the membrane thickness. Thus, a bias voltage would allow pressures of any sign. The manufacturer does not recommend a bias voltage but gives no explanation why. In the following it is assumed that a small bias voltage is applied to the mirror electrode in order to allow actuator pressures of any sign.

The influence matrix $\mathbf{A}$ may be normalized so that the deflection when maximum pressure is applied to all actuators equals an experimentally measured value (the results from this measurement are summarized in Figure 4.7). Equation 2.25 enables calculations of the membrane shape for *all* possible combinations of actuator pressures. Figure 2.10–2.12 displays the membrane response when maximum pressure is applied to a single actuator and no pressure is applied to the other actuators. Figure 2.13 presents other possible shapes of the membrane. The applied actuator pressures are chosen randomly in the range $\pm p_{max}$, where p_{max} is the maximum pressure.

2.4.3 Application of the model

The main purpose for calculating the influence functions was the possibility of an *open-loop* membrane configuration. Open-loop means in this case without feedback or, without a wavefront sensor. With an accurate analysis of the membrane response it would be possible to, at least approximately, modulate the phase of an optical wave in a controlled manner. Compensating for an aberration means introducing the same aberration but with opposite sign. Looking again at the primary aberrations in Table 2.1 we have a mathematical description of astigmatism, coma and spherical aberration. If the MMDM can be configured to induce for example astigmatism, it could also be used to *correct* for astigmatism.

The matrix formulation of the mirror response to actuator voltages makes it possible to perform a least squares fit to an arbitrary shape of the mirror. Let the desired shape, possibly one of the primary aberrations, be $\mathbf{u}$. The solution to equation 2.25 is then in a *least-squares* sense

$$\mathbf{P} = (\mathbf{A}^T\mathbf{A})^{-1}\mathbf{A}^T\mathbf{u} \tag{2.27}$$

Which makes it possible to find the pressures required to make the mirror induce a certain phase. When performing the least-squares fit in equation 2.27, the area over which the fit is performed is determined by the influence functions. If they are defined over the whole membrane structure, the fit is performed over the whole membrane structure. The membrane is clamped at the edges which restricts its motion and in the experiments, described in Chapter 5, only the central 19 actuators were illuminated. The least-squares fit in equation 2.27 should take this into account. In order to do so, the influence functions in matrix $\mathbf{A}$ should only be defined within a circle on the membrane that corresponds to the central 19 actuators.

Figure 2.14 shows a least squares fit of the membrane shape to the astigmatic shape, given in Table 2.1 with only the 19 central actuators illuminated. Equation 2.27 gives the electrode pressures and equation 2.25 gives the resulting shape of the membrane. The method was also applied in order to obtain a comatic shape of the central membrane mirror. Figure 2.15 displays the results. The membrane follows the coma template inside the illuminated area. Coma and astigmatism are low-order aberrations and varies slowly over the aperture. The membrane shape was also fitted to a number of random surfaces with different spatial frequencies. The results are illustrated in Figures 2.16–2.18. In Figure 2.16, the spatial period of the reference surface is 7L, where L is the center-to-center distance between two actuator. The membrane fits perfectly to the reference inside the illuminated area. In Figure 2.17, the period of the reference random surface is 3.5L and the membrane shape still fits to the reference inside the illuminated circle. In Figure 2.18 the spatial period of the reference surface is 2.33L. But, in Figure 2.19, the spatial period is 1.75L. Obviously, the membrane is not able to produce such high spatial frequencies. The reason is that two actuators are needed for one period since the gradient of the surface changes sign two times over this distance.

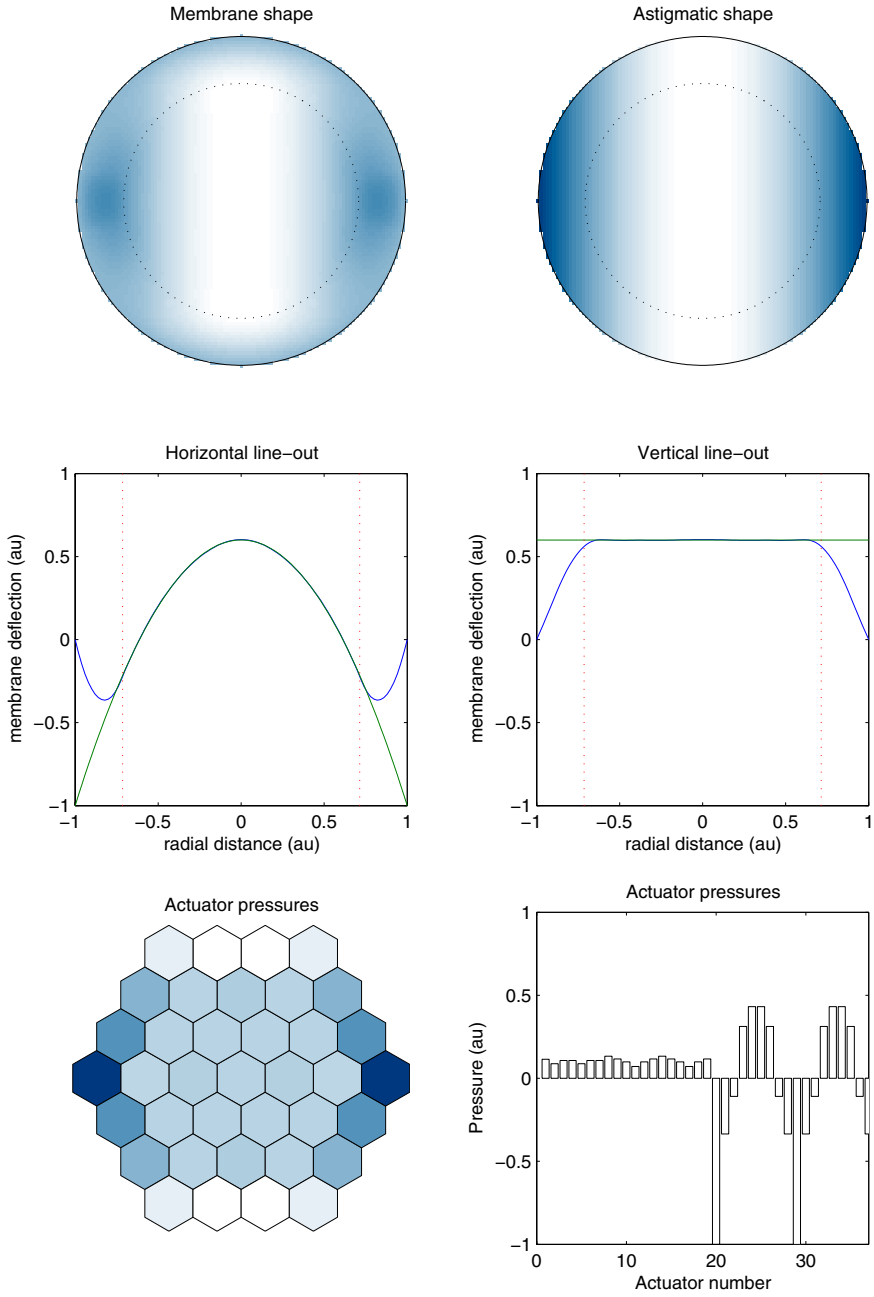

Figure 2.14: Least-squares fit of the actuator pressures in order to obtain an *astigmatic* shape in the central illuminated area, within the dot-lined circle. The top images display the reference and membrane surfaces. A normalized deflection of -1 is blue and a normalized deflection of +1 is white. Vertical and horizontal line-outs of the reference and the membrane surfaces are displayed in the middle diagrams. The membrane deflection is zero at the edges. The lowest diagrams display the calculated actuator pressures. A normalized pressure of -1 is blue and a normalized pressure of +1 is white.

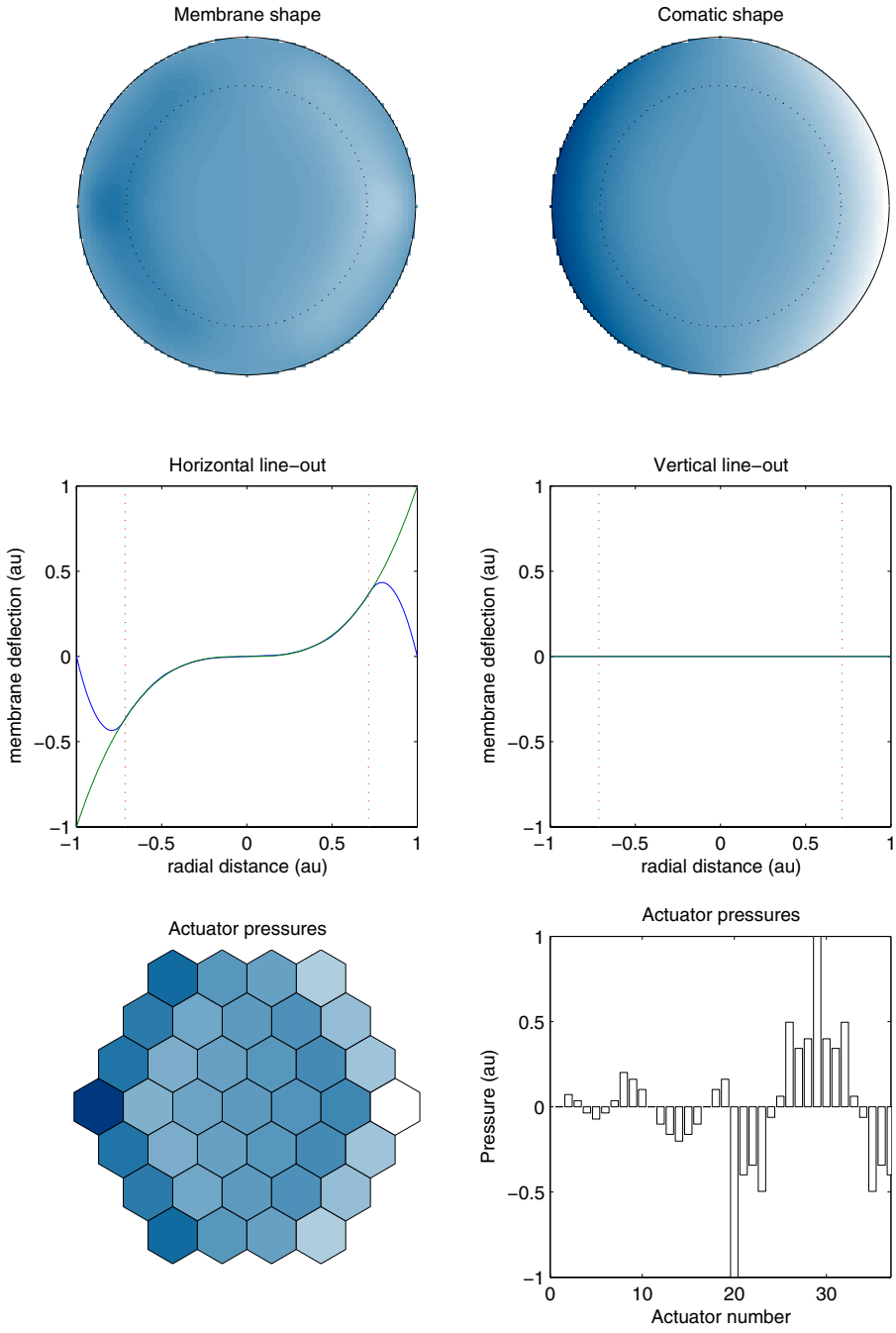

Figure 2.15: Least-squares fit of the actuator pressures in order to obtain a *comatic* shape in the central illuminated area.

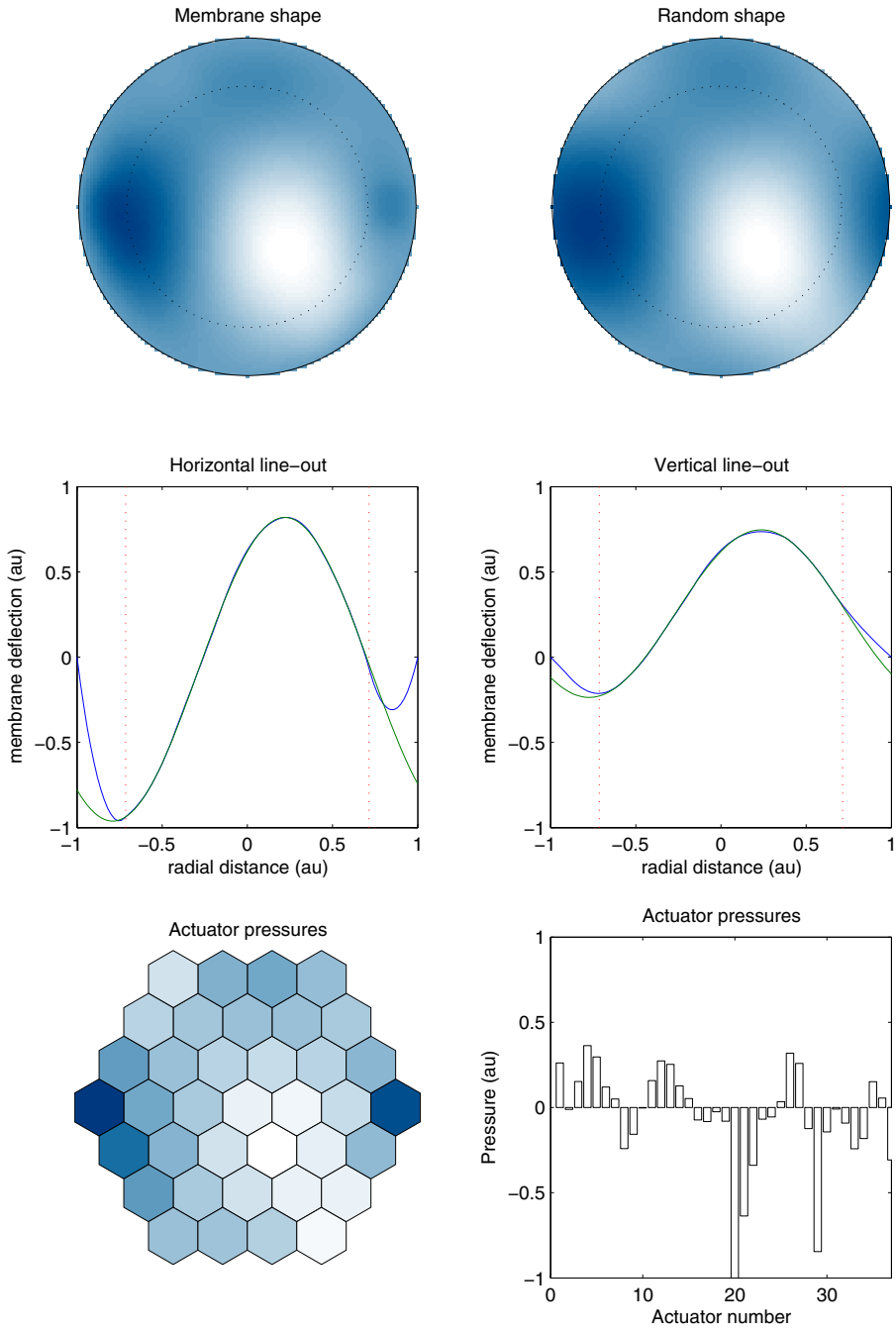

Figure 2.16: Least-squares fit of the actuator pressures to a random surface. The spatial period of the reference surface is 7L, where L is the center-to-center distance between two actuators.

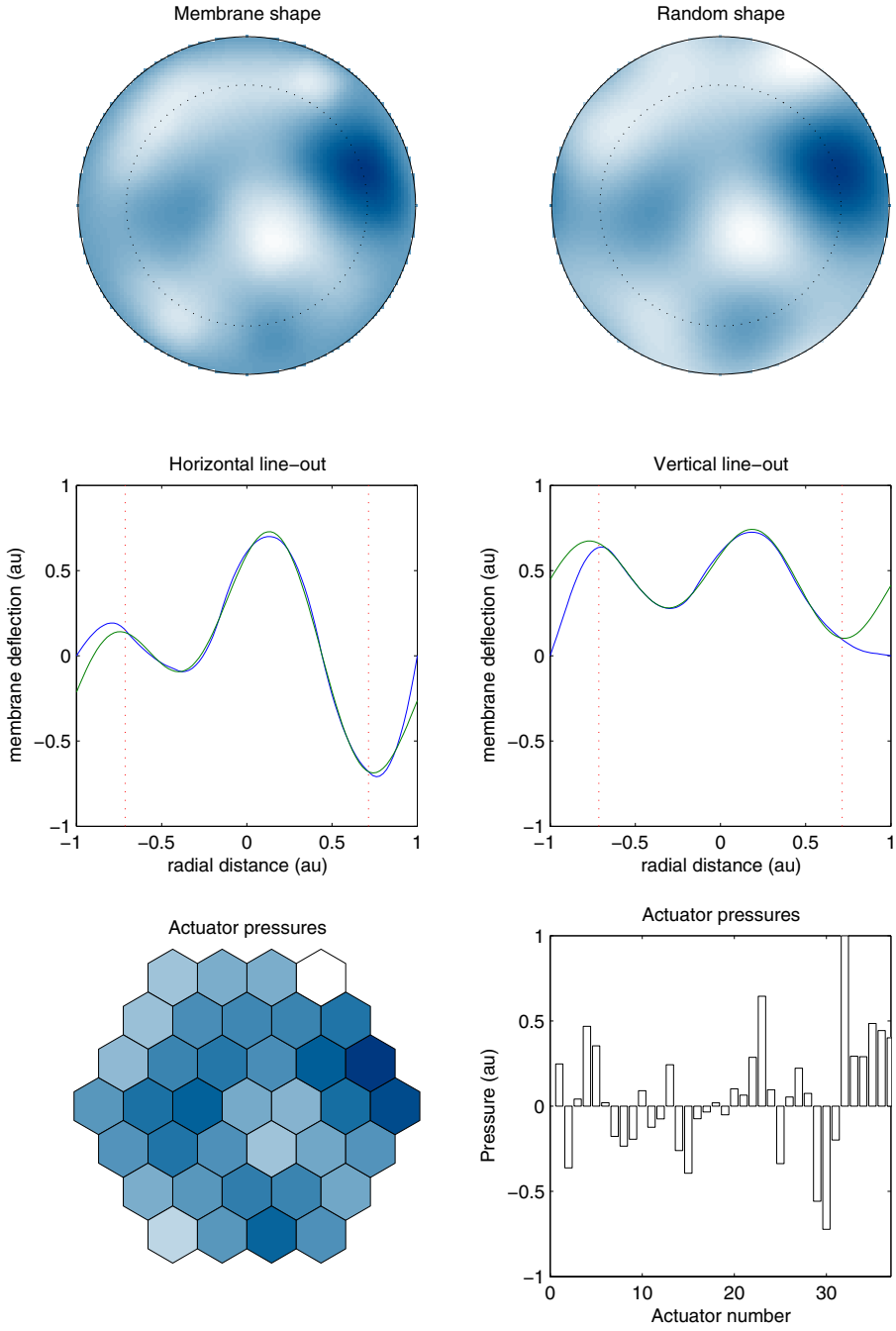

Figure 2.17: Least-squares fit of the actuator pressures to a random surface. The spatial period is 7L/2=3.5L.

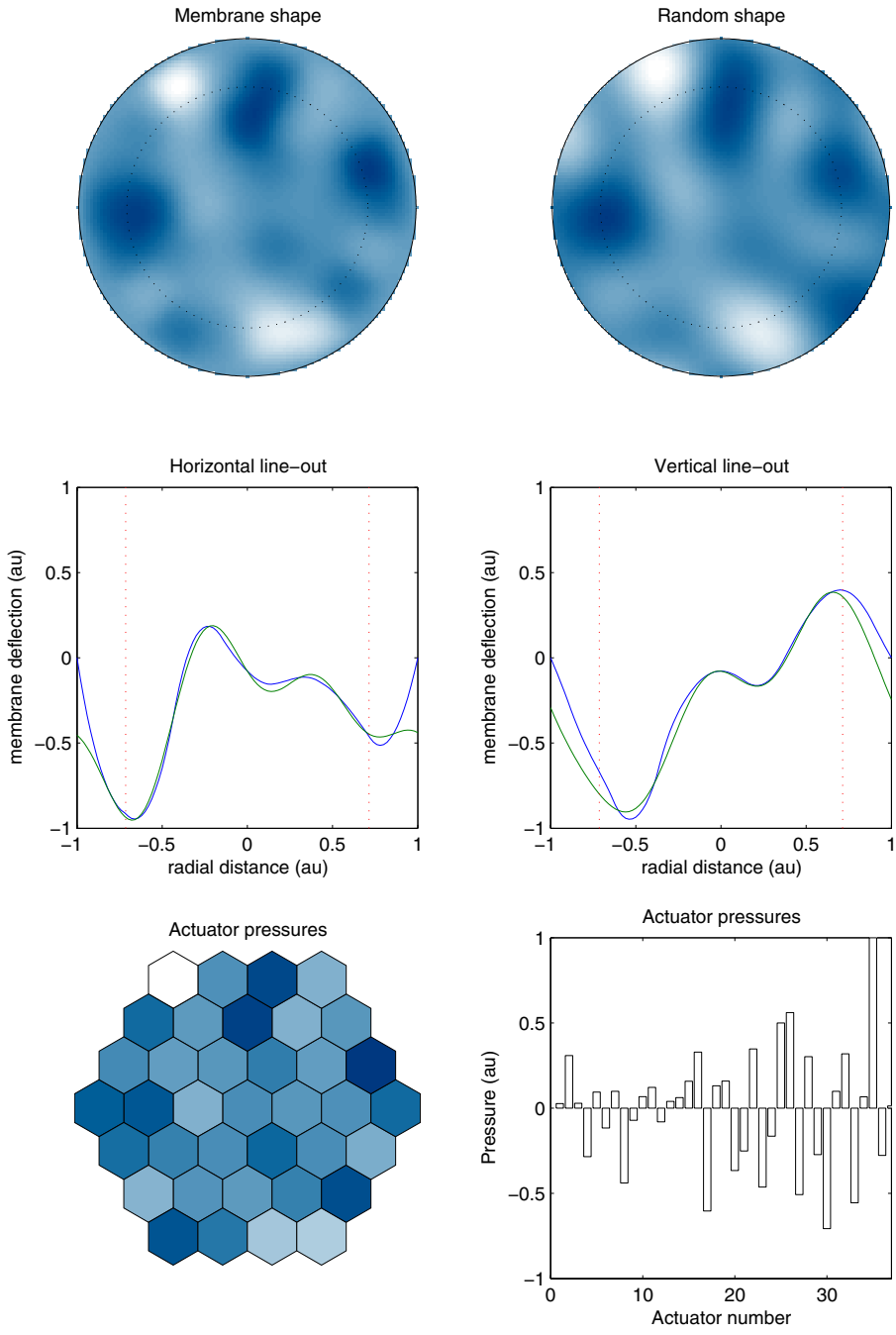

Figure 2.18: Least-squares fit of the actuator pressures to a random surface. The spatial period is 7L/3=2.33L.

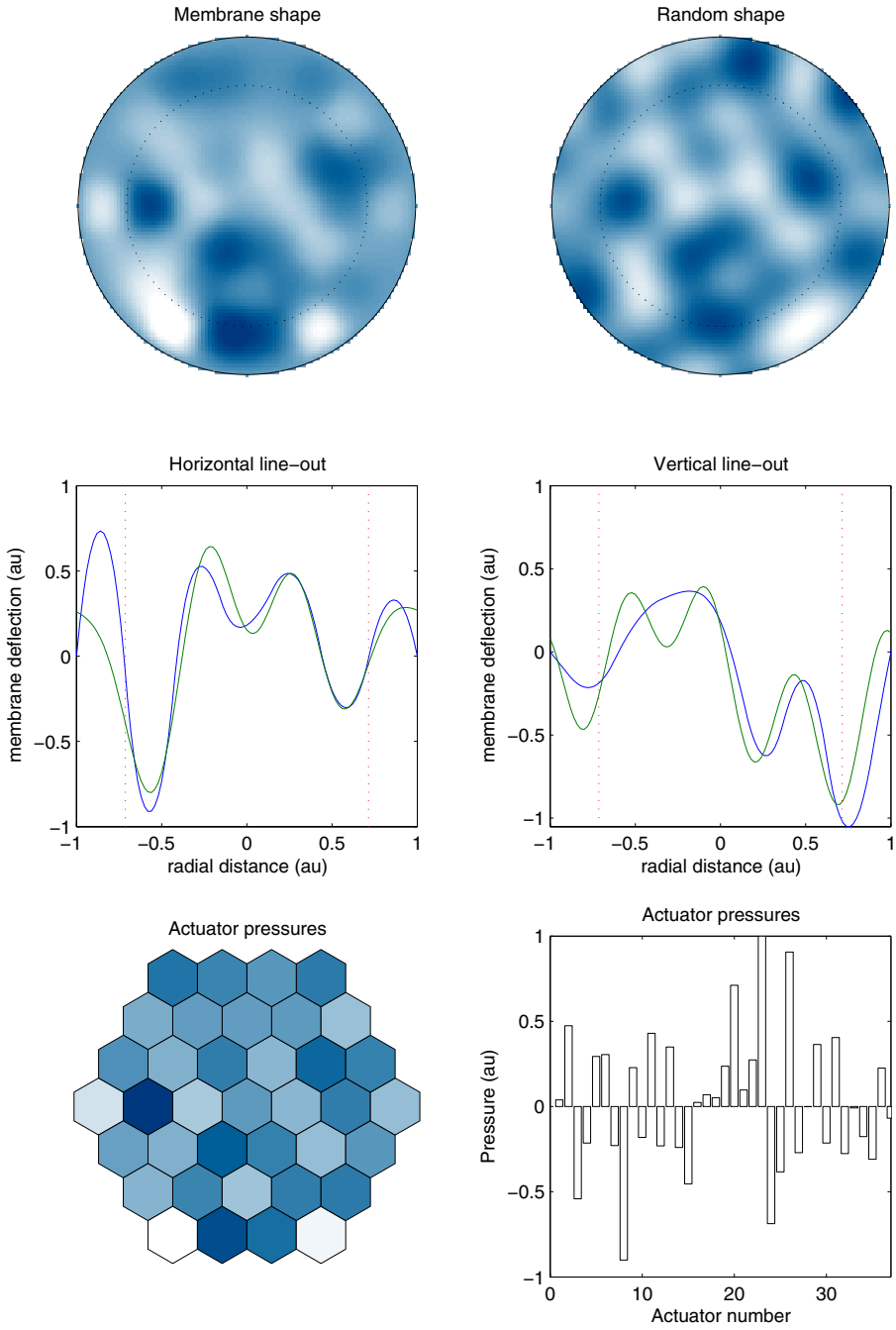

Figure 2.19: Least-squares fit of the actuator pressures to a random reference surface. The spatial period is 7L/4=1.75L. The membrane is not able to reproduce the reference random surface since two actuators/period are needed.

Chapter 3

Genetic algorithms

In order to configure the desired shape of a deformable mirror, conventional adaptive optics uses a wavefront sensor to calibrate the mirror response. The wavefront sensor measures the unwanted wavefront distortion and the calibrated deformable mirror may correct this distortion in only a few iterations or even in a single shot. In this thesis, however, a method for configuration of the mirror surface that *omits* the wavefront sensor has been investigated. The scheme employs a detection system and a blind optimization algorithm. The detection system delivers a signal that somehow measures how well the mirror is performing. The algorithm strives to optimize that signal by manipulating the mirror surface. The signal may for instance be the focal spot-size or peak intensity. The mirror surface is controlled by the mirror actuators so the search space that has to be scanned is quite large. The mirror used in this thesis work has 37 actuators and each actuator may be assigned 256 different values so, in order to search the whole space, 256^{37} evaluations of the performance are needed. This is of course impossible so the optimization must use some smart method that is able to search very large spaces in limited time. Local extrema could also pose severe problems for an optimization algorithm since it could get stuck in a local maximum and fail to find the global optimum.

A genetic algorithm was chosen for the optimization since it has already been successfully employed for blind configuration of the shape of a deformable mirror [2] [1] [3] [6] [15] [27]. The *Stochastic Parallel Gradient Descent* (SPGD) search method has also been employed for optimization of the deformable mirror control signals [18] [25]. The search performed by a genetic algorithm is parallel in its nature and it has successfully solved complicated many-variable optimization problems where other search methods have failed. The aim for this chapter is to introduce the different components of a genetic algorithm in general. A description of the specific computerized implementation used in the experiments will follow in Section 4.4

3.1 Introduction

The *genetic algorithm* (GA) provides an approach to optimization that is based loosely on the idea of simulated evolution. As a tool for search and optimization, GAs have rapidly found new applications and are currently used in many

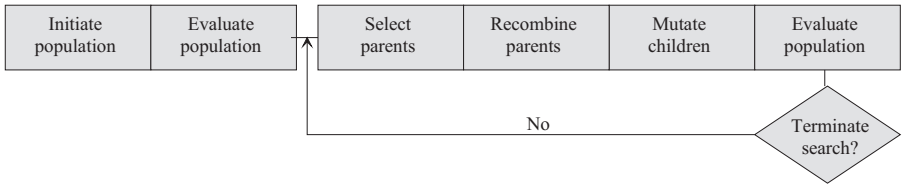

Figure 3.1: Basic structure of a genetic algorithm. First, the population is randomly initiated. Then, all individuals are evaluated by the fitness function. A selection mechanism selects some of the best adapted individuals and through a reproductive rule, the individuals are mated and producing children. The children are randomly mutated and finally evaluated by the fitness function. The process is iteratively repeated until a stop criterion is reached.

different fields. The heart of the GA is Darwin's principle of natural selection and the survival of the fittest. Thus the numerical solution to a specific problem obtained by the GA is not based on mathematical or physical considerations. This makes the GA very flexible and it may be applicable to many different kinds of problems. GAs are often successfully employed where other search methods or optimization methods fail to find a global optimum. This makes many people think of the GA as an all-purpose optimizer that kindly solves your 1000 variable nonlinear problem while you are having a cup of coffee. It should be stressed that unfortunately it is not that simple. There are many things to consider and many choices to make before implementing a GA. One should also consider other optimization methods that could be a faster or a more reliable way to solve a specific problem.

3.2 Implementation

GAs are inspired by the mechanisms of natural selection and the survival of the fittest. They employ analogies to genetic processes and natural evolution. In this context a proposed solution to a given problem would be the individual. An individual is represented by the set of parameters that must be specified to the problem. The parameters are the genes and the total set of parameters is the *chromosome*. How well the individual is adapted to the environment, that is how well it solves the problem, is described by a single-valued function, known as the *fitness function*. The evolution, as it is simulated by the GA, takes place in an isolated *population* of individuals. The population is iteratively updated and a subsequent generation is produced from the chromosomes of the current population through a *selection* and a *crossover* mechanism. The basic structure of a simple GA is shown in Figure 3.1.

3.2.1 Chromosome representation

The chromosome representation of an individual is fundamental and the representation should match the nature of the problem. In biology, the genes are coded in DNA (deoxyribonucleid acid). In turn DNA consists of four building blocks, adenine (A), guanine(G), cytosine(C) and thymine(T). Thus, the genetic representation of an individual employs a four letter alphabet, $\{A, C, T, G\}$.

When implementing a GA for optimization a common representation exploits a binary alphabet, $\{0, 1\}$. The chromosome is in this case the concatenated binary representations of all variables.

var	int	bin
x_1	7	0111
x_2	13	1101
x_3	3	0011

$\Rightarrow$

chromosome
011111010011

Table 3.1: Binary encoding a three variable individual. Each variable is an integer in the interval $[0, 15]$. A binary representation use 4 bits for each integer.

3.2.2 Fitness and objective functions

The objective function measures how well an individual solves the problem. This is the link that relates the GA to the problem of interest. It takes an individual as input and gives a real number as output. When all the individuals have been evaluated their objective values spread over a certain range. Some individuals will have very low objective values and some individuals have very high objective values. To maintain or control uniformity their objective values are mapped into their *fitness* values by the fitness function.

Linear scaling. The objective value, o_i of chromosome i is linearly scaled to the fitness value f_i,

$$f_i = ao_i + b. \tag{3.1}$$

Power scaling. The fitness value is a power of the objective value,

$$f_i = o_i^k, \tag{3.2}$$

where a high value of k spreads the fitness values, increasing the significance of a high objective value. In order to increase the precision of the GA k could be dynamically controlled during the run. It could, for instance, be inversely proportional to the standard deviation of the objective values of the population.

3.2.3 Selection Methods

In each cycle of genetic operation a subsequent population is generated from the chromosomes of the current population. New individuals are created through a mating process from two parent individuals that are chosen from the current population. To generate a good offspring a good selection mechanism is necessary.

Roulette wheel mechanism

The *roulette wheel* selection mechanism is a very common technique for selection. In this scheme individuals are stochastically selected to produce an offspring with a probability being proportional to their fitness value. The probability for selection for individual i equals to

$$p_i = \frac{f_i}{\sum_i f_i}. \tag{3.3}$$

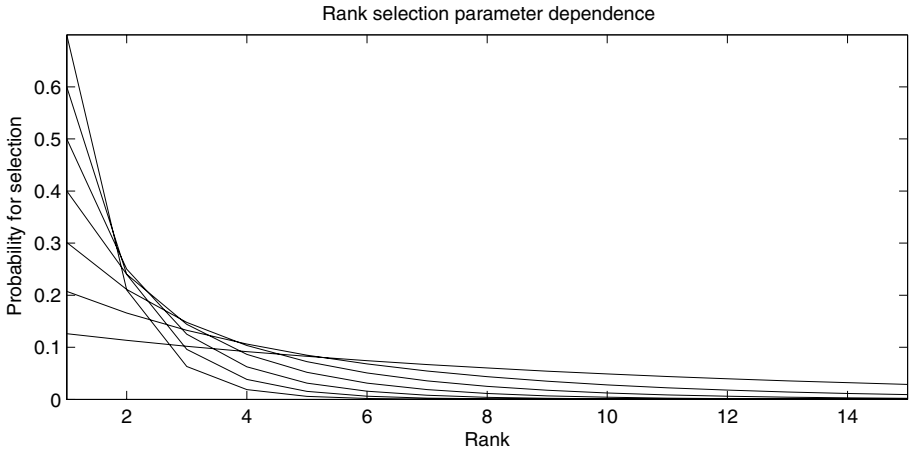

Figure 3.2: The probability for selection when employing rank selection method. In this example, the population consists of 15 individuals. The probability for selection depends on rank and the selection parameter p, see equation 3.4. In this diagram, the parameter p was 0.1, 0.2, 0.3, 0.4, 0.5 0.6 and 0.7. A high value of p favors the highest ranked individuals.

Rank selection

The individuals are ranked according to their fitness values. First, the individuals in the population are sorted with respect to their fitness so that the best fit individual is at the first position in the list. The rank, r_i, of individual i is then its position in this list. In this approach the best individual in a population, according to the fitness function, has the rank 1. The worst individual has the rank N, where N is the number of individuals in the population. The selection process steps through the rank list. Each individual has a probability for selection p, provided that the lower ranked individuals were *not* selected. The probability for selection for an individual with rank r_i is then

$$p_i = \frac{p(1-p)^{r_i-1}}{\sum_{r_i} p(1-p)^{r_i-1}} = \frac{p(1-p)^{r_i-1}}{1-(1-p)^N}. \tag{3.4}$$

The rank selection method enables the importance of fitness to be tuned. The probability for selection depends on the value of p. A low value of p gives approximately equal probability for selection for all individuals. A high value p gives a high probability for selection for the lowest ranked individuals and a low probability for selection for the highest ranked individuals. This is depicted in Figure 3.2 where the probability for selection, that is equation 3.4, is plotted for various p.

Rank-space selection

As the population evolves, individuals with high fitness values tend to produce more offspring than others. Less fitted individuals are wiped out, resulting in a uniformity of the population. If the GA is operating in an environment with many local minima or maxima the search for the globally most fit individual may fail. One may then take into account the *diversity* of the individuals,

giving less fit individuals far away from the better ones a bigger probability for surviving. The rank-space method assigns two intermediate ranking values to each individual. The first value, x_i, is the rank with respect to the *fitness* and the second, d_i, is the rank of the individual with respect to the *distance* between the individual i and the best individual in the population.

When solving a two-variable maximization problem, the fitness function is a 2-dimensional function, $f(x, y)$, and an individual is a point (x, y). The best individual is the point that gives the highest fitness value ($f(x_{best}, y_{best}) > f(x_i, y_i)$) for all individuals i. The *distance* between the best individual and individual i is in a cartesian space

$$\delta_i = \sqrt{(x_{best} - x_i)^2 + (y_{best} - y_i)^2}. \tag{3.5}$$

The intermediate ranking value, d_i, is then the rank of individual i with respect to the value δ_i. The sum of these intermediate rankings is

$$s_i = x_i + \rho d_i, \tag{3.6}$$

where ρ is some number, determining the significance of diversity. The *final* rank, r_i, of an individual is computed as the rank with respect to this weighted sum, s_i. The parameter ρ may be changed dynamically during execution of the algorithm so that the importance of diversity diminishes as the algorithm converges. The probability for selection is computed from the final ranking of the individuals, r_i, as in equation 3.4.

3.2.4 Crossover

Crossover is the genetic operator that is responsible for the production of new individuals. It takes two parent individuals as input and gives two offspring individuals as output. Figure 3.3 illustrates the principle of the one point crossover mechanism. The crossover operator randomly selects a crossover point. The portions of the two chromosomes beyond this point are swapped, producing two offspring. Thus an offspring contains genetic information from both its parents. Multiple points for crossover may also be selected.

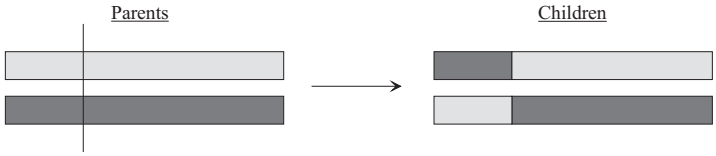

Figure 3.3: Crossover principle.

3.2.5 Mutation

Crossover is not the only operator that alters the genetic information of the population. A chromosome may also be subject to *mutation*. The mutation operator is applied to each offspring that is the result from the crossover mechanism. It alters each genome in the chromosome randomly with a small probability for mutation. In the bit string representation the mutation operator simply switch the genome between 0 and 1 but other representations may require a more complex mutation operator.

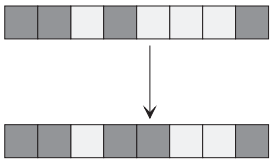

Figure 3.4: Mutation in the bit string representation.

3.2.6 Elitism

The selection mechanism gives well fit individuals a high probability to reproduce. The reproduction involves crossover and mutation. None of the operators conserve genetic information so when a new generation replace its parent population, the so far best individual may be lost. This loss of information slows down the convergence rate significantly but it may be circumvented through an elitist scheme. Elitism always saves the best, or some of the best fit individuals. The elite is transferred to the subsequent generation unaltered, that is they are not mutated. Elitism makes it impossible for the GA to lose good solutions already found and should always be employed.

Chapter 4

Experimental setup and methods

4.1 Laser systems

The adaptive optics system was tested using two differ laser systems. A HeNe-laser, delivering a continuous wave (CW) laser beam, was used for initial tests and characterizations of the deformable mirror as well as for software development. A Ti:sapphire laser, delivering ultrashort pulses of laser light in the femtosecond domain, was used in the final, more realistic tests of the system. From an adaptive optics point of view, however, the main difference between the laser systems was not the extreme properties of the Ti:sapphire laser pulses compared to the CW of the HeNe laser, but the mere fact that the adaptive optics had to be synchronized to the 10 Hz pulses of the Ti:sapphire laser. Another important difference to consider when going from the continuous laser to the pulsed laser was stability. Large pulse-to-pulse fluctuations of the Ti:sapphire laser contrasted the stability of the HeNe-laser. This section gives a *brief* description of these sources of light.

4.1.1 HeNe-laser lasers

The continuous laser light, emitted from a HeNe-laser is the out-coupled standing waves that are present inside the laser cavity. Several longitudinal modes, or standing waves, exist inside the cavity simultaneously. The laser cavity has the length L and possible standing waves have frequencies [21]

$$\upsilon = \frac{c}{2L} \cdot n \ , \quad n = 1, 2, ... \tag{4.1}$$

The amplifying medium in the laser, in this case a mixture of helium and neon gas, can not amplify all these frequencies so the actual output of the laser is a weighted sum of the longitudinal modes. The weighing envelope is the gain of the medium. The frequencies of the longitudinal modes in the HeNe-laser cavity depend on the length of the cavity. So, if the length of the cavity is continuously increased, the frequencies of the standing waves will decrease. The gain envelope is however centered around $\lambda = 633$ nm and the HeNe-mixture

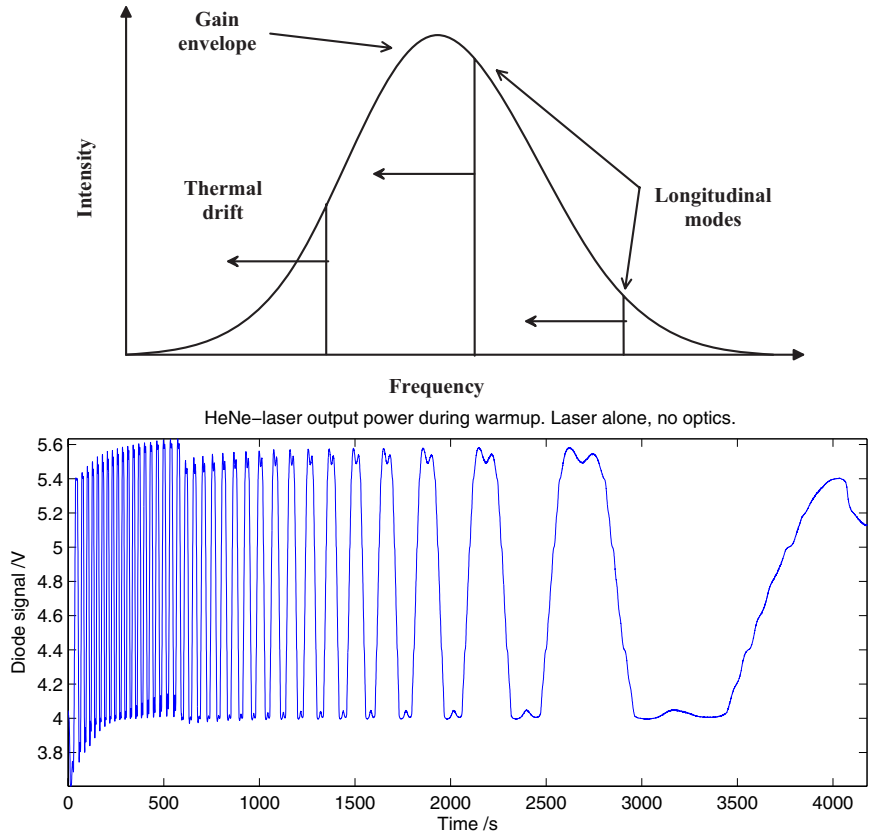

Figure 4.1: Short term variations of the HeNe-laser output power. The upper diagram displays a typical gain profile of a HeNe-laser. As the cavity expands, the longitudinal modes will drift across the gain envelope. The total power of the laser depends on where the modes are positioned under the gain profile. The lower diagram shows the results from a measurement of the output power during the laser warmup.

will amplify the same frequencies so the total output of the laser will vary as the modes wander across the gain profile.

This is what happens when the laser is switched on. As the laser tube heats and expands, the modes will drift across the 1.5GHz wide gain curve. In a 30cm cavity the mode separation is 0.5GHz so, two or three modes may be amplified. Depending on where the modes are located under the gain envelope, the output power of the laser will vary. This short term output power variation during warm-up was measured for the HeNe-laser that was used in the experiments in Chapter 5. A diode measured the laser beam power, the diode voltage was registered by an oscilloscope and the measurement was continuously transferred to the laboratory computer that collected the data. The result is shown in Figure 4.1. The measurement was not calibrated so Figure 4.1 displays the raw data, that is the diode voltage. The variations were not of a single frequency, but included a double-dip behavior. This may be the result of slightly different gain in the different directions of polarization.

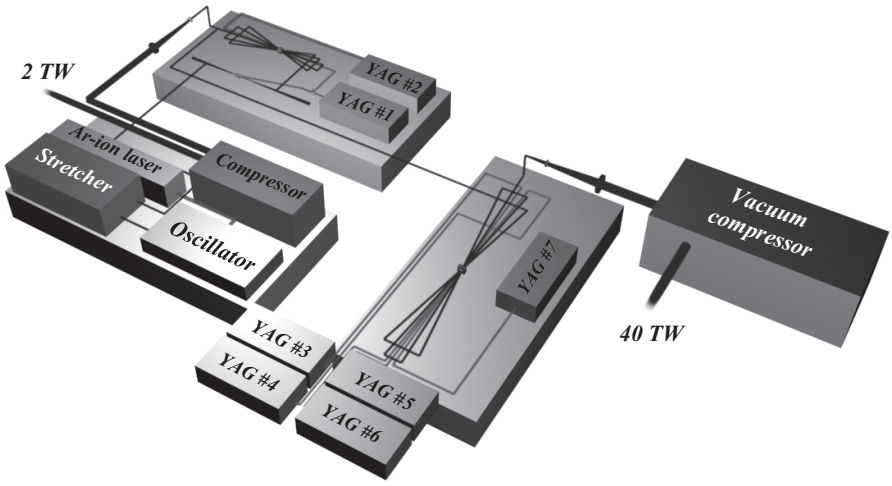

Figure 4.2: A schematic view of the high-power laser system at Lund Institute of Technology that was used for some of the experiments in Chapter 5. This image and many interesting features concerning the extreme irradiance that may be produced by this laser may be found in [12].

4.1.2 The high-power Ti:sapphire laser

A schematic view of the high-power laser system that was used for some of the experiments in Chapter 5 is illustrated in Figure 4.2. The system relies on the generation and amplification of very short pulses in the femtosecond domain. The idea is to achieve high peak power not through high pulse energies, but through short duration of the pulses. Such short pulses may be produced through *modelocking* [21], where several longitudinal modes are locked in phase. The output from a *modelocked* laser is a train of very short pulses. The length of the pulses depends on the number of modes that are locked to each other and the number of cavity modes depends on the width of the gain profile. This is the reason why broad-band gain materials, such as the Ti:sapphire crystal (centered around $\lambda = 800$ nm), are used in modelocked lasers. The *oscillator* in Figure 4.2 is a modelocked Ti:sapphire laser that is pumped by an continuous wave Ar-ion laser. The oscillator pulses are then amplified. Very short pulses may generate very high peak powers, even at low pulse energies. At some point the high intensities of the laser pulses may damage the optics and crystals that are used in the setup, making further amplification impossible. This limit was pushed forward by the innovative design of the *chirped pulse amplification* (CPA). In a CPA laser chain, the short oscillator pulses are stretched in time, from the femtosecond to the picosecond domain, before they are amplified. This reduces the peak power of the pulses and enables massive amplification of the laser-pulse. After amplification, the pulses are recompressed to the femtosecond domain and focused on the target. In the CPA design, the pulses are stretched by an arrangement of gratings. Since the very short modelocked pulses contain many wavelengths, the gratings may be arranged so that the short wavelengths have a longer optical path-length through the stretcher than the long wavelengths. Consequently, the longer wavelengths will exit the stretcher before the shorter

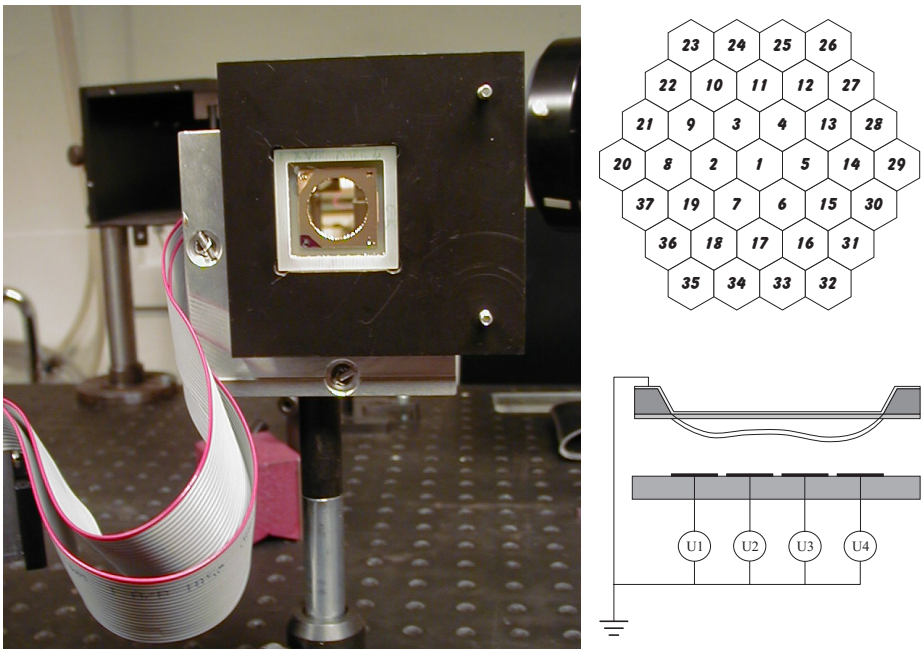

Figure 4.3: The deformable mirror that was used in the experiments. The left image shows the mirror in its position in the experiments. To the right, the actuator structure and the mirror working principle are illustrated.

wavelengths, resulting in a longer pulse. A similar arrangement of gratings constitutes the compressor where the shorter wavelengths experience a shorter optical path than the longer wavelengths. The pulses are thus recompressed when they exit the compressor. Each of the two arms in the terawatt laser-system in Lund has its own compressor arrangement. The multi-terawatt arm is seeded with pulses from the terawatt laser. The pulses are amplified in a 4-pass Ti:sapphire butterfly amplifier from 100 mJ to almost 2 J, producing a pulse peak power after compression of 40 TW. The experiments in Chapter 5 were performed on the terawatt-arm. Only one of the two pump lasers was used since high pulse energy was not required.

4.2 The deformable mirror

The mirror that was used for wavefront correction belongs to the class of deformable mirrors named micromachined membrane deformable mirrors (MMDM). It has 37 electrostatic hexagonal actuators and is coated with gold. The mirror is driven by two 20-channel high-voltage amplifier boards and controlled by two 20-channel DA control boards. The MMDM, the high voltage boards and the DAC boards were lent to the Atomic Physics Department from Laboratoire d'Optique Appliquée, Palaiseau, France.

Membrane reflective coating	Gold
Aperture shape	Circular
Aperture dimensions	15mm diameter
Number of actuators	37
Actuator center-center distance	1,75mm
Actuator-Membrane distance	$75\mu m$
Membrane thickness	$0,75\mu m$
Membrane material	Si_3Ni_4
Control voltages	0..255V
Initial P-V deviation from plane	less than $0.6\mu m$
Main initial aberration	astigmatism
Frequency range	0:1000Hz
Maximum deflection of the mirror center	$5.4\mu m$
Maximum optical load	$3W/cm^2$ at 633nm

Table 4.1: Technical specifications of the Micromachined Membrane Deformable Mirror that was used in the experiments in Chapter 5.

4.2.1 Micromachined Membrane Deformable Mirror

The MMDM consists of a thin reflective membrane that is stretched over an array of electrodes, see Figure 4.3. The membrane can be electrically grounded and when voltage is applied to the electrode structure, the membrane is electrostatically attracted towards the electrodes and locally deformed. The device is commercially available from OKO Technologies and consists of a silicon chip mounted over a PCB holder (printed circuit board). The electrodes are patterned in the metallization layer of the PCB. The PCB also contains connectors to the driver units.

The active part of the MMDM is a low-stress nitride membrane. The membrane is made reflective and conductive by coating the etched side with a thin layer of evaporated gold. Other coatings available from OKO Technologies are aluminium, silver and multilayer laser coatings. The fabrication sequence for the nitride membrane is as follows. A thin layer ($0.5\mu m$) [24] of silicon nitride is deposited on the surface of a silicon wafer. Selective etchants removes the silicon substrate but leaves the nitride layer intact. The shape of the membrane boundary is determined in the etching process. Square, as well as circular membranes has been successfully fabricated. According to Gleb Vdovin at OKO Technologies, silicon nitride was chosen as membrane material for the following reasons [22]:

- Nitride is a mechanically strong material, compatible with microelectronic processing. Fabrication of nitride membranes with a comparatively large, up to 2,5 cm, diameter is possible.
- Nitride deposition allows precise control of the stress in the nitride layer. When the silicon substrate is etched away, the shape of the nitride membrane depends only on the boundary conditions. Since it covers an opening in an optically flat silicon wafer, the membrane is at least as flat as the surface of the substrate.
- Selective etchants does not damage the nitride layer so the membrane have

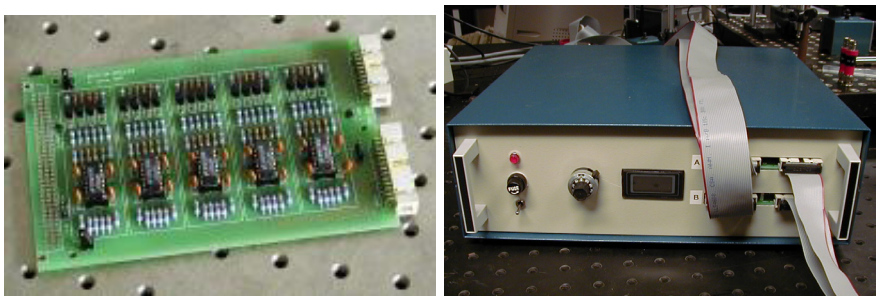

Figure 4.4: The high-voltage amplifier boards were installed in a separate rack.

a very low roughness since it replicates the polished silicon wafer. Thus a good optical quality is ensured when the etched side of the membrane is coated with the reflective material.

- The metal layer on top of the membrane is used as a capacitor plate for the electrostatic control of the mirror shape. Silicon nitride is a good insulator which reduces the risk for short circuit, even if the membrane sticks to the electrode structure.

The 37 hexagonal actuators of the MMDM are patterned in the metallization layer of the PCB, see Figure 4.3. The center-to-center distance between the actuators is 1,8mm. The whole actuator structure was located within a 12mm circle. The actuators are connected to the conducting tracks on the back side of the PCB through metalized holes. These holes, or vias, reduce air damping and extend the operational frequency response up to 1kHz. The temporal response of the mirror was not a constraint to the experiments in Chapter 5 since the detection system operated on a much lower frequency and the wavefront that was manipulated was fairly static. Aberrations that varies rapidly, such as turbulence in the medium of propagation, requires much faster acquisition and correction rates so a mirror with a temporal response of 1kHz may in fact be necessary for some applications.

The circular membrane is clamped at its edges. This restricts the motion of the membrane and thus the possible wavefront manipulations. Therefore, only 9mm of the total 15mm membrane diameter was illuminated in the experiments in Chapter 5. The wavefront that was induced by the mirror was then not restricted to be constant at the aperture edges.

4.2.2 High-voltage amplifiers

The mirror is driven by two high-voltage amplifier boards, available from OKO technologies. Each board has 20 channels and each channel has a gain of 59, offering a voltage control range of [0...300V] for an input range of [0...5V]. One channel is used to ground the membrane, leaving in total 39 channels to control the mirror. The mirror has only 37 actuators so two channels are not used. The driver units and the high-voltage supplies were installed in a separate rack and connected to the mirror and to the control computer.

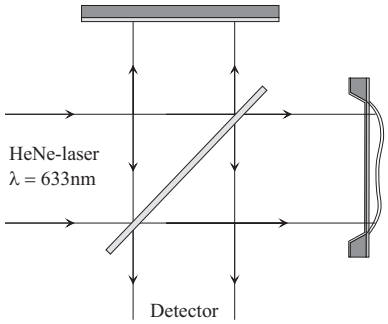

Figure 4.5: A Michelson interferometer was used to characterize the deformable mirror. The laser light comes in from the left and a beam-splitter divides the light in two arms. The beams are reflected by the plane and deformable mirrors. Since the optical paths of the two arms in the interferometer are different, an interference pattern appear when the beams are brought together again by the beam-splitter. A CCD-camera detects the resulting interference pattern.

4.2.3 Digital control boards

Two 24-output channel digital to analog converter (DAC) ISA boards were installed in the control computer. Each channel provide 8-bit resolution voltage control in the range [0V–2,5V...10V]. To match the high-voltage amplifier boards, four channels on each control board were disabled. One board was configured to control actuators 1-19 plus the membrane bias voltage. The other board controlled actuators 21-37 so two accessible channels were not used on the second board. The output range of the control boards was set to [0...5V].

The output voltages of the digital boards were controlled by the software in the control computer. A control byte [0...255] was sent to the output port corresponding to the controlled output channel. All channels had their own output ports. The output ports reserved for mirror control were chosen by adjusting the jumpers on the digital boards.

When the digital boards had been installed in the control computer, it was carefully verified that all channels responded correctly to the software commands. Eight channels on one board responded strangely. The error was identified as one of three DAC circuits on the board. Fortunately the DACs were replaceable and a DAC from the second board could replace the malfunctioning DAC. The board then functioned perfectly so there were no additional errors. A new DAC was ordered and installed on the control board.

4.2.4 Characterization of the MMDM

A Michelson interferometer was used to verify that the mirror was working properly. One of the mirrors in the Michelson interferometer was replaced by the deformable mirror, see Figure 4.5. The resulting interference pattern revealed the amplitude and localization of the deformations induced by individual actuators. Figure 4.6 displays some of the interference patterns recorded. The interferometer verified that all cables were drawn correctly and that all actuators responded correctly to the software control values.

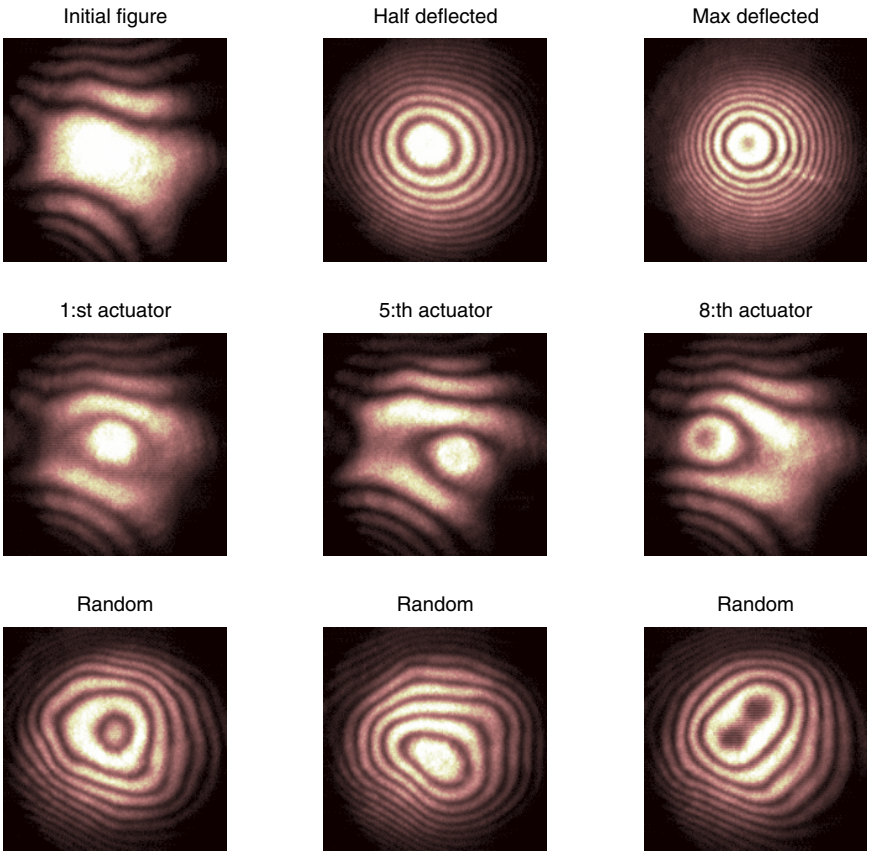

Figure 4.6: Mirror interferograms, recorded by the Michelson interferometer. Top-left interferogram is the initial figure of the mirror, when no voltage was applied to the actuators. Top-right interferogram displays the fully deflected membrane. The membrane response to actuators 1, 2 and 8 is displayed in the middle interferograms. The bottom interferograms display the membrane response to random actuator voltages.

The mirror response to identical actuator voltages was measured. Only a small spot in the mirror center was illuminated and a diode was placed in the interference pattern. The diode signal was registered by a digital oscilloscope and read into the control computer by a short LabView routine that also controlled the mirror. Identical control values were sent to all actuators. The diode signal was recorded as a function of actuator control values. Figure 4.7 shows the results. The wavelength of the HeNe-laser was 633 nm so each fringe represents a membrane deflection of 316 nm. The maximum membrane deflection was thus 5.4 μm. Between each peak and valley lies a membrane deflection of 158 nm so, by identifying the actuator values of these peaks and valleys, it is possible to plot the membrane deflection as a function of actuator control values, see Figure 4.7.

The mirror reaches its maximum deflection for an actuator signal 227 and larger values did not result in further deflection of the mirror center. The limitation was the high-voltage units. If the amplifier boards had been driven

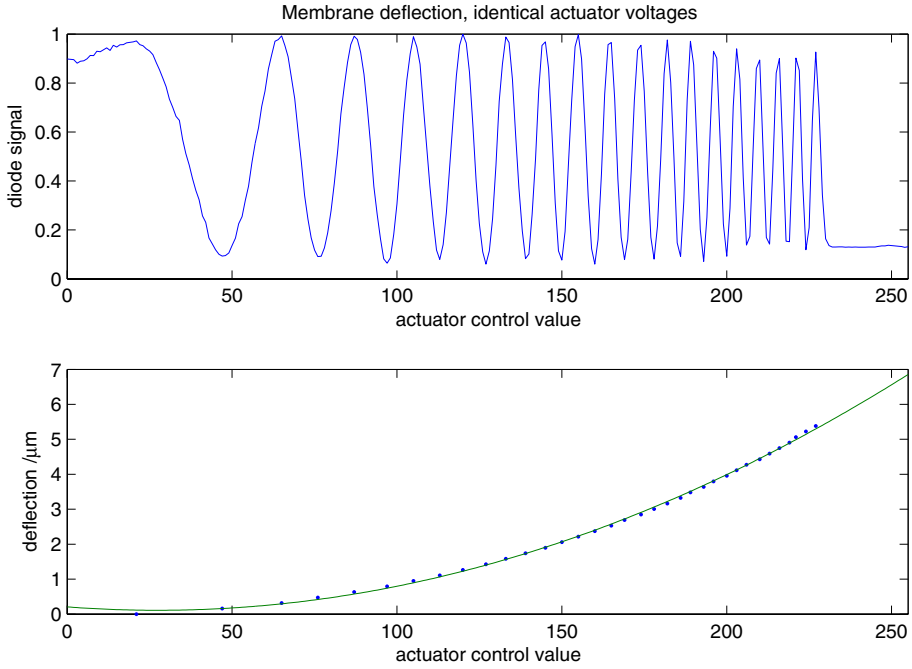

Figure 4.7: Deflection of the membrane center when all actuator voltages were equal. A parabolic curve was fitted to the data since the membrane deflection depends quadratically on the actuator voltages (see equation 2.23).

by a larger voltage, the maximum deflection of the mirror center could have been increased. If the fitted curve in Figure 4.7 is extrapolated, the maximum deflection reach $6.8\mu m$, but the mirror was already operated at the highest control voltage that was recommended by the manufacturer (255V) so the effects of using a higher driving voltage was never investigated.

4.3 Detection system

The purpose of the detection system was to supply the GA with the raw data necessary to judge whether a mirror configuration was good or bad. Two schemes were implemented. The first scheme was used for focusing optics with long focal lengths. A CCD-chip was in this case placed directly in the focal plane so it was necessary to attenuate the beam. A frame grabber board in the control computer registered the image of the focal spot and delivered it to the GA for analysis. The second scheme involved a diode and magnifying optics. The focal spot was magnified by a factor 310. A variable aperture was adjusted so only the central part of the magnified spot could illuminate the diode. The signal from this second diode was also registered by a digital oscilloscope and sent to the control computer through a RS-232 computer interface. Effects of laser power instabilities were suppressed by the use of a beam splitter, a lens and a second diode. The beam was split before the deformable mirror and one branch was focused by the lens on the second diode. The diode signal was reg-

1010111110000010001010001100100111111
0001100100100100010101110000011010100
1110001010011001000100101100000001011
0100101101001000011101000110110101101
0100010001111011111010100101100111100
0011000011000011010111110101111000011
1111010111010111001100111100110001011
1001100000011111101101010010101111111

Figure 4.8: Binary representation of a 37 variable random individual, using a 8-bit resolution for each variable.

istered by the oscilloscope and sent to the computer. It could then be used to normalize the signal from the first diode since it measured the total power of the beam.

4.4 Software implementation

All software was developed by the author and implemented in LabView, except the frame-grabber drivers, written in C/C++ by Anders Sjögren. These dynamically linked libraries (dll) communicated with the frame-grabber PCI computer board and supplied an image, captured by the CCD-camera, with background subtracted, to the optimization algorithm for evaluation. The LabView routines were linked and could be executed from a main routine.

4.4.1 Controlling the mirror

The shape of the MMDM was controlled by the software by sending control bytes [0...255] to the output ports corresponding to the mirror actuators. A routine was implemented in LabView that enabled *manual* control of the actuator values. Mirror configurations could also be loaded from or saved to a spreadsheet file. The routine monitored the *fitness* of the current mirror configuration according to the fitness function chosen for the genetic algorithm.

4.4.2 The genetic algorithm

The brain of the adaptive optics system was the genetic algorithm. Its design was crucial to the performance of the system and a lot of time was invested in the implementation of the GA and the subsequent debugging.

Representation

The mirror configuration was defined by 37 integer numbers in the interval [0...255] so a bit representation of the mirror configuration chromosome was natural. Each actuator value could be represented by a 8-bit sequence of binary digits. The chromosome was then the *concatenated* binary actuator values so each chromosome in the population was a binary string with $37 \cdot 8 = 296$ digits. A representation of a random chromosome is depicted in Figure 4.8. A routine that *encoded* the integer actuator values in a binary format and a routine that *decoded* the binary representation of a chromosome was implemented.

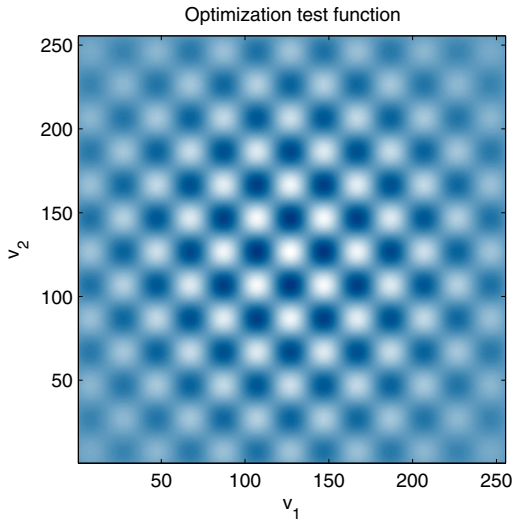

Figure 4.9: A function with many local maxima was used during the development of the genetic algorithm. In the diagram, blue represents f=0 and white represents f=2.

Fitness

Several schemes for evaluation of the mirror configuration were implemented. During code development mathematical functions with known optima were used to test the convergence of the algorithm. One of these was

$$f = 1 + \prod_{i=1}^{37} e^{-(\frac{v_i - 127}{127})^2} \cos \frac{\pi(v_i - 127)}{20} \tag{4.2}$$

where v_i denotes the value of actuator i. It has many local optima and a global maximum at $v_1 = ... = v_{37} = 127$. Therefore it was used during the development of the code to test the search performed by the GA. A 2-dimensional version of this function is illustrated in Figure 4.9.

Several fitness functions were implemented since there were two aims for the experiments in Chapter 5. One was to optimize the focal spot peak intensity and another was to tailor the focal spot intensity profile.

Focal spot peak intensity optimization. Two detection methods were used for focal spot peak intensity optimization. Either a CCD-camera was used in order to register the focal spot intensity profile or a diode was used to measure the total intensity of a central part of focal spot. Using the CCD-camera, the fitness function first demanded an image of the focal spot from the camera. The fitness function then simply returned the highest pixel value in this image. If the image was represented by a matrix $\mathcal{Z}$, with pixel indices (x, y), the fitness value was

$$f = \max_{x,y} \mathcal{Z}(x, y). \tag{4.3}$$

The camera had no gamma correction so the pixel values were proportional to intensity. Using a diode that measured intensity in the central part of the focal spot, the fitness was the voltage read-out from the diode, v_d,

$$f = v_d. \tag{4.4}$$

In order to overcome stability problems, a possibility to use two diodes was implemented. The second diode measured the *total* power of the beam and was used to normalize the measurement. The fitness was in this case calculated as discussed in Section 4.3

$$f = v_{d1}/v_{d2}. \tag{4.5}$$

Focal spot intensity profile tailoring. Two approaches to focal spot intensity profile tailoring led to two different fitness functions. The first and most simple approach was to maximize the intensity at some given pixels in the image. This differs from the peak intensity optimization since it only looks at some fixed points in the image. This method was used in order to produce two separated foci. The fitness value was in this case the smallest of the two pixel values,

$$f = \min\{\mathcal{Z}(x_1, y_1),\ \mathcal{Z}(x_2, y_2)\} \tag{4.6}$$

where (x_1, y_1) and (x_2, y_2) are the indices of the two points. A good individual is thus an individual with high pixel values at *both* pixels.

The second approach to tailoring of the focal spot intensity profile is to use a least squares fitting method to evaluate an individual. If a desired intensity profile of the focal spot is given by $\mathcal{D}$, the fitness could measure the distance between $\mathcal{D}$ and $\mathcal{Z}$. There exists many norms that measure the distance between two matrices. One is

$$f = -\sqrt{\sum_{x,y} [\mathcal{Z}(x, y) - \mathcal{D}(x, y)]^2}. \tag{4.7}$$

The fitness is the negated distance between the images in a *least squares* sense. The distance is negated since the GA, in this implementation, strives to *maximize* the fitness value. The reference profile $\mathcal{D}$ must be appropriately chosen. In this implementation, the reference profile image was read from an ordinary windows bitmap file and normalized so that its total power equaled the total power of the laser pulse.

Selection

Two selection methods were accessible from the user interface. The *roulette wheel* selection method selected parents for the next generation with a probability that was proportional to fitness,

$$p_i = \frac{f_i}{\sum f_i}. \tag{4.8}$$

The *rank-space* selection method employed a probability for selection that depended on the rank of an individual with respect to fitness *and* distance to the best individual. The distance Δ_{ij} between individuals i and j was measured as the Euclidian distance between the actuator value coordinates,

$$\Delta_{ij} = \sqrt{\sum_{k=1}^{37} (x_k^i - x_k^j)^2} \tag{4.9}$$

where x_k^i denotes the value for actuator k for individual i. The intermediate rank of individual i with respect to fitness was x_i and the rank with respect to

diversity was d_i. The *final* rank, r_i, of individual i was the rank with respect to the *sum* of the intermediate rankings,

$$s_i = r_i + d_i. \tag{4.10}$$

No dynamical control of the importance of diversity (as discussed in Section 3.2.3) was thus built into the algorithm.

Reproduction

The reproduction involved one-point crossover and mutation. The algorithm may have benefited from multiple-point crossover but that was never considered during the implementation of the code. The mutation operator simply altered the value of a binary digit with some probability for mutation. The mutation rate was accessible from the user interface so this parameter could be dynamically changed by the user and typically it was decreased as the algorithm converged.

Elitism

Since the crossover and mutation genetic operators do not conserve genetic information as was discussed in Section 3.2.6, an elitist scheme was necessary. It simply copied the best individual of the current population to the subsequent population without any involvement of the crossover or mutation operators.

4.4.3 Performance

Once the algorithm was implemented, it was first tested for peak intensity optimization. The expanded HeNe laser beam illuminated the deformable mirror. Since the deformable mirror is clamped at its edges only the central 19 actuators were illuminated (recall the results from the simulation in Section 2.4). The reflected beam was focused by a f=3000mm plano-concave lens directly on the CCD. The recorded image was sent to the control computer and analyzed by the software. By monitoring the focal spot as random actuator commands were sent to the mirror it was clear that the mirror was able to change the properties of the spot. Peak intensity was chosen as fitness and the GA was started. After some minor adjustments to the code, the algorithm was stable and similar results were obtained for consecutive runs. Figure 4.10 depicts the fitness of the best individual for each generation of a typical run. A population consisted of 20 individuals and the mutation rate was 0.005. The image acquisition was very slow. Only two images were captured every second so one generation took 10 seconds to evaluate. The optimization in Figure 4.10 took almost 30 minutes but already after 10 minutes the fitness had reached 90% of the peak value. The convergence times that were needed in the experiments, see Chapter 5, often exceeded 30 minutes. The reason was that the lens used in this initial test was well aligned. When the lens was, on purpose, misaligned, the algorithm needed more time to converge.

Laser stability

The algorithm was implemented and tested using the continuous and stable HeNe-laser. When the setup was moved and the laser source was the pulsed

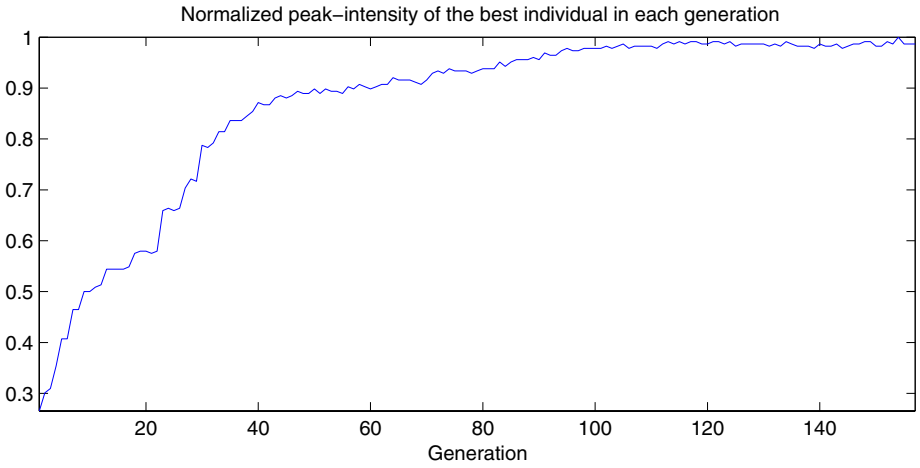

Figure 4.10: Focal spot peak intensity of the best individual for each generation. A population consisted of 20 individuals and the mutation rate was 0.005.

Ti:sapphire laser, pulse-to-pulse fluctuations posed a problem. The peak intensity of the focused Ti:sapphire pulses deviated from the average peak intensity with almost $\pm 10\%$. Since the algorithm assessed the quality of a mirror configuration through a measurement of the peak intensity, the fluctuations were expected to pose severe problems for the optimization. A number of schemes were tried in order to suppress the problems introduced by the pulse-to-pulse fluctuations.

A scheme where the fitness function measured the *width* of the focal spot instead of the *peak intensity* was tried. The problem was that the focal spot had a width of only a few pixels and width was measured in numbers of pixels. Thus, the low resolution of this scheme resulted in bad estimations of the focal spot quality.

In another approach, the fitness function averaged the fitness value over a number of acquisitions. This slowed down the optimization, which already was slow, and a maximum of 5 averaging acquisitions were acceptable from a convergence rate point of view. But an average over only 5 acquisitions did not result in a more stable signal so this approach was also abandoned.

Instead of averaging over a number of acquisitions one could increase the number of individuals in the population. As the Genetic Algorithm converged, the individuals in the population became more and more similar. When they were evaluated, the pulse-to-pulse fluctuations resulted in low fitness for some good individuals and in high fitness for some bad individuals. In a *large population*, however, many individuals will be approximately equal, and if only one individual in a group of similar, good individuals, receives a high fitness (a high-intensity pulse arrives at that, particular measurement), the qualities of this group will still have a high probability to be transferred to the next generation. This scheme was in one way an averaging scheme but it did not slow down the convergence as much. Therefore, the Genetic Algorithm employed a larger population when the laser source was the Ti:sapphire-laser than when the HeNe-laser was used.

4.4.4 Improvements

There are a number of things that could be done to improve the performance of the GA. They were not implemented mainly because of limitations in time available. First of all, multiple-point crossover should be implemented and the number of points for crossover should be accessible from the user-interface. Secondly, the elitist scheme should consider some percentage of the population as elite and not only the best individual. A larger elite population would make the algorithm less sensitive to noise. The elite percentage should be accessible from the user-interface. The probability used for the rank-space selection method should also be accessible to the user.

To speed up the algorithm convergence, it is possible to reduce the size of the chromosomes. Instead of using 37 independent variables, the actuators can be linked into groups. The Zernike polynomials describe optical aberrations and constitute an orthogonal basis on a circular geometry. To speed up the algorithm, the chromosomes may represent the amplitudes in terms of Zernike polynomials instead of actuator voltages. The voltages that must be applied to the electrodes in order to obtain the Zernike polynomial surface, $Z_n(\rho, \theta)$, are

$$\mathbf{U}_n^2 = (\mathbf{A}^T\mathbf{A})^{-1}\mathbf{A}^T\mathbf{Z}_n. \tag{4.11}$$

$\mathbf{U}_n$ is 37x1 column vector that contains the voltage on each actuator. $\mathbf{Z}_n$ is the desired Zernike polynomial, $Z_n(\rho_i, \theta_i)$, defined in the surface points (ρ_i, θ_i). It is a Mx1 vector where M is the number of surface points. The surface points define only a small part of the whole membrane since only the central 19 actuators are illuminated. This means that $\rho_i < R$ for all i, where R is the radius of the illuminated area. $\mathbf{A}$ is a 37xM matrix and the columns of $\mathbf{A}$ are the influence functions on the central part of the membrane. The derivations in Section 2.4 assumes that the mirror is linear. Since the mirror is linear only in a *biased* operation, a bias voltage, U_b, is added to the control signal. Using the 15 first Zernike polynomials, the control signal may be written as a linear combination,

$$\mathbf{U} = U_b + \sum_{n=1}^{15} a_n\mathbf{U}_n. \tag{4.12}$$

Using this relation, the chromosome of an individual is composed of fifteen coefficients, a_n. If these coefficients are coded using a 8-bit resolution, the number of different mirror configurations is $256^{15} \approx 10^{36}$ when the Zernike basis is used. Using the actuator basis, this number is $256^{37} \approx 10^{89}$. So if only the Zernike basis $\langle U_n\rangle_{n=1}^{15}$ is correctly calculated, this scheme could significantly speed up the convergence of the algorithm. A similar scheme has already been tested in order to improve the convergence of the GA [1]. When the Zernike basis was used instead of the actuator basis the convergence time decreased to one third of the original convergence time. The previously described scheme allows, however, a more precise calculation of the voltages than the calculations that were performed in [1].

Chapter 5

Experiments and results

The adaptive optics system was used to manipulate the properties of a focusing system and enhance the qualities of the focal spot. The experiments were divided in two main parts. In the first part the adaptive system strived to maximize the focal spot peak intensity while the specific shape of the focal spot was not considered. It was shown, however, that the intensity profile was close to the diffraction limit when peak intensity was maximized. This method was used to compensate for aberrations resulting from alignment errors of the focusing optics.

The second part aimed for precise control of the focal spot intensity profile. A scheme that would allow arbitrarily tailored intensity profiles was implemented and tested but turned out not to be very successful. Another scheme allowed the generation of multiple focal spots of equal intensity.

5.1 Optimization of the focal spot peak intensity

Many laser applications exploit the extreme irradiance that may be reached when a laser beam is focused to a small spot. At the Lund High Power Laser Facility, the laser system delivers ultrashort pulses with peak powers reaching 40 TW at a repetition rate of 10 Hz. The pulses are focused to achieve extreme irradiance exceeding 10^{19} W/cm^2, which allows studies of the relativistic properties of laser produced plasmas. In order to increase the peak intensity at the focal spot it is either possible to increase the pulse energy, reduce the pulse length or make the focal spot smaller. Cost and the laser bandwidth put limits to the two first alternatives and the possibility to reduce the focal spot size becomes very interesting. When a Gaussian beam is focused the focal spot diameter is

$$d = \frac{4\lambda f}{\pi D} \tag{5.1}$$

where D is the beam diameter, λ is the laser wavelength and f is the focal length of the focusing optics. In order to produce a small focal spot, the f-number, f/D, of the focusing optics should be as small as possible. At present, the focusing optics that is used for the ultra-high intensity experiments at the Lund High Power Laser Facility is a f/3 parabolic mirror. A f/1 parabola would make the spot 3 times smaller and thus increase the peak intensity with almost one order of

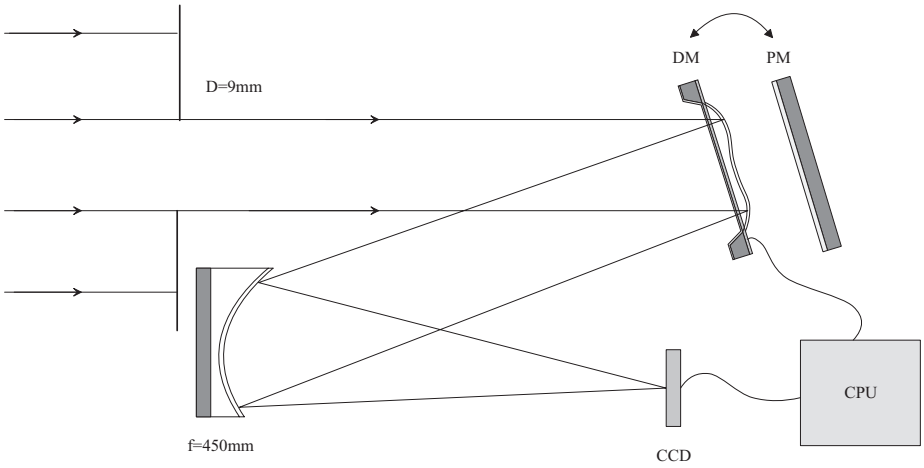

Figure 5.1: The 9mm Ti:sapphire laser beam was focused by a f=450mm parabolic mirror. The deformable mirror (DM) could be replaced by a plane mirror (PM).

magnitude. In practice, however, a f/1 parabola is very difficult to manufacture with "perfect" shape and also very difficult to align so aberrations, mainly astigmatism, are introduced by the focusing optics [2] [1]. These aberrations degrade the focusing power of the system (see Section 2.1.3) so the focal spot never reaches the diffraction limit and the peak intensity does not increase as much as could be expected.

The aim for the experiments described below was to prove that an adaptive optics system could be used to precompensate for the astigmatism introduced by misaligned focusing optics.

5.1.1 Compensating focusing optics alignment errors

The experimental setup is depicted in Figure 5.1. The laser system that was used for this experiment was the Ti:sapphire laser. Since the deformable mirror (DM) is clamped, its motion is restricted near the edges. In order to allow arbitrary deformations near the aperture edge, only the central 19 actuators were illuminated. The actuator center-to-center distance is 1.8 mm so the laser beam diameter was adjusted by a variable aperture to 9 mm. The original beam diameter was 50 mm and its intensity profile was approximately Gaussian. The aperture selected only a central disc of the original beam so the intensity profile at the aperture was approximately a top-hat, that is the intensity was uniform throughout the aperture and zero outside.

The attenuated 9mm beam illuminated the DM under a small inclining angle in order to preserve circular symmetry. The reflected beam was then focused by a parabolic mirror on to the CCD-chip. The focal length of the parabola was 450 mm so the f-number was very large,

$$f/\# = 50$$

The discussion above addressed the alignment problems associated with a low f/# parabola so using a f/50 parabola for the experiments might seem inappropriate. However, with this parabola, the setup was simplified since there was no

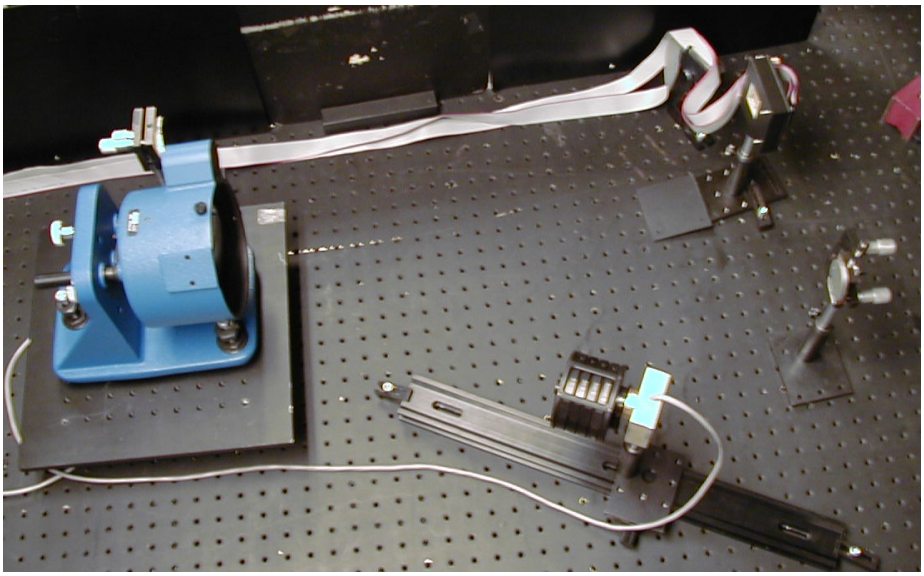

Figure 5.2: The deformable mirror, the plane mirror, the focusing parabolic mirror and the CCD-camera with mounted attenuators.

need to magnify the focal spot on to the CCD. Instead the parabola could focus the beam right on to the chip since the spot diameter was significantly bigger than each pixel. When a circular beam with uniform intensity and no wavefront distortions is focused, the resulting focal intensity distribution is given by an Airy pattern [16]. The central Airy disc has the diameter

$$d = 2 \cdot 1.22 \cdot \frac{\lambda f}{D}. \tag{5.2}$$

With our parameters, this gives a spot diameter of 98 μm, while the size of each pixel on the CCD chip used is approximately 6 μm, so the shape of the focal spot could be well resolved on the chip.

When voltages were applied to the actuators, the membrane was attracted towards them. The shape of the membrane was shown in Section 2.4 to be parabolic,

$$u(r) = \frac{\zeta V_0^2}{4} \left(r^2 - R^2\right). \tag{5.3}$$

The maximum deflection of the membrane was 5.4 μm and its diameter 15 mm. Thus, the membrane had a radius of curvature of 5.2 m when it was fully deflected. The DM could therefore, depending on the actuator voltages, act as f= 2.6m-∞ variable concave mirror. It is possible to compensate for this by letting the inclining beam be slightly divergent but in the current setup that was no alternative. Instead, the parabola was aligned with the mirror membrane deflected to half its maximum. As was shown in Section 2.4, the membrane deflection depended on the *squared* actuator voltages. In order to deflect the membrane to half its maximum, the command

$$c = \frac{227}{\sqrt{2}} \simeq 160$$

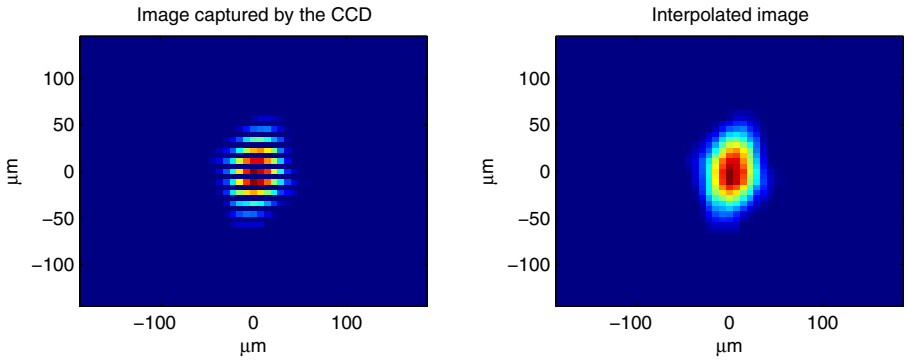

Figure 5.3: The short pulses of the Ti:sapphire laser could not be fully registered by the CCD-camera so the captured images had to be interpolated. The interpolation was linear.

was sent to all actuators. Recall that the membrane reached its maximum deflection when the actuator command 227 was sent to all actuators.

Because of the angle of incidence and the curvature of the mirror, the deformable mirror itself induced some astigmatism at this stage. It was presumed that the mirror could compensate for this intrinsic astigmatism.

When the parabola was aligned, the CCD-camera was positioned in the focal plane. Due to the curvature of the mirror, the distance between the parabola and the focal plane was slightly changed to (see Appendix B)

$$F = \frac{R/2 - L}{f + R/2 - L} \cdot f = 406mm \tag{5.4}$$

where f=450 mm was the focal length of the parabola and R=10.4 m was the radius of curvature of the half deflected deformable mirror and L=1.0m was the distance between the deformable mirror and the parabola. The focal plane was thus shifted 44 mm towards the parabola when the deformable mirror was deflected to half its maximum.

The image acquisition was synchronized with the 10 Hz repetition rate of the laser using a delay unit with a variable delay. The CCD-camera captures an image in two steps. First, it takes the pixel values for row number 1, 3, 5, etc. and sends the information to the frame grabber in the control computer. Then it sends the pixel values in row number 2, 4, 6, etc. to the computer. Since the Ti:sapphire laser pulses were very short, the frame grabber only had the time to register every second row of the image. This had to compensated for and the images were interpolated before analysis. Figure 5.3 displays the raw, and linearly interpolated images of the focal spot.

The driver units maximum voltage was set to 275 V, so the maximum actuator voltages were 255 V, according to the amplifier board specifications. The GA employed the roulette wheel selection method, a population consisted of 50 individuals and the mutation rate was initially set to 0.01. As the algorithm converged, the mutation rate was diminished and at the end of the experiment it was 0.0005. The focal spot peak intensity was chosen as the fitness function. The optimization took three hours.

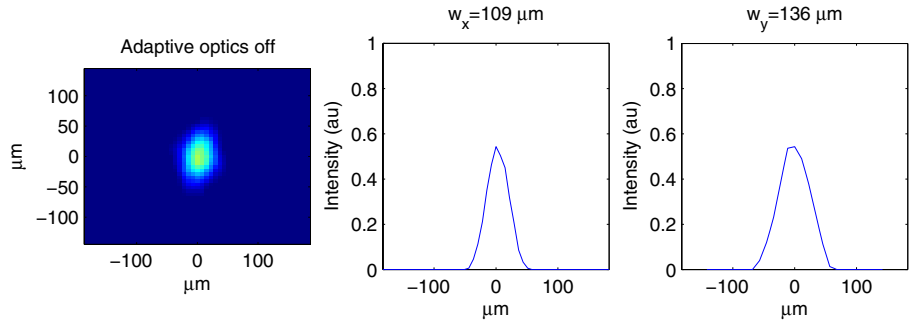

Figure 5.4: Focusing with a parabolic mirror. The deformable mirror was *not* used for aberration compensation.

The deformable mirror was replaced by an ordinary plane mirror and the parabola was realigned. A translator was used to slide the camera through the focus as the software in the control computer registered the peak intensity. Figure 5.4 displays the focal spot when no adaptive optics was used but at the point were the peak intensity reached its maximum. The width of the spot was measured as the distance between the first minima on each side of the central disc. This spot was 109 μm in the horizontal direction and 136 μm in the vertical direction. Compared to the diffraction limit (98 μm) the spot was 1.1 and 1.4 times the diffraction limit in each direction.

Figure 5.5 shows the results obtained with the adaptive optics system. The spot is 0.8 and 1.3 times the diffraction limit respectively. The adaptive optics system increased the peak intensity by 85%. It might seem strange that the spot size was below the diffraction limit in the horizontal direction. The reason for this was that the laser intensity profile was assumed to be a top-hat before it was focused. The focal spot intensity profile is in that case described by the square of a *Bessel function of the first kind*, $J_1(\gamma)$ [16]. The Bessel function may be expressed as an infinite series,

$$J_1(\gamma) = \frac{\gamma}{2} - \frac{(\gamma/2)^3}{1^2 \cdot 2} + \frac{(\gamma/2)^5}{1^2 \cdot 2^2 \cdot 3} - ... \tag{5.5}$$

The intensity at the focal spot is then

$$I(\gamma) = I_0 \left(\frac{2J_1(\gamma)}{\gamma} \right)^2 . \tag{5.6}$$

The dimension-less parameter γ is

$$\gamma = \frac{\pi D r}{\lambda f} \tag{5.7}$$

where D is the aperture diameter, f is the focal length and r is the radial coordinate in the focal plane. The intensity distribution, given by equation 5.6 is plotted in Figure 5.6. The central maximum contains almost all the pulse energy and is called the *Airy disc*. Outside the Airy disc there are other maxima but these are not seen in figures 5.4 and 5.5. The reason is that the intensities of these small maxima were smaller than the noise. When the background was

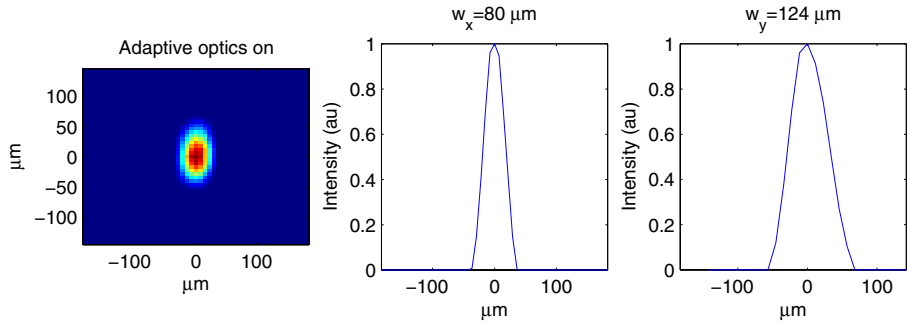

Figure 5.5: Focusing with a parabolic mirror. The deformable mirror was used for aberration compensation and the Genetic Algorithm optimized peak intensity.

subtracted, the diffraction rings disappeared. Experimentally the diameter of the Airy disc was measured as the distance between the first minima outside the central disc. Figure 5.6 illustrates in which diameter this method results if the background magnitude was exactly equal to the intensity of the first maxima on either side of the Airy disc. When this background is subtracted, the measured diameter will be

$$d_{meas} = 84\mu m$$

The diffraction limit was 98 μm so, in fact the diameter of a *diffraction limited* focal spot will be observed as

$$\frac{d_{meas}}{d_{diff}} = 0.86 \tag{5.8}$$

times the diffraction limit. If the noise is higher, this ratio will be even smaller. This explains why observed spot diameter was under the diffraction limit.

A far more unpleasant problem was the elliptic shape of the focal spot. Ideally the focal spot would be circular, with a diffraction-limited diameter. The experiment was run several times but with the same result, the spot was 60% longer in the vertical direction than in the horizontal direction. It was suggested that some asymmetry in the CCD-camera in conjunction with the ,ultrafast pulses of the Ti:sapphire laser could be the source of the problem but, as the camera was rotated, the asymmetry of the focal spot did not change. It was suggested that the deformable mirror *itself* was asymmetric and that the strains in the membrane were different in the different directions. But, as the deformable mirror was rotated, the focal spot remained asymmetric in the same direction.

Only the Ti:sapphire laser beam remained. It was proposed that the beam was astigmatic, but the adaptive system had already corrected much heavier astigmatism (see Section 5.1.2). Finally it was suggested that the asymmetry was the result of *chromatic* aberrations. If the different wavelengths of the broad spectra of the femtosecond pulses had slightly different direction, the focal spot would be elongated in the direction of the dispersion. The mirror could not, however, change the direction of all wavelengths independently so it would not be possible to correct for angular dispersion with the deformable mirror in the current setup. Angular dispersion can be the result of misaligned gratings in the

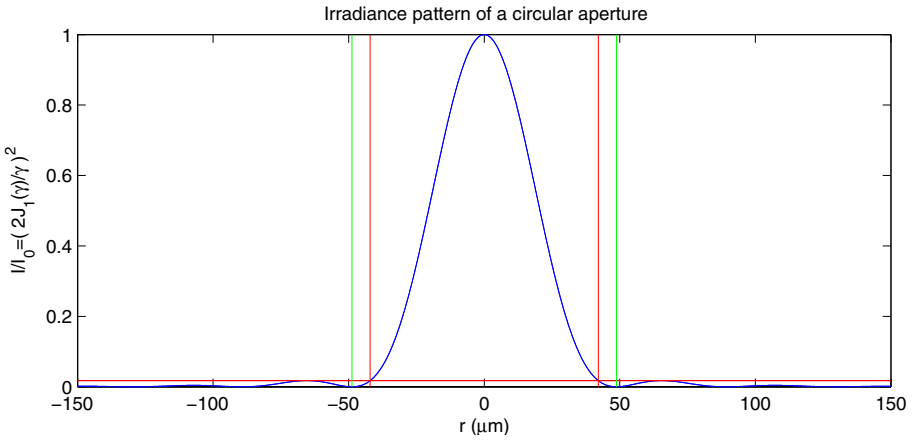

Figure 5.6: Diffraction limited focal Airy pattern of the Ti:sapphire laser. The horizontal line illustrates a hypothetical background level. The distance between the outer vertical lines is the diffraction limited diameter of the focal spot. The distance between the inner vertical lines is the diameter that would be observed when the background has been subtracted.

compressor but the experiment was never repeated with uncompressed pulses so it was never proved that the compressor was the source of the aberrations.

Nevertheless, the adaptive optics system increased the peak intensity by 85%.

5.1.2 Off-axis focusing with a spherical mirror

When working with ultrafast lasers it is often necessary to use *reflective* optics. Short, high-power laser pulses contain many wavelengths and *refractive* optics cause dispersion and nonlinear effects that degrade the beam quality. An *off-axis* focusing mirror makes it possible to focus the beam by using only reflective optics. An off-axis *parabolic* mirror is generally used to focus the beam at the end of ultra-intense laser chains such as the High Power Ti:sapphire laser at the Atomic Physics Department. A parabolic mirror, such as the one used in Section 5.1.1, is off-axis by nature and enables diffraction limited focal spots if it is only appropriately aligned and correctly manufactured. The production of parabolic surfaces is however quite demanding compared to the techniques employed to obtain spherical surfaces. Thus spherical mirrors are cheaper and allow shorter focal lengths than parabolic mirrors. Unfortunately, a spherical mirror induces aberrations, mainly astigmatism and coma, when it is used for off-axis focusing.

The idea behind the experiments, described in this section, was to replace the parabolic mirror by a spherical mirror and correct the induced aberrations with the deformable mirror and the genetic algorithm. The experimental setup is depicted in Figure 5.1.2. The experiment was first performed using the expanded Gaussian HeNe laser beam. The setup was then moved and the experiment was repeated using the top-hat Ti:sapphire femtosecond laser pulses.

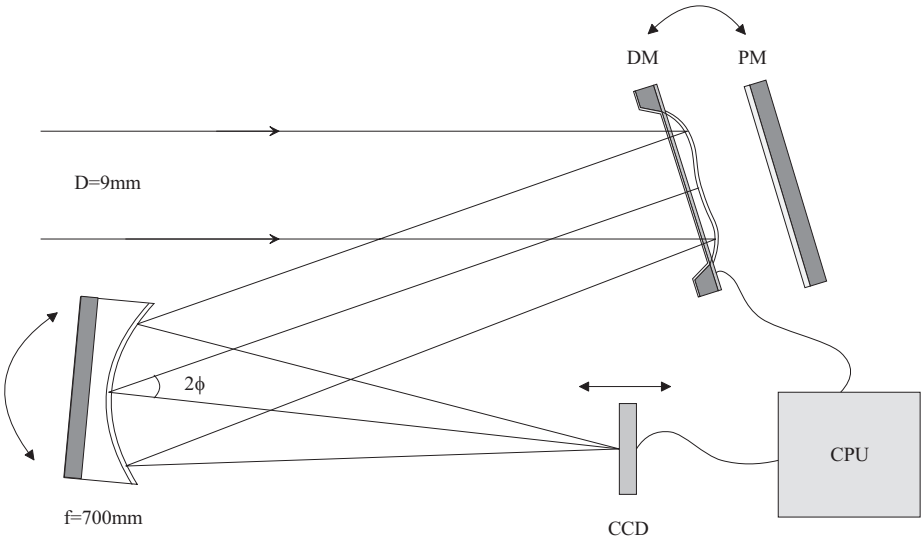

Figure 5.7: A spherical mirror was used to focus the laser. The mirror could be turned so that the incident angle was changed. The deformable mirror could be replaced by a plane mirror so that the reflected beams coincided, preserving the incident angle on the spherical mirror.

The HeNe-laser

The diameter of the expanded *Gaussian* HeNe laser beam was 9mm so that only the 19 central actuators were illuminated. The beam was reflected by the deformable mirror in a small angle in order to preserve circular symmetry of the illuminated area on the mirror. The beam was then focused by a spherical mirror with a focal length of 700mm so the f-number of the focusing optics was again very high,

$$f/\# = 78.$$

The beam was focused on to the CCD and an image of the focal spot was captured and sent to the control computer. The CCD was placed in the focal plane when the membrane was deflected to half its maximum. The curvature of the deformable mirror moved the focal plane 100mm towards the spherical mirror.

The deformable mirror could be replaced by a plane mirror so that the reflected beam coincided with the beam that was reflected from the deformable mirror. The idea was to use the plane mirror as a reference of what happened if no adaptive optics was used to compensate for the astigmatism and coma. The amount of aberrations that was induced by the off-axis focusing spherical mirror was quite dependent on the angle of incidence so, as the incidence angle increased, the focal spot peak intensity diminished.

The genetic algorithm employed a population of 20 individuals and the mutation rate was 0.005. Fitness was measured as the peak intensity and the rank-space selection method was used. The algorithm optimized the peak intensity for several angles of incidence, ranging from 5^o to 17^o. As the angle was

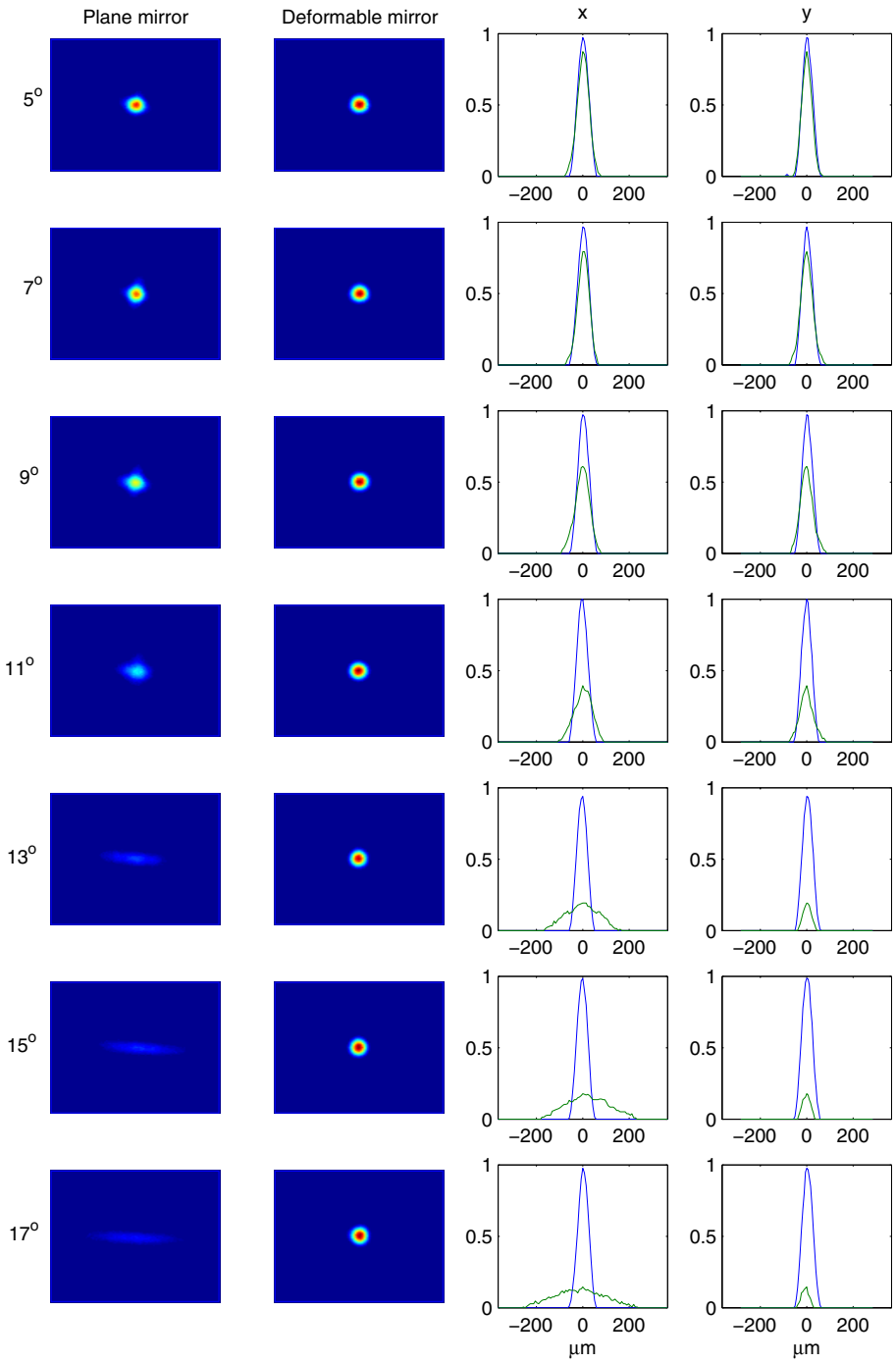

Figure 5.8: Focal spot intensity profiles for incident angles 5^o, 7^o, 9^o, 11^o, 13^o, 15^o and 17^o. Left column shows plane mirror results and the adjacent column the results obtained with the adaptive optics system. The diagrams display the intensity in the horizontal and longitudinal directions.

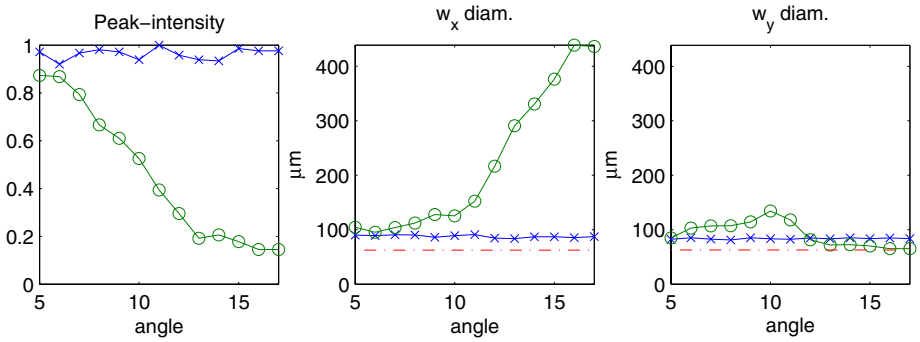

Figure 5.9: Peak intensity and $1/e^2$ spot diameter of the focused HeNe-laser beam for several angles of incidence. The results obtained with the deformable mirror are x-marked and the results for the plane mirror are marked with circles. The diffraction limit is dot-lined.

x	5^o	7^o	9^o	11^o	13^o	15^o	17^o
PM	103	100	128	150	280	363	410
DM	83	87	86	83	84	78	84
PM	1.65	1.59	2.00	2.39	4.47	5.79	6.54
DM	1.32	1.38	1.37	1.33	1.33	1.24	1.35

Table 5.1: Focal spot $1/e^2$ diameter (horizontal direction) of the focused HeNe-laser beam in μm and compared to the diffraction limit.

increased, the astigmatism introduced by the focusing mirror became more and more significant.

For every angle, a plane mirror replaced the deformable mirror after optimization. A translator was used to slide the CCD through focus as the computer software monitored the peak intensity. The focal spot intensity profile was captured when the CCD was positioned at the point that corresponded to maximum peak intensity.

The results are summarized in Figure 5.8. It was clear that the adaptive optics system was capable to compensate quite heavy astigmatism. As the spherical mirror was turned to larger and larger angles, the astigmatism became more and more severe and the peak intensity was significantly decreased at an angle of incidence of 17^o. The adaptive optics system, however, was able to compensate for the induced aberrations and the peak intensity never decreased. In order to compare the peak intensity of two focal spots, the gain of the camera had to be constant. Angles larger than 17^o resulted in a very weak signal from the plane mirror while the signal from the deformable mirror almost saturated the CCD. Thus angles larger than 17^o were not treated and the limitations of the deformable mirror were not reached as is illustrated in Figure 5.8 and 5.9.

The HeNe laser beam was Gaussian so the diffraction limit for the diameter of the focal spot was

$$d = \frac{4\lambda f}{\pi D} = 63\mu m. \tag{5.9}$$

Gaussian curves, $f(x) = y_0 + Ae^{-(x-x_0)^2/w^2}$, were fitted to the line-outs in

Figure 5.8. For data points (x_i, y_i), the centroid, amplitude and base intensity was calculated as

$$x_0 = \frac{\sum x_i y_i}{\sum y_i}\,,\ A = \max_i(y_i)\,,\ y_0 = \min_i(y_i) \tag{5.10}$$

The width of the focal spot, w, was calculated through a least-squares approximation.

$$\frac{1}{w^2} = (\mathbf{M^T M})^{-1}\mathbf{M^T u} \tag{5.11}$$

where $\mathbf{M}$ and $\mathbf{u}$ are column vectors and

$$\begin{aligned} \mathbf{M} = &\quad [x_1^2\ x_2^2 \ldots x_N^2]^T, \\ \mathbf{u} = &\quad \left[\ln\tfrac{y_1-y_0}{A}\ \ln\tfrac{y_2-y_0}{A} \ldots \ln\tfrac{y_N-y_0}{A}\right]^T. \end{aligned} \tag{5.12}$$

The $1/e^2$ diameter of the Gaussian focal spot was then calculated as

$$d = 2w\sqrt{2} \tag{5.13}$$

The result is depicted in Figure 5.9. The first diagram shows how peak intensity decreases with increasing incident angle. The adaptive optics system was able to keep the peak intensity almost constant for all angles. The next two diagrams display the $1/e^2$ spot diameters in the horizontal and longitudinal directions for different angles. The spot diameters resulting from off-axis focusing by the spherical mirror *without* aberration compensation is marked with circles. The spot diameters obtained using the deformable mirror are marked with an x. The diffraction limit is marked as a dotted line. The astigmatism that was induced by the spherical mirror increases the spot diameter in the horizontal direction. For 17^o the spot diameter was 410 μm which is 6.5 times the diffraction limit. The deformable mirror was able to keep the spot diameter at a constant magnitude between 1.2 and 1.4 times the diffraction limit for all angles. For 17^o, the spot diameter was 1.3 times the diffraction limit. Table 5.1 displays the spot diameters in the horizontal direction, in μm and in terms of the diffraction limit.

The Ti:sapphire-laser

The same experiment was performed, using the top-hat Ti:sapphire laser beam. The image acquisition system was synced to the 10Hz repetition rate of the laser. The negative effect of the pulse-to-pulse fluctuations were minimized by using a larger population of individuals for the optimization. This slowed the convergence of the algorithm but increased its performance. The diameter of the beam was again 9mm so the diameter of the diffraction limited central Airy disc was

$$d = 2.44 \cdot \frac{f\lambda}{D} = 152\mu m \tag{5.14}$$

The results for angles 2.5^o, 5^o, 7.5^o, 10^o, 12.5^o and 20^o are shown in figures 5.10 and 5.11. The spot diameter was measured as the distance between the first minima on each side of the central disc. Without compensating adaptive optics, peak intensity was significantly reduced by the astigmatism that was induced by the off-axis spherical mirror.

The deformable mirror was able to compensate for the aberrations that was introduced by the focusing optics but peak intensity drops for angles 12.5^o and

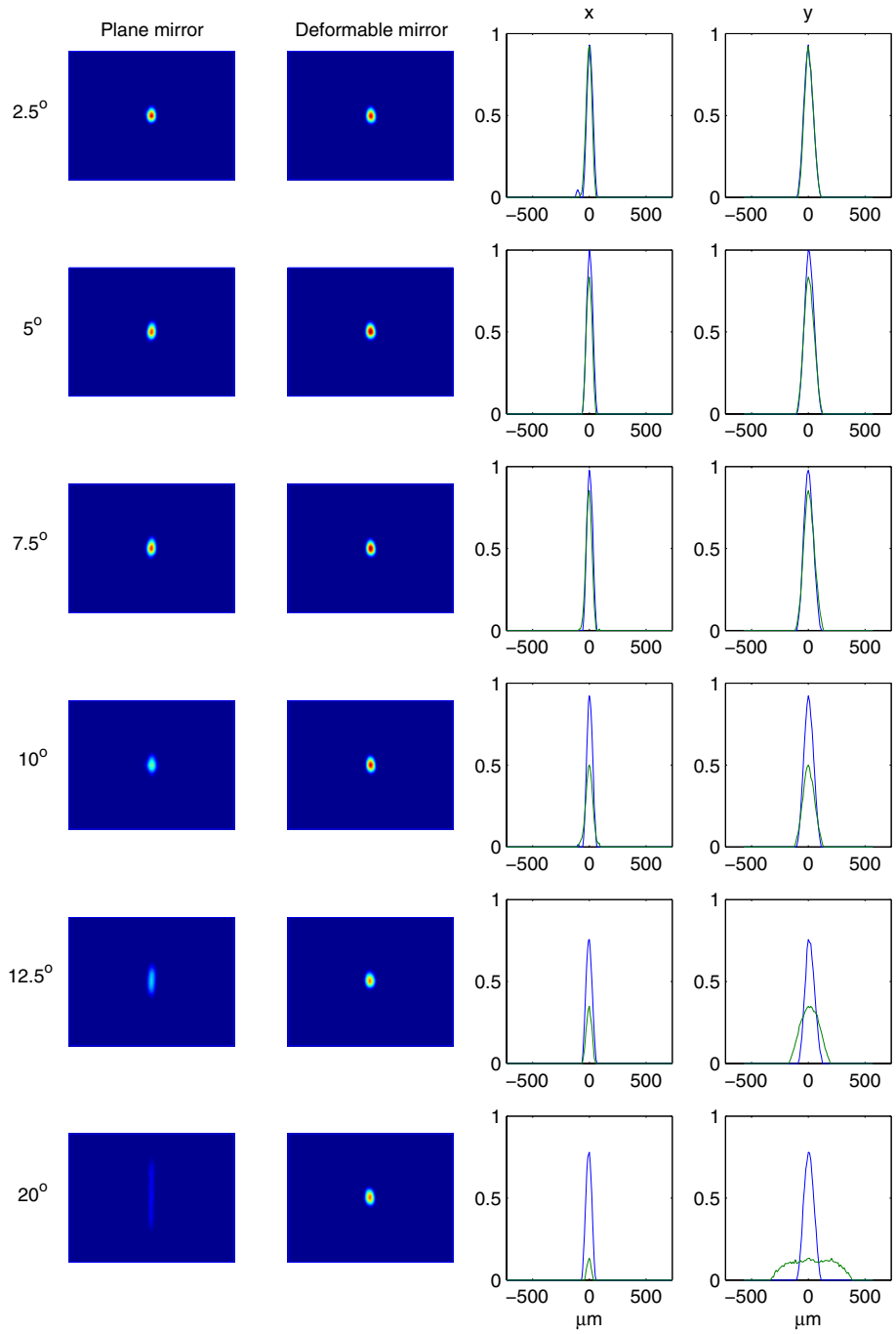

Figure 5.10: The focused Ti:sapphire laser. Focal spot intensity profiles for incident angles 2.5^o, 5^o, 7.5^o, 10^o, 12.5^o and 20^o. Left column shows plane mirror results and the adjacent column the results obtained with the adaptive optics system. The diagrams display the intensity in the horizontal and longitudinal directions.

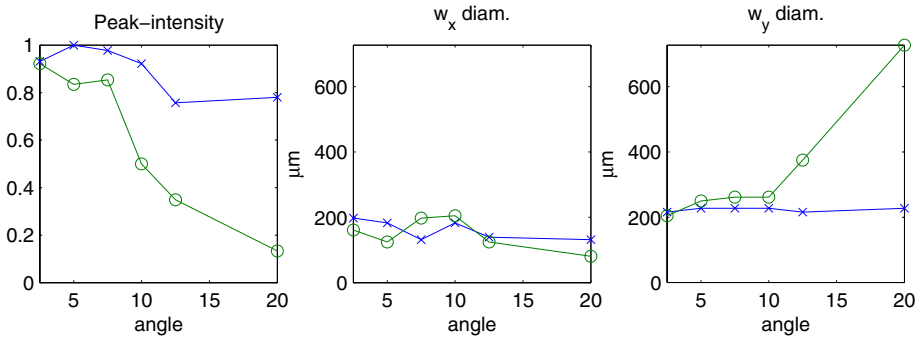

Figure 5.11: Peak intensity and diameter of the focused Ti:sapphire laser for several angles of incidence. The results obtained with the deformable mirror are x-marked and the results for the plane mirror are marked with circles.

20^o. Looking at the results obtained with the continuous HeNe-laser beam this deterioration seems unmotivated. The intensity drop could have been the result of a drift of the pulse energy in the Ti:sapphire laser chain or maybe the algorithm simply would have needed more time to converge. In order to compare the intensities, it was necessary to do all measurements during one day so that the laser was not shut down between the measurements. The GA needed in general several hours to converge so perhaps a higher peak intensity could have been obtained for these angles if the algorithm had been given more time.

Conclusions

The deformable mirror and the Genetic Algorithm were used to compensate for aberrations, mainly astigmatism, induced by off-axis focusing with a spherical mirror. The results were good and showed that a high f-number of the spherical mirror could be used for off-axis focusing if a deformable mirror is used to eliminate the induced aberrations. In a real situation, it is however often desirable to use a low f-number of the focusing optics in order to reach high intensities in the focal spot. This situation has been investigated [17], the main difference from the present work being that a wave-front sensor was used in order to allow corrections in only one iteration.

5.1.3 Simplified detection

A scheme that would optimize the focal spot peak intensity using a simplified method for detection was also tested. The HeNe-laser beam was expanded and a 8 mm aperture selected the central part of the beam so the beam profile was top-hat. A beam-splitter was placed in front of the deformable mirror (see Figure 5.12). The transmitted beam was reflected by the deformable mirror and focused by a f=40 mm plano-convex lens. A microscope objective magnified the focal spot and a variable aperture selected the central part of the spot image. A diode registered the power of the transmitted light and the measured voltage was sent from an oscilloscope to the control computer. Another diode measured a signal, proportional to the total power of the beam and the signal that was

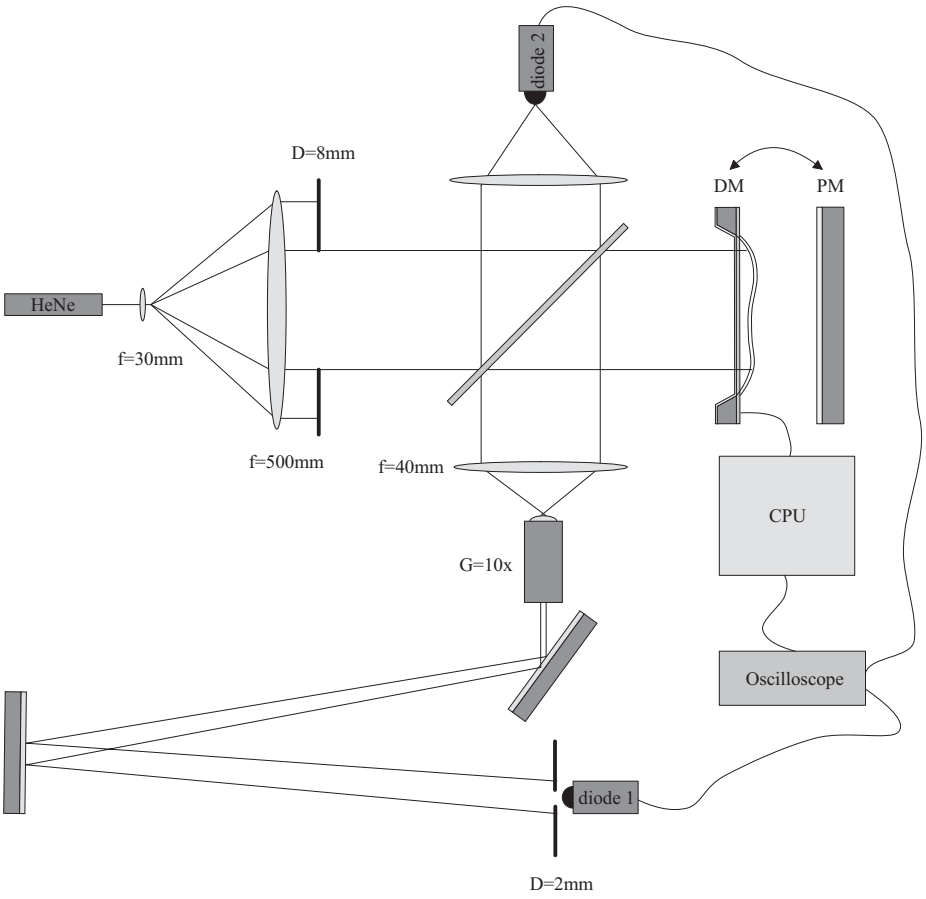

Figure 5.12: Optical setup in order to optimize the focal spot peak intensity by measuring the power in the bucket. The size of the bucket is determined by the diameter of the variable aperture in front of the diode.

optimized by the genetic algorithm was

$$f = v_1/v_2 \tag{5.15}$$

where v_1 was the voltage of the diode that measured the spot peak power and v_2 was the voltage of the diode that measured the total power of the beam. The distance between the objective and the variable aperture was 5 m and the focal length of the objective was 16 mm. The focal spot was thus magnified 310 times.

$$\frac{1}{a} + \frac{1}{b} = \frac{1}{f} \Rightarrow M = \left|\frac{b}{a}\right| = \frac{b-f}{f} \simeq \frac{b}{f} = \frac{5000}{16} = 310 \tag{5.16}$$

The beam profile was a 8 mm in diameter top-hat so the size of the central Airy disc was

$$d = 2.44\,\frac{\lambda f}{D} = 7.7\mu m \tag{5.17}$$

The *magnified* Airy-disc was 2.4 mm in diameter. The variable aperture was adjusted to match the size of the Airy-disc. The algorithm employed a population of 20 individuals and the roulette wheel selection method was used. The

mutation rate was 0.05. When the deformable mirror had been optimized, the fitness signal was

$$f_{DM} = 2.1 \tag{5.18}$$

A plane mirror was inserted in front of the deformable mirror. The microscope objective was translated through the focus and the steering mirror behind the objective was adjusted in order to obtain the highest possible fitness signal from the diodes. The maximal fitness signal found was

$$f_{PM} = 1.1 \tag{5.19}$$

The peak power had increased by almost a factor of 2. This was quite remarkable since the 40 mm focusing lens had been carefully aligned and the HeNe-laser beam was expected to be free of aberrations. The optics used in the setup was however *not* free of aberrations. The magnified focal spot suffered from coma when the plane mirror was inserted in front of the deformable mirror, but the optimized focal spot was free of coma. Sources of coma could have been either the focusing lens itself or the lenses in the beam-expanding telescope. Another explanation to the peak intensity augmentation was the beam steering capabilities of the deformable mirror. As random actuator command values were continuously sent to the deformable mirror, the position and the shape of the focal spot changed a lot. During optimization it was possible for the algorithm to accurately tune the position of the focal spot in order to exactly match the position of the variable aperture. When the plane mirror was used, these adjustments were made manually.

The main drawbacks of this detection technique were probably the speed and the resolution. The optimization that has just been described took many hours to complete. Such conditions make for instance software-debugging a *very* time-consuming activity. The convergence time depended completely on the acquisition rate. Two oscilloscope measurements were sent to the computer every second. This means that only one individual was evaluated every second since two diodes were used. The mirror is able to operate in the kHz regime and the CPU time needed for every generation was in the ms regime so in principle the optimization could have been completed in a few minutes instead of hours. The spatial resolution of the diode measurement was worse than that of the CCD since the CCD peak intensity measurement resolved individual pixels. When the CCD was used for peak intensity measurements, the problems associated with beam steering were eliminated.

5.2 Tailoring the focal spot intensity profile

So far, *peak intensity* has been the main quality of interest of the focal spot. In many high-power laser applications the peak intensity is indeed an important quality but the *shape* of the focal spot intensity profile may also be of interest. Two schemes for tailoring of the focal spot intensity profile have been investigated. The first scheme was quite similar to the peak intensity optimization and was used to produce two focal spots of equal intensity. The other scheme was designed to allow custom focal spots. The results of the latter were not satisfying and the method would benefit from a deeper investigation of the phase-modulating capabilities of the deformable mirror as well as the magnitude of noise in the CCD-camera.

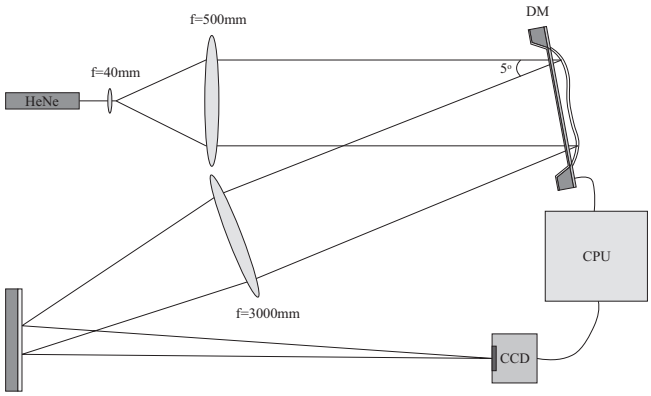

Figure 5.13: Optical setup for focal spot intensity profile tailoring.

5.2.1 Two foci

The optical setup is depicted in Figure 5.13. The expanded 9mm HeNe-laser beam illuminated the deformable mirror and the reflected beam was focused with a f=3000mm plano-convex lens. The CCD-camera was positioned in the focal plane when the membrane was deflected to half its maximum. Two pixels, (x_1, y_1) and (x_2, y_2), in the image, $\mathcal{Z}$, were chosen and the fitness function returned the smallest value of these pixel,

$$f = \min(\mathcal{Z}(x_1, y_1), \mathcal{Z}(x_2, y_2)). \tag{5.20}$$

The idea was that this fitness function would lead to a simultaneous optimization of both pixel intensities, producing two hot-spots of equal intensities. The result is shown in Figure 5.14. The size of the population was 20 individuals, the mutation rate was 0.005 and the roulette-wheel selection method was employed for the optimization. Line-outs of the hot-spots are shown in Figure 5.14 together with Gaussian fits to the peaks. The peak intensities of the hot-spots differed only by 6% which was good since the main goal for the optimization was to produce two spots of equal intensity. The $(1/e^2)$ diameters of the spots were

	w_x	w_y	I_{peak}
Spot 1	$445\mu m$	$503\mu m$	0.94
Spot 2	$444\mu m$	$463\mu m$	1.00

The characteristics of the generated hot-spots were thus comparable which could be of importance for applications. The diffraction limited spot diameter of the 9mm Gaussian HeNe-laser beam was

$$d = \frac{4\lambda f}{\pi D} = 269\mu m \tag{5.21}$$

so both spots were 1.65 times the diffraction limit in the direction of separation and 1.7 and 1.9 times the diffraction limit in the other direction.

The spots were separated on the CCD by $525\mu m$. The normalized intensity was 0.28 between the peaks so the visibility was not very good. The visibility

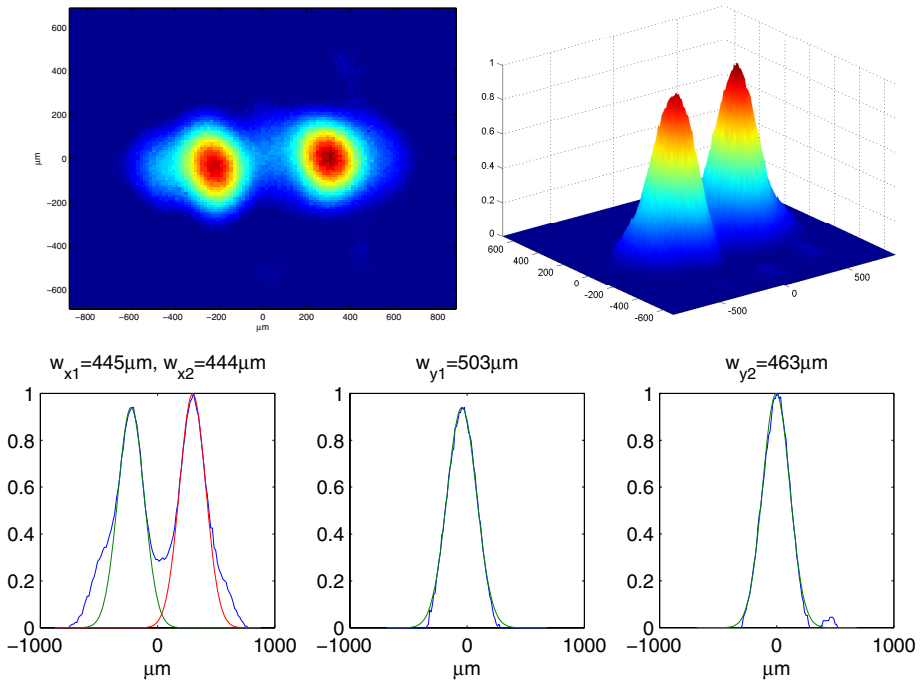

Figure 5.14: Two focal hot-spots.

of the spots was

$$V = \frac{I_{max} - I_{min}}{I_{max} + I_{min}} = 0.56 \tag{5.22}$$

In an attempt to increase the visibility of the spots another optimization was done, using a slightly different fitness function.

$$f = V \cdot \min(\mathcal{Z}(x_1, y_1), \mathcal{Z}(x_2, y_2)) \tag{5.23}$$

where V was the visibility.

$$V = \frac{\min(\mathcal{Z}(x_1, y_1), \mathcal{Z}(x_2, y_2)) - \mathcal{Z}(x_3, y_3)}{\min(\mathcal{Z}(x_1, y_1), \mathcal{Z}(x_2, y_2)) + \mathcal{Z}(x_3, y_3)} \tag{5.24}$$

where (x_3, y_3) were the coordinates for a pixel, mid-way between the hot-spot pixels. The idea behind this fitness function was that it would yield high fitness for individuals that produced two hot-spots of equal peak intensity *and* with a good contrast. The result from an optimization of the fitness function in equation 5.23 is shown in Figure 5.15. The intensity at (x_3, y_3) between the spots was 0.08 so the contrast was indeed increased which was a main goal for the optimization. The optimized visibility was

$$V = \frac{I_{max} - I_{min}}{I_{max} + I_{min}} = 0.93. \tag{5.25}$$

The intensities of the spots differed by 8% and the spot $(1/e^2)$ diameters were similar in the different directions.

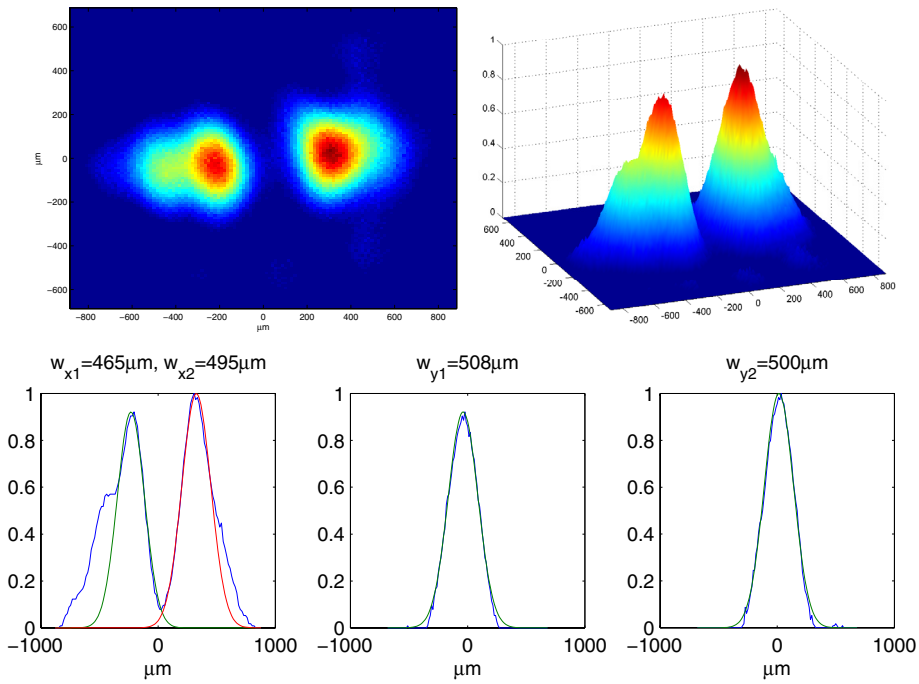

Figure 5.15: Two focal hot-spots, visibility optimized.

	w_x	w_y	I_{peak}
Spot 1	$465\mu m$	$508\mu m$	0.92
Spot 2	$495\mu m$	$500\mu m$	1.00

The shapes of the spots in Figure 5.15 were not very nice and in particular the left spot (spot number 1) had a quite nasty bump on its back. The reason was simply that the algorithm only considered three points in the image and the *shapes* of the spots were ignored. A fitness function that took the shape of the focal spot into account was also tested and the results are given in Section 5.2.2.

Application

One possible high-power application of two closely spaced focal spots of equal intensity is the simultaneous triggering of two closely spaced plasma channels in a gas-jet. In this test the spots were separated by approximately $500\mu m$ which was two times the size of the diffraction limited focal spot. Focusing optics with a focal length of 150mm would, for the high-power Ti:sapphire laser ($\lambda = 800nm, D = 50mm$), allow the spots to be separated by only $6\mu m$. For such small spots it would be necessary to use magnifying optics in order to image the focal spot on the CCD. The difference in intensity between the spots was only 8% of the peak intensity, so perhaps it would be possible to create two channels with approximately equal prerequisites (peak intensities and spot sizes) at exactly the same time.

5.2.2 Top-hat focal spot intensity profile

A fitness function that judges the *shape* of the focal spot needs some reference. In the software that was developed and used, the reference was an ordinary Windows bitmap image. The image was read by the software and normalized so that the total power of the reference intensity profile equaled the power of the laser spot. This meant that

$$\int_{\mathcal{S}} \mathcal{Z}(x,y)dxdy = \int_{\mathcal{S}} \mathcal{D}(x,y)dxdy \tag{5.26}$$

where $\mathcal{Z}$ was the spot intensity profile and $\mathcal{D}$ was the reference image. The integration was performed over the entire image. Fitness was measured as the distance between the reference spot and the current focal spot. There are many norms that measure the distance between two matrices. The fitness function was the negated Euclidian distance,

$$f = -\sqrt{\sum_{x,y} \left[\mathcal{Z}(x,y) - \mathcal{D}(x,y)\right]^2}. \tag{5.27}$$

The distance was negated since the Genetic Algorithm strived to maximize the fitness function, which in this case meant minimizing the distance.

The optical setup was identical to the setup in Section 5.2.1 (see Figure 5.13) and the only thing that was changed was the fitness function in the algorithm. The shape that was chosen for the tests was a circular top-hat. The reference intensity profile and the results from the optimization are shown in Figure 5.16. It was clear that the optimization failed its main goal, to produce a top-hat focal spot. But, some things were however promising. First, it was clear that the algorithm had found the position of the reference image. When the optimization started, the focal spot jumped to different positions in the image but converged to the *position* were the reference top-hat was situated. Next, the intensity profile of the optimized spot was flatter than the ordinary Gaussian shape that would be the result if a Gaussian beam is focused by well aligned optics. In order to somehow measure the flatness of the spot, super-Gaussians of various order were fitted to the intensity profile in the x-direction. These are shown in one of the plots in Figure 5.16. A super-Gaussian function is a generalized Gaussian function. A super-Gaussian of order n is given by

$$g_n(x) = y_0 + Ae^{-\left(\frac{x-x_0}{w}\right)^{2n}} \tag{5.28}$$

For high n, the super-Gaussian is flatter than an ordinary Gaussian and in the limit, when $n \to \infty$, it approaches a top-hat. The super-Gaussians that were fitted to the data in Figure 5.16 were of the first, second and third order. For data points (x_i, y_i), the centroid, amplitude and base intensity were calculated as in Section 5.1.2. The width of the spot, w, was then calculated through a least-squares approximation, but now the order, n, of the super-Gaussian had to be taken into account.

$$\frac{1}{w^{2n}} = (\mathbf{M^T M})^{-1}\mathbf{M^T u} \tag{5.29}$$

where $\mathbf{M}$ and $\mathbf{u}$ are column vectors.

$$\begin{aligned} \mathbf{M} &= \left[x_1^{2n}\ x_2^{2n}\ ...\ x_N^{2n}\right]^T \\ \mathbf{u} &= \left[\ln\tfrac{y_1-y_0}{A}\ \ln\tfrac{y_2-y_0}{A}\ ...\ \ln\tfrac{y_N-y_0}{A}\right]^T \end{aligned} \tag{5.30}$$

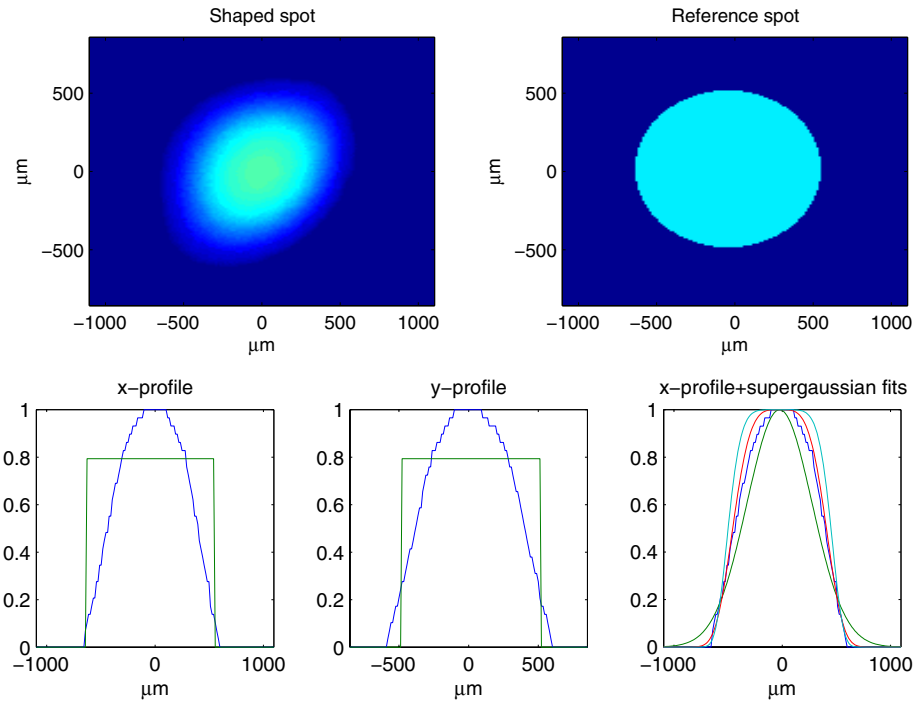

Figure 5.16: Focal spot intensity profile tailoring. Super-Gaussians of order 1,2 and 3 was fit to the horizontal line-out of the intensity profile.

How well the super-Gaussian functions fitted the data was measured as the mean difference between the data, $y(x)$, and the fitted super-Gaussian of order n, $g_n(x)$.

$$\epsilon_n = \frac{1}{L}\int_L |z(x) - g_n(x)|dx \tag{5.31}$$

The deviations were calculated for the super-Gaussian fits of order 1, 2 and 3 in Figure 5.16.

ϵ_1	ϵ_2	ϵ_3
0.061	0.023	0.057

This shows that a super-Gaussian of the second order fitted the data better than a standard Gaussian (first order) or a super-Gaussian of the third order. So, even if the focal spot intensity profile was not top-hat, it was indeed flatter than the original Gaussian profile.

Improvements

The top-hat results that were obtained with the current scheme were not satisfying. It is however still believed that a genetic algorithm in conjunction with a deformable mirror could be used to produce arbitrary tailored focal spots. But, some things must be improved in order to make this scheme work better.

The reference image must be a realistic goal for the algorithm. A deeper analysis would involve a calculation of the aperture phase that is needed to produce a given profile (through an inverse Fourier transform). It is then necessary to estimate if it is possible for the mirror to take on such a shape (that is, if its spatial resolution is high enough).

When voltage was applied to the actuators, the membrane mirror was attracted towards them. The mirror took on a concave shape and, since the incident beam was plane, the mirror focused the beam. When the membrane was deflected to half its maximum, the focal length was approximately 5 m. This must be compensated for and, in order to match the laser wavefront to the mirror shape, the incident beam should be slightly divergent. In fact, if the half deflected membrane has a radius of curvature of R, the radius of curvature of the incident beam should be R/2 at the deformable mirror. In a setup were the beam is expanded by a telescope right before it hits the deformable mirror, the last lens in the telescope can be adjusted in order to collimate the reflected beam. This was not done in the experiments in Section 5.1 since the idea was to quantify the impact of the deformable mirror, compared to the plane mirror. It should, however, have been done in the current experiment in order to gain optimal results.

The fitness function calculated the distance between the reference image and the current intensity profile, using all pixels in the entire image. In order to increase the signal to noise ratio, a region of interest (ROI) that encircles the reference structure should be employed. Fitness would in that case only be calculated from the points inside the ROI.

There are also some indications that the failure was partly due to a bug in the computer software. This possibility has not been investigated thoroughly but, possibly the pixel values at the center of the focal spot were interpreted badly by the acquisition software.

Chapter 6

Summary and outlook

In this work a Micromachined Membrane Deformable Mirror has been used in conjunction with a Genetic Algorithm to control the focusing characteristics of two different laser systems. The experimental work was divided in two main parts. The first part investigated the capabilities of the adaptive system to pre-compensate for alignment errors of the focusing optics. The second part looked into the possibilities to tailor the intensity profile of the focal spot. Numerical calculations of the membrane mirror response to the applied actuator voltages were also performed. This chapter gives a short summary of the conclusions that were reached and points at possible future work that might be a natural continuation of this project.

6.1 The membrane mirror

The membrane deformable mirror was mainly used to correct for astigmatic errors. The tests with the spherical mirror in Section 5.1.2 showed that it is possible to use a spherical mirror for off-axis focusing if a deformable mirror is used to compensate for the induced astigmatism. This is promising since spherical mirrors are cheaper and easier to manufacture than parabolic mirrors. One should however keep in mind that deformable mirrors are sophisticated devices and thus they tend to be quite expensive. The membrane deformable mirror was also used to correct for intrinsic aberrations that may be present in complex laser systems such as the Ti:sapphire CPA laser-chain in Lund. Intrinsic aberrations means here alignment errors of the focusing and other optics, surface quality of optical components, thermal effects, nonlinear effects and doping inhomogeneities in the amplifying crystals. All such aberrations decrease the peak intensity in the focal spot. The deformable mirror and the Genetic Algorithm were able to increase the peak intensity by 85%. The deformable mirror was however *not* able to correct for chromatic aberrations.

In the tests with the spherical mirror in Section 5.1.2, heavily astigmatic foci were corrected by the deformable mirror. It is thus most likely that a deformable mirror could be used to remove the alignment errors that are unavoidable also when a f/1 parabola is used for focusing.

6.2 The Genetic Algorithm

The Genetic Algorithm turned out to be a very flexible instrument to control the mirror. The tests in Section 5.2 could be performed with the same algorithm that was used in Section 5.1. Only the fitness function needed to be changed. By choosing an appropriate fitness function, the characteristics of the focal spot could be controlled. This was demonstrated when two focal spots of equal intensity were produced in Section 5.2.1. By slightly changing the fitness function, the intensity halfway between the spots was minimized. The strength of the algorithm was also demonstrated when the strong pulse-to-pulse fluctuations of the Ti:sapphire laser were encountered. Increasing the size of the population proved to be a more efficient way to reduce the effect of this noise than for example averaging over a number of acquisitions. The main drawback of the algorithm was that it was time-consuming and normally it needed hours to converge. The bottleneck was the repetition rate of the acquisition system since only two images per second were delivered to the algorithm. The High-Power laser operates at a 10 Hz repetition rate so the convergence time could be increased by 500%. Using a kHz- or a continuous laser, the repetition rate of the CCD-camera sets the limits to 25 Hz. This would reduce the execution time to minutes, instead of hours.

The convergence rate of the algorithm could have been increased in other ways than just increasing the acquisition rate. Possible improvements of the algorithm were discussed in Section 4.4.4. The simulations in Section 2.4 provide *a priori* information about the shape of the membrane mirror. Using this information one could decrease the number of degrees of freedom which would speed up the convergence and contribute to the stability of the algorithm.

6.3 Future work

A deformable mirror may enhance the characteristics of a high-power laser in several ways. If it is positioned right before the focusing optics (as in [1] [2] [9] [17]) it may correct for phase errors, inheriting from both the focusing optics and the laser chain, that degrade the focusing power of the system. A configuration like this aims for a smaller spot size. A deformable mirror may also be positioned in an amplifier [4], in order to smoothen the intensity profile and eliminate unwanted hot-spots that may damage the optics. If a deformable mirror is placed in the Fourier plane in a stretcher, [7], or in a compressor (see [3] [27]), it may be used also to control the temporal aspects of ultrafast laser pulses.

There are two CPA laser-systems at the Lund High-Power Facility. The kHz-laser delivers ultrashort pulses at a kHz repetition rate. The beam diameter is 8mm and the usable diameter of the mirror that has been used in this work was 9mm. The beam diameter and the fast repetition rate of this laser make a scheme involving this mirror and Genetic Algorithm attractive.

The other CPA laser-system is the 10-Hz system that was described in Chapter 4. The beam diameter is 40mm so only a small part of the beam was used for the tests in Chapter 5. A mirror with diameter of 50-60mm is needed to control the beam. This requires a bimorph mirror. If a genetic algorithm is used for optimization, the 10-Hz repetition rate of the laser might give rise to unacceptable convergence times. If a wavefront sensor measures the wavefront

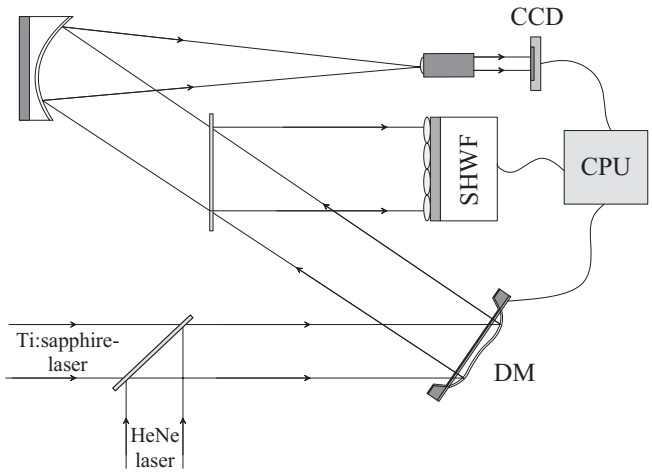

Figure 6.1: The genetic algorithm optimizes the focal spot peak intensity when the High-Power laser is turned off. The Shack-Hartman wavefront sensor (SHWS) measures the optimized wavefront. The High-Power laser wavefront is then changed to this wavefront by the deformable mirror (DM).

between the focusing parabola and the deformable mirror, it would be possible to deliver a plane wave to the parabola. But if the parabola is not perfectly aligned or if there are intrinsic manufacturing errors, a plane wavefront would not result in a diffraction-limited spot. In Figure 6.1 a scheme is illustrated that would allow correction for both intrinsic laser aberrations *and* focusing optics errors;

- A HeNe-laser is aligned so that the continuous beam coincides with the Ti:sapphire beam.
- With the High-Power laser-system turned off, the genetic algorithm optimizes the focal spot peak intensity.
- The wavefront sensor measures the optimized wavefront. This a reference wavefront that conjugates the errors introduced by the parabola.
- The High-Power system is turned on and the wavefront sensor measures the wavefront of the Ti:sapphire beam.
- The deformable mirror is configured in order to reproduce the reference wavefront that was found by the genetic algorithm. This will only require a single or a few iterations, depending on the linearity of the mirror.

This is an approach to wavefront correction of a High-Power laser that has not, to the best of our knowledge, yet been investigated.

Acknowledgements

First of all I would like to thank my supervisor *Claes-Göran Wahlström*. His support and never-ending enthusiasm has inspired and encouraged me throughout the course of this work.

I am also very grateful to my assistant supervisor *Anders Persson* for always taking his time to answer my questions about laser technology in general and the terawatt laser in particular. His help was indispensable when the equipment was moved to the terawatt laser.

I would like to thank *Anders Sjögren* who wrote the drivers for the camera. Without his help a large part of this project would have been impossible to carry out and I am very grateful for that.

I would also like to thank *Per Knutsson* at the Astronomy Division for a very nice demonstration of dual conjugate adaptive optics.

I also thank *Åke Bergquist* for building the high-voltage units and *Johan Mauritsson* and *Per Johnsson* who answered many of my questions about LaTeX.

A special thanks goes to *Anne L'Huillier* for being an excellent teacher. She is the person who got me interested in laser- and atomic physics and opened up this new world for me.

At last I would like to express my gratitude to the people at *Laboratoire d'Optique Appliquée* (LOA) in Paris. Especially I would like to thank *Jean-Paul Chambaret*, *Gilles Chériaux*, *Olivier Albert* and *Thomas Planchon*. They were very kind during my visit to Paris and they made this project possible since they kindly lent the deformable mirror to the Atomic Physics Division in Lund.

Appendix A

Influence function approach to the mirror response

When configuring the shape of a deformable mirror in an open loop, i.e. without feedback, an *influence function* approach might be appropriate. An influence function is the deformation produced by a single actuator. There are 37 influence functions for a 37 actuator deformable mirror. The mirror response to actuator voltages is assumed (which is not really true) to be linear so the mirror shape can be represented as a linear combination of the influence functions. This chapter aims to develop tools in order to analytically calculate the influence functions of a membrane mirror. Most of the derivations origin from [8].

The deformation of a membrane mirror under electrostatic load is the solution to Poisson's equation.

$$\begin{cases} \Delta u = -\frac{p}{T} & (x,y) \in \Omega \\ u(x,y) = 0 & (x,y) \in \partial\Omega \end{cases} \tag{A.1}$$

Solutions to the Poisson equation are linear in electrode pressure [13] and can thus be represented as

$$u_i = \sum_{j=1}^{37} \mathcal{A}_{ij} P_j \tag{A.2}$$

where u_i is the displacement of the i:th surface element, P_j is the pressure over the j:th actuator. $\mathcal{A}_{ij}$ are coefficients that has to be calculated. The 37 column vectors of the matrix $\mathcal{A}$ are the influence functions. In this notation the membrane deflection is represented as a column vector, $\mathbf{u}$. Each element u_i of the vector is the deflection in the point (r_i, ϕ_i) on the circular mirror. Each influence function is the displacement of the membrane, caused by unit pressure from that electrode. Equation A.2 can be written in matrix form

$$\mathbf{u} = \mathcal{A}\mathbf{P} \tag{A.3}$$

$\mathbf{P}$ is a column vector (37x1) and each element of $\mathbf{P}$ is the pressures exerted on the membrane from the different actuators.

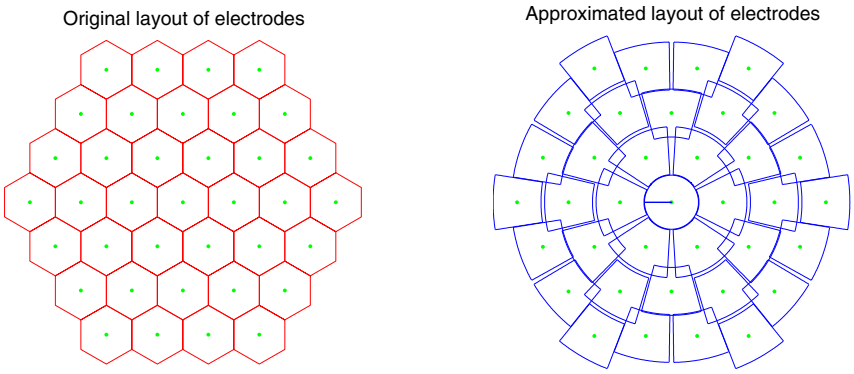

Figure A.1: Original and approximated actuator electrode layouts.

A.1 Determination of the influence function matrix

As stated before the tension T in equation A.1 is assumed to be constant and the deflections of the membrane are assumed to be small. The membrane radius is normalized to unity so that $u = 0$ at $r = 1$. The solution to Poisson's equation in equation A.1 is given by [14]

$$u(r,\phi) = \frac{a^2}{2\pi T}\int_0^{2\pi} \left[\int_0^r \left\{ln(1/r) - \sum_{n=1}^{\infty}\frac{\cos n(\phi'-\phi)}{n}[(rr')^n - (r'/r)^n]\right\}P(r',\phi')r'dr' + \int_r^1 \left\{ln(1/r') - \sum_{n=1}^{\infty}\frac{\cos n(\phi'-\phi)}{n}[(r'r)^n - (r/r')^n]\right\}P(r',\phi')r'dr'\right]d\phi' \quad \text{(A.4)}$$

Here $P(r,\phi)$ is the pressure on the membrane at position (r,ϕ) and a is the membrane radius. To simplify the calculations and allow an analytic integration of equation A.4 the hexagonal actuators are approximated by actuators with the same area but with a slightly different shape. The shape that is chosen is bounded by lines of constant r and ϕ. The bounds of electrode j will be noted (r_{1j}, r_{2j}) and (ϕ_{1j}, ϕ_{2j}). The center of the approximated electrode $\{(r_{1j} - r_{2j})/2, (\phi_{1j}, \phi_{2j})/2\}$ is positioned at the same point as the geometric center of the original hexagonal electrode. The dimensions of the approximated electrode are chosen so that the length of its radial bisector equals the length of its angular bisector. Figure A.1 shows the original and the approximated electrode layout. In order to obtain the influence function matrix in equation A.2 we evaluate equation A.4 at a point (r_i, ϕ_i). Let $\theta_j(r,\phi)$ be a function that is 1 over actuator j and zero elsewhere. The pressure exerted on the membrane by the actuator structure can then be written as

$$P(r_i,\phi_i) = \sum_{j=1}^{37} P_j\theta_j(r_i,\phi_i) \quad \text{(A.5)}$$

where P_j is the pressure over actuator j and V_j is the voltage applied to that actuator. d is the distance between the actuators and the membrane. This equation is valid under the assumption that the pressure over an actuator is caused only by that actuator which is the case if the actuator-actuator spacing is much larger than the actuator-mirror spacing. The MMDM used had an actuator-actuator spacing of 1,8mm and an actuator to mirror spacing of $75\mu m$. The expression for the pressure over the membrane in equation A.5 simplifies the solution in equation A.4 and we get the deflection of the membrane in the desired matrix form

$$u_i = \frac{a^2}{T}\sum_{j=1}^{37} A_{ij}P_j \tag{A.6}$$

where the matrix elements, A_{ij}, are given by

$$\begin{aligned} A_{ij} = \frac{1}{2\pi}\Bigg\{&(\phi_{2j}-\phi_{1j})\left[ln(1/r_i)\int_0^{r_i} r'dr' + \int_{r_i}^1 ln(1/r')r'dr'\right] \\ &-\int_0^{r_i}\sum_{n=1}^{\infty}\frac{\sin n(\phi_{2j}-\phi_i)-\sin n(\phi_{1j}-\phi_i)}{n^2}[(r_ir')^n-(r'/r_i)^n]r'dr' \\ &-\int_{r_i}^1\sum_{n=1}^{\infty}\frac{\sin n(\phi_{2j}-\phi_i)-\sin n(\phi_{1j}-\phi_i)}{n^2}[(r'r_i)^n-(r_i/r')^n]r'dr'\Bigg\} \end{aligned} \tag{A.7}$$

As already mentioned ϕ_{1j} and ϕ_{2j} are the angular bounds of the j:th actuator. (r_i, ϕ_i) is the point on the membrane where the deflection u_i is calculated. The matrix elements in equation A.7 has been analytically calculated [8]. Different expressions are needed, depending on the radial position r_i of the i:th surface point and the radial ranges r_{1j} and r_{2j} of the j:th actuator. There are five cases:

- $r_i = r_{1j} = 0$

$$A_{ij} = \frac{\Delta\phi_j}{2\pi}\left(\frac{1}{2}-\ln r_{2j}\right)\frac{r_{2j}^2}{2} \tag{A.8}$$

- $r_i = 0, r_{1j} > 0$

$$A_{ij} = \frac{\Delta\phi_j}{2\pi}\left[r_{2j}^2\left(\frac{1}{2}-\ln r_{2j}\right) - r_{1j}^2\left(\frac{1}{2}-\ln r_{1j}\right)\right]\frac{1}{2} \tag{A.9}$$

- $r_{2j} \le r_i$

$$\begin{aligned} A_{ij} = \frac{1}{2\pi}\Bigg\{&-\frac{\Delta\phi_j}{2}\left(r_{2j}^2-r_{1j}^2\right)\ln r_i - \sum_{n=1}^{\infty}\frac{r_i^2\left(r_i^{2n}-1\right)}{n^2(n+2)} \\ &\times\left[\left(\frac{r_{2j}}{r_i}\right)^{n+2}-\left(\frac{r_{1j}}{r_i}\right)^{n+2}\right][\sin n(\phi_{2j}-\phi_i)-\sin n(\phi_{1j}-\phi_i)]\Bigg\} \end{aligned} \tag{A.10}$$

- $r_i \le r_{1j}$

$$\begin{aligned} A_{ij} = \frac{1}{2\pi}\Bigg\{&\frac{\Delta\phi_j}{2}\left[r_{2j}^2\left(\frac{1}{2}-\ln r_{2j}\right) - r_{1j}^2\left(\frac{1}{2}-\ln r_{1j}\right)\right] - \\ &-\sum_{n=1}^{\infty}\frac{r_i^n\left(r_{2j}^{n+2}-r_{1j}^{n+2}\right)/(n+2)+\alpha_n}{n^2} \\ &\times\Big[\sin n(\phi_{2j}-\phi_i)-\sin n(\phi_{1j}-\phi_i)\Big]\Bigg\} \end{aligned} \tag{A.11}$$

where

$$\begin{aligned}
\alpha_1 &= -r_i(r_{2j} - r_{1j}) \\
\alpha_2 &= -r_i^2(\ln r_{2j} - \ln r_{1j}) \\
\alpha_n &= \tfrac{r_i^2}{n-2}\left[\left(\tfrac{r_i}{r_{2j}}\right)^{n-2} - \left(\tfrac{r_i}{r_{1j}}\right)^{n-2}\right] \ , \ n \geq 3
\end{aligned}$$

- $r_{1j} < r_i < r_{2j}$. Substitute r_i for r_{2j} in equation A.10 and r_i for r_{1j} in equation A.11. Add the results.

When the matrix A is calculated all possible membrane deflections can be calculated through equation A.2 where $\mathcal{A} = (a^2/T)A$. If the membrane is grounded and voltages are applied to the actuators, the pressure exerted on the membrane by the actuator structure is given in equation 2.19. The membrane deflection can then be calculated as a function of voltage

$$\mathbf{u} = \frac{\epsilon\epsilon_0 a^2}{Td^2}\mathbf{A}\mathbf{V}^2 \tag{A.12}$$

The elements of $\mathbf{V}^2$ are the squared actuator voltages.

Appendix B

Matrix formulation of paraxial optics

When an optical system consists of many components, a systematic description of the optical elements is needed. In this approach, a paraxial ray is described by two numbers, distance (y_0) and angle (α_0) with respect to the optical axis. An element of the optical system is considered as a linear system, that is its influence on a paraxial ray is defined by a matrix. This means that an incident ray (y_0, α_0) results in an outgoing ray (y, α) according to [16]

$$\begin{bmatrix} y \\ \alpha \end{bmatrix} = \begin{bmatrix} A & B \\ C & D \end{bmatrix} \begin{bmatrix} y_0 \\ \alpha_0 \end{bmatrix} \tag{B.1}$$

The ABCD-matrix defines the effect of the optical component on a paraxial ray. A simple translation of a ray in a homogeneous medium is in this matrix notation written

$$M_L = \begin{bmatrix} 1 & L \\ 0 & 1 \end{bmatrix} \tag{B.2}$$

where L is the length of the translation. Another important matrix is the thin-lens matrix.

$$M_f = \begin{bmatrix} 1 & 0 \\ -\frac{1}{f} & 1 \end{bmatrix} \tag{B.3}$$

where f is the focal length of the lens. The combined effect of several optical components is in this linear system approach the product of their matrices. The distance between the last component of such a system and the focal plane is given by [16]

$$F = -\frac{A}{C} \tag{B.4}$$

A system consisting of two lenses with focal lengths f_1 and f_2 that are separated by a distance L yields the ABCD-matrix

$$M = M_{f_2} M_L M_{f_1} = \begin{bmatrix} 1 & 0 \\ -\frac{1}{f_2} & 1 \end{bmatrix} \begin{bmatrix} 1 & L \\ 0 & 1 \end{bmatrix} \begin{bmatrix} 1 & 0 \\ -\frac{1}{f_1} & 1 \end{bmatrix} = \begin{bmatrix} 1 - \frac{L}{f_1} & L \\ \frac{L}{f_1 f_2} - \frac{1}{f_1} - \frac{1}{f_2} & 1 - \frac{L}{f_2} \end{bmatrix} \tag{B.5}$$

The distance from the last lens (f_2) to the focal plane is then

$$F = -\frac{A}{C} = -\frac{1 - \frac{L}{f_1}}{\frac{L}{f_1 f_2} - \frac{1}{f_1} - \frac{1}{f_2}} = \frac{f_1 - L}{f_1 + f_2 - L} \cdot f_2 \tag{B.6}$$

If the first lens is a spherical mirror with radius of curvature R the focal plane will be at a distance

$$F = \frac{R/2 - L}{f + R/2 - L} \cdot f \tag{B.7}$$

from the last lens with focal length f. This means that when the spherical mirror is positioned at a distance L from the focusing lens, the focal plane will move a distance

$$\delta = f - F = \left(1 - \frac{R/2 - L}{f + R/2 - L}\right) \cdot f = \frac{f^2}{f + R/2 - L} \tag{B.8}$$

towards the focusing lens.

Bibliography

[1] O. Albert, L. Sherman, G. Mourou, T.B. Norris, and G. Vdovin. Smart microscope: an adaptive optics learning system for aberration correction in multiphoton confocal microscopy. *Optics Letters*, 25:52–54, 2000.

[2] O. Albert, H. Wang, D. Liu, Z. Chang, and G. Mourou. Generation of relativistic intensity pulses at a kilohertz repetition rate. *Optics Letters*, 25:1125–1127, 2000.

[3] M.R. Armstrong, P. Plachta, E. Ponomarev, and R.J.D. Miller. Versatile 7-fs parametric pulse generation and compression by use of adaptive optics. *Optics Letters*, 26:1152–1154, 2001.

[4] H. Baumhacker, G. Pretzler, K.J. Witte, M. Hegelich, M. Kaluza, S. Karsch, A. Kudryashov, V. Samarkin, and A. Roukossouev. Correction of strong phase and amplitude modulations by two deformable mirrors in a multistaged Ti:sapphire laser. *Optics Letters*, 27:1570–1572, 2002.

[5] M. Born and E. Wolf. *Principles of optics*. University Press, Cambridge, 1999.

[6] I. Buske, H.M. Heuck, and U. Wittrock. Master-Oscillator-Power-Amplifier laser with adaptive aberration correction. In *Proceedings of the 3nd international workshop on adaptive optics for Industry and Medicine*, Albuquerque, USA, 2001.

[7] G. Chériaux, O. Albert, V. Wänman, J.P. Chambaret, C. Felix, and G. Mourou. Temporal control of amplified femtosecond pulses with a deformable mirror in a stretcher. *Optics Letters*, 26:169–171, 2001.

[8] E.S. Claflin and N. Bareket. Configuring an electrostatic membrane mirror by least-squares fitting with analytically derived influence functions. *Journal of the Optical Society of America A*, 3:1833–1839, 1986.

[9] F. Druon, G. Chériaux, J. Faure, J. Nees, M. Nantel, A. Maksimchuk, G. Mourou, J.C. Chanteloup, and G. Vdovin. Wave-front correction of femtosecond terawatt lasers by deformable mirrors. *Optics Letters*, 23:1043–1045, 1998.

[10] J.W. Goodman. *Introduction to Fourier Optics*. McGraw-Hill, United States of America, 1968.

[11] G. Harbers, P.J. Kunst, and W.R. Leibbrandt. Analysis of lateral shearing interferograms by use of Zernike polynomials. *Applied Optics*, 35:6162–6172, 1996.

[12] J. Mauritsson. *Temporal aspects of high-intensity laser-matter interactions*. PhD thesis, Lund Institute of Technology, 2003. LRAP-312.

[13] P.M Morse and H. Feshbach. *Methods of Theoretical Physics, Part I*, pages 793–795. McGraw-Hill, New York, 1953.

[14] P.M Morse and H. Feshbach. *Methods of Theoretical Physics, Part II*, page 1191. McGraw-Hill, New York, 1953.

[15] K. Nemoto, T. Nayuki, T. Fujii, N. Goto, and Y.K. Kanai. Optimum control of the laser beam intensity profile with a deformable mirror. *Applied Optics*, 36:7689–7695, 1997.

[16] F.L. Pedrotti and L.S. Pedrotti. *Introduction to optics*. Prentice-Hall, New Jersey, 1996.

[17] T.A. Planchon, P. Mercère, G. Chériaux, and J.P. Chambaret. Off-axis aberration compensation of focusing with spherical mirrors using deformable mirrors. *Optics Communications*, 216:25–31, 2003.

[18] M.L. Plett, P.R. Barbier, and D.W. Rush. Compact adaptive optical system based on blind optimization and a micromachined membrane deformable mirror. *Applied Optics*, 40:327–330, 2001.

[19] J. Queneuille, F. Druon, A. Maksimchuk, G. Chériaux, G. Mourou, and K. Nemoto. Second-harmonic generation and wavefront correction of a terawatt laser system. *Optics Letters*, 25:508–510, 2000.

[20] G. Sparr and A. Sparr. *Kontinuerliga system*. Studentlitteratur, Lund, 2000.

[21] O. Svelto. *Principles of lasers*. Plenum Press, New York, 1998.

[22] G. Vdovin. Micromachined Membrane Deformable Mirrors. In R.K. Tyson, editor, *Adaptive optics engineering handbook*. Dekker Inc, New York, 2000.

[23] G. Vdovin and V. Kiyko. Intracavity control of a 200-W continuous-wave nd:yag laser by a micromachined deformable mirror. *Optics Letters*, 26:798–800, 2001.

[24] G. Vdovin and P.M. Sarro. Flexible mirror micromachined in silicon. *Applied Optics*, 34:2968–2972, 1995.

[25] M.A. Vorontsov and G.W. Carhart. Adaptive phase distortion correction in strong speckle-modulation conditions. *Optics Letters*, 27:2155–2157, 2002.

[26] B. Wattellier, J. Fuchs, J.P. Zou, J.C. Chanteloup, H. Bandulet, P. Michel, C. Labaune, S. Depierreux, A. Kudryashov, and A. Aleksandrov. Generation of a single hot spot by use of a deformable mirror and study of its propagation in an underdense plasma. *Journal of the Optical Society of America B*, 20:1632–1642, 2003.

[27] E. Zeek, K. Maginnis, S. Backus, U. Russek, M. Murnane, G. Mourou, H. Kapteyn, and G. Vdovin. Pulse compression by use of deformable mirrors. *Optics Letters*, 24:493–495, 1999.

[28] Z. Zeng, N. Ling, and W. Jiang. The investigation of controlling laser focal profile by deformable mirror and wave-front sensor. *Journal of Modern Optics*, 46:341–348, 1999.

[29] L. Zhu, P.S. Sun, D.U. Bartsch, W.R. Freeman, and Y. Fainman. Adaptive control of a micromachined continuous-membrane deformable mirror for aberration compensation. *Applied Optics*, 38:168–176, 1999.

[30] L. Zhu, P.S. Sun, D.U. Bartsch, W.R. Freeman, and Y. Fainman. Wavefront generation of Zernike polynomial modes with a micromachined deformable mirror. *Applied Optics*, 38:6019–6026, 1999.